



UNA PUBLICACIÓN DE LA
SOMIB
Sociedad Mexicana de
Ingeniería Biomédica

Revista Mexicana de Ingeniería Biomédica

New publishing model

*Continuous publication:
as soon as an article is prepared,
it will be released online*

Sociedad Mexicana de Ingeniería Biomédica

La Mesa Directiva de la Sociedad Mexicana de Ingeniería Biomédica hace una extensa invitación a las personas interesadas en participar, colaborar y pertenecer como Socio Activo de la SOMIB. La SOMIB reúne a profesionistas que se desarrollan en áreas de Ingeniería Biomédica, principalmente ingenieros biomédicos, así como otros profesionistas afines con el desarrollo de tecnología para la salud.

Membresía Estudiante

\$850.00 PESOS MXN

15% de descuento para grupos de 5 o más personas.

Membresía Profesional

\$1,450.00 PESOS MXN

15% de descuento para grupos de 5 o más personas.

Membresía Institucional

\$11,600.00 PESOS MXN

No aplica descuento.

Membresía Empresarial

\$20,000.00 PESOS MXN

La suscripción empresarial requiere invitación.

EL PAGO CUBRE UN AÑO DE CUOTA. EN CASO DE REQUERIR FACTURA
FAVOR DE SOLICITARLA, ADJUNTANDO COMPROBANTE DE PAGO Y ESPECIFICANDO CONCEPTO,
AL CORREO ELECTRÓNICO: facturación@somib.org.mx

ib Revista Mexicana de Ingeniería Biomédica

AUTORES

Los trabajos a publicar en la RMIB, deben ser originales, inéditos y de excelencia. Los costos de publicación para autores son los siguientes:

NO SOCIOS: \$4,060.00 PESOS MXN (INCLUYE I.V.A.)

SOCIOS: \$1,276.00 PESOS MXN (INCLUYE I.V.A.)

PUBLICIDAD

A las empresas e instituciones interesadas en publicitar su marca o productos en la RMIB, los costos por número son los siguientes:

MEDIA PLANA: \$4,999.00 PESOS MXN (INCLUYE I.V.A.)

UNA PLANA: \$6,799.00 PESOS MXN (INCLUYE I.V.A.)

CONTRAPORTADA: \$7,799.00 PESOS MXN (INCLUYE I.V.A.)

FORROS INTERIORES: \$7,799.00 PESOS MXN (INCLUYE I.V.A.)

DESCUENTO DEL 20% AL CONTRATAR PUBLICIDAD EN DOS O MÁS NÚMEROS.

Para ser socio

- › Realiza el pago de derechos, de acuerdo a la categoría que te corresponde.
- › Ingresa a www.somib.org.mx/membresia y elige el tipo de membresía por el cual realizaste el pago de derechos.
- › Completa el formulario correspondiente y envíalo.
- › Se emitirá carta de aceptación y número de socio por parte de la mesa directiva (aprobada la solicitud).
- › Para mayor información sobre beneficios, ingresar a: www.somib.org.mx o comunicarse al correo socios@somib.org.mx.

Datos bancarios

- › **Beneficiario:** Sociedad Mexicana de Ingeniería Biomédica A. C.
- › **Banco:** Scotiabank
- › **Referencia:** 1000000333
- › **Cuenta:** 11006665861
- › **CLABE Interbancaria:** 044770110066658614

La inserción de la publicidad será publicada en el libro electrónico y en el área de patrocinios en el sitio Web de la revista (RMIB), disponible en:

<http://rmib.mx>

Fundador
Dr. Carlos García Moreira

COMITÉ EDITORIAL

Editor en Jefe
Dr. César A. González Díaz
INSTITUTO POLITÉCNICO NACIONAL-MÉXICO

Editores Asociados Nacionales

Dra. Dora-Luz Flores

UNIVERSIDAD AUTÓNOMA DE BAJA CALIFORNIA

Dr. Aldo Rodrigo Mejía Rodríguez

FACULTAD DE CIENCIAS
UNIVERSIDAD AUTÓNOMA DE SAN LUIS POTOSÍ

Dra. Citlalli Jessica Trujillo Romero

DIVISIÓN DE INVESTIGACIÓN EN INGENIERÍA MÉDICA
INSTITUTO NACIONAL DE REHABILITACIÓN-LUIS GUILLERMO IBARRA IBARRA

Dr. Christian Chapa González

INSTITUTO DE INGENIERÍA Y TECNOLOGÍA
UNIVERSIDAD AUTÓNOMA DE CIUDAD JUÁREZ

Dr. Rafael Eliecer González Landaeta

UNIVERSIDAD AUTÓNOMA DE CIUDAD JUÁREZ

Editores Asociados Internacionales

Dr. Leonel Sebastián Malacrida Rodríguez

UNIVERSIDAD DE LA REPÚBLICA, URUGUAY

Dra. Elisa Scalco

INSTITUTE OF BIOMEDICAL TECHNOLOGY
ITALIAN NATIONAL RESEARCH COUNCIL, MILAN, ITALY

Dra. Natali Olaya Mira

INSTITUTO TECNOLÓGICO METROPOLITANO
ITM, MEDELLÍN, COLOMBIA

Índices

La Revista Mexicana de Ingeniería Biomédica aparece en los siguientes índices científicos:
Sistema de Clasificación de Revistas Científicas y Tecnologías del CONACYT - Q4, SCOPUS, SciELO, EBSCO, Medigraphic Literatura Biomédica, Sociedad Iberoamericana de Información Científica - SIIC.

www.rmib.mx
ISSN 2395-9126

Asistente Editorial
Carla Ivonne Guerrero Robles

Editor Técnico y en Internet
Enrique Ban Sánchez

Se autoriza la reproducción parcial o total de cualquier artículo a condición de hacer referencia bibliográfica a la Revista Mexicana de Ingeniería Biomédica y enviar una copia a la redacción de la misma.



Sociedad Mexicana de Ingeniería Biomédica

Periferico Sur #5374, Col. Olímpica, Alc. Coyoacán, C. P. 04710, Ciudad de México, CDMX, México (555) 574-4505



MESA DIRECTIVA

Ing. Herberth Bravo Hernández

PRESIDENTE

Ing. Eduardo Méndez Palos

VICEPRESIDENTE

Ing. Janetthe Mariana Tarín León

SECRETARIA

Mtro. Jaime Arturo Quirarte Tejeda

TESORERO

Dr. César A. González Díaz

EDITOR DE RMIB

Afiliada a:

International Federation of Medical and Biological Engineering (IFMB-IUPSM-ICSU)

Federación de Sociedades Científicas de México, A.C. (FESOCIME)

Consejo Regional de Ingeniería Biomédica para América Latina (CORAL)

SOMIB

Periferico Sur #5374, Col. Olímpica, Alc. Coyoacán, C. P. 04710, Ciudad de México, CDMX, México (555) 574-4505

www.somib.org.mx

REVISTA MEXICANA DE INGENIERÍA BIOMÉDICA, Vol. 42, No. 3, Septiembre-Diciembre 2021, es una publicación cuatrimestral editada por la Sociedad Mexicana de Ingeniería Biomédica A.C., Periferico Sur #5374, Col. Olímpica, Alc. Coyoacán, C. P. 04710, (555) 574-4505, www.somib.org.mx, rmib.somib@gmail.com. Editor responsable: César Antonio Díaz González. Reserva de Derechos al Uso Exclusivo No. 04-2015-041310063800-203, ISSN (impreso) 0188-9532; ISSN (electrónico) 2395-9126, ambos otorgados por el Instituto Nacional del Derecho de Autor. Responsable de la última actualización de este número: Lic. Enrique Federico Ban Sánchez, Periferico Sur #5374, Col. Olímpica, Alc. Coyoacán, C. P. 04710, (555) 574-4505, fecha de última modificación, 1 de agosto de 2020.

El contenido de los artículos, así como las fotografías son responsabilidad exclusiva de los autores. Las opiniones expresadas por los autores no necesariamente reflejan la postura del editor de la publicación.

Queda estrictamente prohibida la reproducción total o parcial de los contenidos e imágenes de la publicación sin previa autorización de la Sociedad Mexicana de Ingeniería Biomédica.

Disponible en línea:

www.rmib.mx

CONTENTS**CONTENIDO****Contents**

p 5

Review Article

p 6

A Practical Review of the Biomechanical
Parameters Commonly Used in the Assessment
of Human Gait
*Revisión Práctica de los Parámetros
Biomecánicos Comúnmente Utilizados en
la Evaluación de la Marcha Humana*

Research Article

p 28

Image-based Glaucoma Classification Using
Fundus Images and Deep Learning
*Clasificación de Glaucoma Basada en Imágenes
de Fondo de Ojo y Aprendizaje Profundo*

Research Article

p 42

Identification of 7 Movements of the Human
Hand Using sEMG - 360° on the Forearm
*Identificación de 7 Movimientos de la Mano
Humana Utilizando sEMG - 360° en el Antebrazo*

Research Article

p 51

Shielding Volume Reduction in a High Dose
Rate Brachytherapy Room
*Reducción de Volumen de Blindaje en una Sala de
Braquiterapia de Alta Tasa de Dosis*

dx.doi.org/10.17488/RMIB.42.3.1

E-LOCATION ID: 1189

A Practical Review of the Biomechanical Parameters Commonly Used in the Assessment of Human Gait

Revisión Práctica de los Parámetros Biomecánicos Comúnmente Utilizados en la Evaluación de la Marcha Humana

J. C. Arellano-González¹, H. I. Medellín-Castillo², J. J. Cervantes-Sánchez¹, A. Vidal-Lesso¹

¹División de Ingenierías Campus Irapuato Salamanca, Universidad de Guanajuato

²Facultad de Ingeniería, Universidad Autónoma de San Luis Potosí

ABSTRACT

The analysis of human gait is a potential diagnostic instrument for the early and timely identification of pathologies and disorders. It can also supply valuable data for the development of biomedical devices such as prostheses, orthoses, and rehabilitation systems. Although various research papers in the literature have used human gait analyses, few studies have focused on the biomechanical parameters used. This paper presents an extensive review and analysis of the main biomechanical parameters commonly used in the human gait study. The aim is to provide a practical guide to support and understand of the choices and selection of the most appropriate biomechanical parameters for gait analysis. A comprehensive search in scientific databases was conducted to identify, review and analyze the academic work related to human gait analysis. From this search, the main biomechanical parameters used in healthy and pathological gait studies were identified and analyzed. The results have revealed that the spatiotemporal and angular gait parameters are the most used in the assessment of healthy and pathological human gait.

KEYWORDS: Gait analysis, Healthy gait, Pathological gait, Gait parameters

RESUMEN

El análisis de la marcha humana es un instrumento potencial de diagnóstico para la identificación oportuna y temprana de patologías y trastornos. También puede proporcionar información valiosa para el desarrollo de dispositivos biomédicos tales como prótesis, órtesis y sistemas de rehabilitación. Aun cuando diversos trabajos de investigación en la literatura han utilizado el análisis de la marcha humana, pocos estudios se han enfocado en analizar los parámetros biomecánicos utilizados. Este trabajo presenta una revisión completa y análisis de los parámetros biomecánicos comúnmente utilizados en el estudio de la marcha humana. El objetivo es proporcionar una guía práctica para apoyar y entender las opciones y selección de los parámetros biomecánicos más adecuados para el análisis de la marcha. Se llevó a cabo una búsqueda exhaustiva en bases de datos científicas para identificar, revisar, y analizar los trabajos de investigación relacionados con el análisis de la marcha humana. A partir de esta búsqueda se identificaron y analizaron los principales parámetros biomecánicos utilizados en estudios de la marcha sana y patológica. Los resultados han revelado que los parámetros espaciotemporales y angulares son los más utilizados en la evaluación de la marcha humana tanto sana como patológica.

PALABRAS CLAVE: Análisis de la marcha, Marcha sana, Marcha patológica, Parámetros de la marcha

Corresponding author

TO: Juan Carlos Arellano González
INSTITUTION: Universidad de Guanajuato
ADDRESS: Carretera Salamanca-Valle de Santiago
Km. 3.5+1.8, Comunidad de Palo Blanco, C. P. 36885,
Salamanca, Guanajuato, México
E-MAIL: carlos.arellano@uaslp.mx

Received:

8 June 2021

Accepted:

3 September 2021

INTRODUCTION

Human gait is a complex process that involves many systems such as bones, joints, muscles, peripheral nerves, spinal cord, and the brain. When one, or some, of these systems fail or present some limitations, the gait process is altered and becomes a pathological gait [1] [2] [3] [4]. Therefore, the analysis of the human gait represents an important instrument for the early and timely identification of pathologies, and a component of follow-up rehabilitation programs [5] [6] [7] [8] [9]. In addition, gait analysis is also important to the design of equipment, devices, rehabilitation systems, prostheses, orthoses, and humanoid robots [10] [11] [12] [13] [14]. Moreover, it can be used in sports science to improve the techniques and performance of athletes. However, such a diagnostic tool requires the use of biomechanical parameters to characterize and evaluate the human gait performance.

Several research works have undertaken the assessment of human gait as a prevention, monitoring, and diagnostic tool. For example, it can be possible to avoid foot ulcers in diabetic patients by increasing foot motion during the intermedia stance phase of the gait cycle [15]. Patients with knee osteoarthritis (KOA) often adopt a type of antalgic gait as their disease progresses [16]. These patients generally try to protect the damaged knee by biomechanical adaptations that may affect the movement of the joints of the lower extremities and the lower back [17] [18]. Gait and balance abnormalities have been described even at early stages in the diagnosis of Alzheimer's ailment [19]. Similarly, a fall during gait can be the result of specific characteristics of gait disturbances related to neurological disorders [20]. Additionally, it has been observed that robotic gait rehabilitation can improve the biomechanical parameters in chronic hemiplegic patients [21].

Numerous biomechanical parameters have been used in the analysis of the human gait. It was reported that gait patterns and parameters values often vary with

the gait velocity [22], a parameter used to identify groups of elderly patients who are at increased risk of death and serious morbidity after cardiac surgery [23]. The spatiotemporal parameters have been related to the gait mechanics of the KOA progression [24] [25] [26]. Cadence, stride length, and gait velocity are the main gait parameters that provide a general idea of how well patients can walk [27]. In addition, the joint angles of the knee flexion and leg shortening effect parameters are very relevant when analyzing the kinematics of the knee and designing knee prostheses [28].

Over time, the interest in analyzing the performance and characteristics of human gait through biomechanical parameters has increased because human gait alterations can be associated with pathologies known to cause bad body postures and muscle imbalance [19] [29] [30] [31] [32]. However, in the clinical area the gait analysis still relies on the knowledge and experience of the specialist, which represents a certain degree of subjectivity. In addition, few studies have correlated the gait parameters and metrics with clinical problems such as musculoskeletal, neurological, and circulatory problems [33]. Furthermore, there is not a comprehensive baseline study to ease the understanding and selection of biomechanical parameters for normal and pathological gait analyses. Therefore, the objective of this research work is to identify and analyze the main biomechanical parameters commonly used in the assessment of human gait.

MATERIALS AND METHODS

Literature search

A literature review was carried out to identify research papers dealing with biomechanical parameters used in the human gait analysis. Original articles published in scientific journals indexed in PubMed, Web of Science, Scopus, Science Direct, and Google Scholar, were considered. Although no date of publication limits were used, papers published during the last ten years were mainly considered to identify the latest

advances. The keywords and mesh terms related to human gait (gait and walking), type of gait (normal, healthy, pathological, hemiplegic, parkinsonian, paraparetic, dancer, apraxic, ataxic, vestibular, equinus, steppe, multisensory deficits, diabetic, prudent, senile, antalgic, dysmetric, Trendelenburg, and claudic), and biomechanical parameters, (temporal, spatial, spatiotemporal, angular, force, strength, kinematic, and kinetic), were used in the search.

In the first search, 380 publications were selected. Next, the title, abstract, and conclusions of each paper were reviewed and the following selection criteria applied: 1) the study should be based on a quantitative analysis of pathological or healthy gait, 2) the study should report the analysis of pathological gaits caused by neurological, musculoskeletal and circulatory problems, 3) the study should use kinematic and kinetic parameters, and other particular parameters according to the case study or pathology, 4) the study should indicate application areas, and 5) priority was given to

papers that included the use of three-dimensional digital measurements in gait analysis. The first three criteria were mandatory and the last two were desired. Two independent researchers (authors) conducted searches by applying the criteria and resolving discrepancies. A total of 144 papers were finally selected.

Analysis of the parameters

In order to identify the most important biomechanical parameters reported in the literature, the selected papers were analyzed in detail. Then a classification of the gait parameters was established according to the following application areas: clinical, sports, and research. Furthermore, the parameters used in the analysis of pathological gaits were identified and classified according to the cause of the pathology as: circulatory, musculoskeletal, and neurological. Finally, set theory was used to systematically analyze the biomechanical parameters, and to facilitate their selection according to the application area. The complete flow chart of the methodology used in this study is shown in Figure 1.

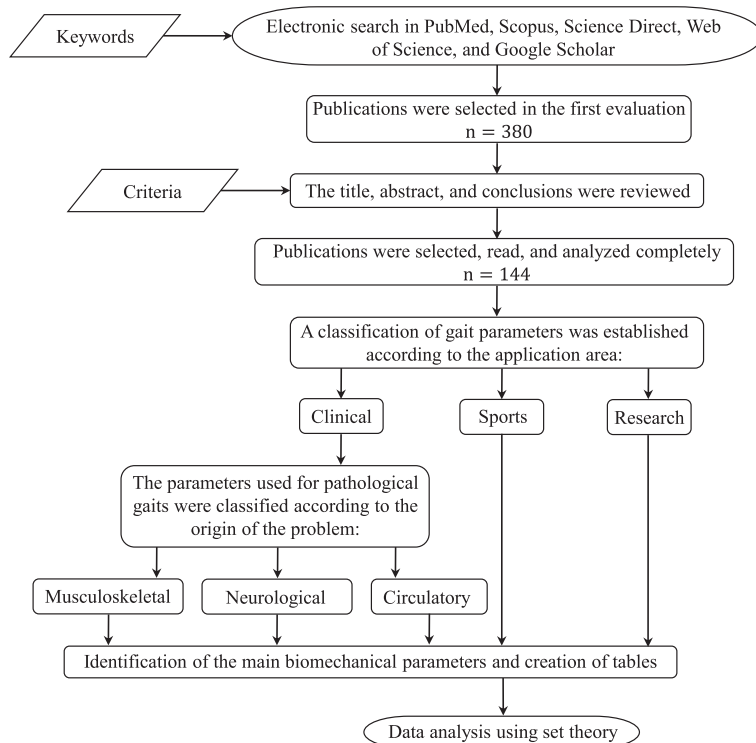


FIGURE 1. Methodology used in the review and analysis of the gait parameters.

RESULTS AND DISCUSSION

Demographic and anthropometric data

The demographic and anthropometric information of the patient is essential when conducting a gait analysis. Table 1 summarizes the demographic and anthropometric parameters reported in the literature.

The demographic data comprises general information about the group of people such as age, gender, place of residence, as well as social or economic characteristics such as occupation, marital status, etc. The most common demographic data used for gait analysis are age and gender.

Table 1 also describes the anthropometric data used in gait analyses. Since computer vision systems, tracking systems, or force plates are commonly used in gait studies, it is important in the collection of anthropometric data to have a robust benchmark that can be used to calibrate the vision system, define the dimensions of the walkway, locate the force plates, etc. [34] [35] [36]. A tendency to decrease the amount of anthropometric information required in gait analyses was also observed [37] [38] [39].

Gait analysis applications

In general, six main application areas were identified and the percentage of each calculated, Table 2 [40] [41] [42] [43] [44] [45] [46] [47] [48] [49] (based on the number of uses in each application area relative to the total number of

TABLE 1. Anthropometric and demographic data required for human gait analysis.

	Data	Description
Anthropometric	Ankle width	The anthropometric length between the lateral and medial malleolus of each leg.
	ASIS width	The horizontal distance between the anteroposterior iliac spines.
	Body mass index	A key index for relating weight to height.
	Bodyweight	The force that induces the gravity on the human body.
	Foot length	The anthropometric length between the heel and the big toe.
	Foot width	The anthropometric length between the first and fifth metatarsal heads.
	Knee width	The anthropometric length between the lateral and medial epicondyles of the femur.
	Lower leg length	The anthropometric length between the lateral femoral condyle and the lateral malleolus.
	Pelvic height	The anthropometric length between the superior iliac crest and the ischium when seated on a stiff chair.
	Pelvic width	The anthropometric length between the right and left superior iliac crests.
Demographic	Standing height	The height of a person from foot to head.
	Thigh-length	The anthropometric length between the greater trochanter and the lateral femoral condyle.
	Age	The time that a person has lived (in years).
	Duration of the disease	The elapsed time of having a disease condition (in years).
	Gender	Male/Female.
	Marital status	The status of a person according to the civil registration.
	Employment	The activity where a person is hired to perform a series of specific tasks.
	Place of birth	City, state, and country where she/he was born.
	Residence	Place where she/he lives.

uses). The six application areas were then rearranged into three generic types: clinical (56%), research (31%), and sports (13%) applications; similarly, as reported by Muro-de-la-Herran [33].

TABLE 2. Main applications of gait analysis and proposed classification.

Applications of gait analysis	Use (%)	Proposed classification	Use (%)
Diagnosis	25		
Rehabilitation	31	Clinical	56
Art and entertainment	9		
Ergonomics and industrial applications	13	Research	31
Fundamental and applied research	9		
Sports	13	Sports	13

Gait parameters

In the literature, human gait biomechanical parameters have been classified in several ways. However, all the classifications converge on the use of spatial, temporal, angular, and strength biomechanical parameters. Table 3 presents the biomechanical parameters most used in the literature for gait analysis. In this table, each parameter has been classified, defined, and identified according to the application area.

In order to systematically analyze the biomechanical parameters, set theory is used. Three sets **A**, **B** and **C** are defined and correspond to the parameters used in clinical, research, and sports applications, respectively. The common parameters among the three sets are given by the intersection of the three sets, as shown in Figure 2.

Figure 2 shows that the spatiotemporal parameters predominate in the three application areas. Notice that between the research and the sports sets, and between the research and the clinical sets, there are no common parameters besides those parameters described

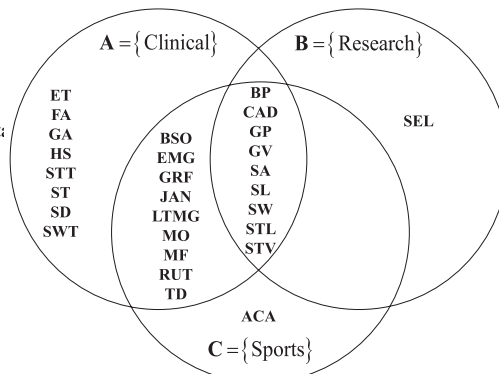


FIGURE 2. Gait parameters used in clinical, sports, and research applications.

by the intersection **A ∩ B ∩ C**. This suggests that clinical applications make use of most of the biomechanical parameters used in gait analysis.

Clinical gait parameters

The disability due to gait problems represents approximately 55% of the total disabilities worldwide [50]. These gait disorders may be a consequence of various pathologies, which are known to disturb human motor functions. The most common semiology of the pathological processes that affect human gait is pain, limitation of movement, muscular weakness, and deficit of neurological control [29] [51]. Consequently, the study of the characteristics of human gait by means of biomechanical parameters represents a potential tool for the diagnosis, treatment and monitoring of some pathologies. In the literature, many gait pathologies have been analyzed and classified according to the root cause of the functional impairment [27] [29] [33] [51]. Based on a preliminary study [52], three large groups of pathologic causes are proposed: neurological, musculoskeletal, and circulatory.

Table 4 synthesizes the clinical gait parameters according to the type of pathology, and presents the parameters used in healthy gait analysis, extending the work presented by Muro-de-la-Herran [33]. On the other hand, Table 5 presents the biomechanical parameters and the demographic and anthropometric data used in pathological gait analyses.

TABLE 3. Description of the biomechanical gait parameters and their applications.

Type of parameter	Reference	Biomechanical gait parameters	Acronym	Unit	Definition	Application		
						Clinic	Research	Sports
Spatial	33	Accumulated altitude	ACA	m	The vertical distance traveled.			x
	53-56	Height of step	HS	m	The movement of the lower extremities gives a height to the step, avoiding the drag of the feet.	x		
	28	Shortening effect of the leg	SEL	%	The natural shortening effect of the lower limb in the swing phase, generated by the knee joint to avoid tripping.		x	
	30, 34, 53-65	Step length	SL	m	The distance between the placements of a foot.	x	x	x
	30, 57-60	Step width	SW	m	The distance between two equivalent points of two consecutive footprints.	x	x	x
	30, 34, 53-65	Stride length	STL	m	The distance between the placements of the same foot. A stride is equivalent to a complete gait cycle.	x	x	x
	53-56	Traveled distance	TD	m	The length of the journey traveled.	x		x
	30, 34, 53-65	Cadence	CAD	steps/min	The number of steps taken in a time interval.	x	x	x
Temporal	53-56	Gait autonomy	GA	min	The maximum time that a person can walk, considering the number and duration of stops.	x		
	30, 34, 53-65	Gait phases	GP	%	Set of divisions of the gait cycle.	x	x	x
	30, 34, 53-65	Gait velocity	GV	m/s	The distance traveled in a defined time interval.	x	x	x
	30, 34, 53-65	Stance time	STT	s	The time elapsed from the moment that the heel touches the ground until the toes are lifted, for each foot.	x		
	30, 34, 53-60, 64-66	Step time	ST	s	The time elapsed between the placement of one foot and the placement of the other.	x		
	53-56	Stop duration	SD	s	The time in which both feet are on the ground, without being part of a gait phase.	x		
	34, 53-56, 64-66	Stride velocity	STV	m/s	The distance traveled in one stride in a defined time interval.	x	x	x
	30, 34, 53-65	Swing time	SWT	s	The time elapsed from when the foot is lifted off the ground until it touches it again, for each foot.	x		

Application								
Type of parameter	Reference	Biomechanical gait parameters	Acronym	Unit	Definition	Clinic	Research	Sports
Angular	30, 53-60	Body posture (inclination, symmetry)	BP	°	The direction of a corporal segment with respect to geometric references (usually the conventional references).	x	x	x
	30, 34, 53-60, 64-66	Body segment orientation	BSO	°	Geometric description of the behavior of the body referenced to geometric entities.	x		x
	30, 34, 53-60, 64-66	Joint angles	JAN	°	The angle between two members due to the biomechanical movements of the joints (hip, knee, ankle).	x		x
	30, 53-60	Step angle	SA	°	Direction of the foot during the step.	x	x	x
Force	30, 34, 53-60, 64-66	Ground reaction forces	GRF	N	The forces generated on the floor due to weight and walking.	x		x
	30, 53-63	Momentum	MO	N·m	Measurement of the rotating potential that a joint performs against a force to a specific line.	x		x
	30, 34, 53-60, 64-66	Muscle activation index	EMG	mV	Electrical activity produced by muscles.	x		x
	30, 53-60	Muscle force	MF	N	The forces generated in the limbs due to the action of the contractions and tractions of the muscles.	x		x
Others	53-56	Existence of tremors	ET	Yes/ No	Presence of disturbances in the form of oscillation patterns.	x		
	53-56	Falls	FA	Yes/ No	Any event that precipitates the individual to the ground against his will.	x		
	53-56	Long-term monitoring of gait	LTMG	h, d	The monitoring history of the gait behavior in an established period.	x		x
	53-56	Route	RUT	-	Specification of the path walked on the walkway. This path can be straight or curve.	x		x

ANALYSIS AND DISCUSSION

Pathological and healthy gaits

Figure 3 shows the biomechanical parameters used in the assessment and analysis of pathological and healthy (normal) gaits, referred to as set **P** and **H**, respectively. It is observed that in the study of pathological gaits most of the gait parameters reported in the literature are used. The spatiotemporal parameters predominate in the study of both pathological and healthy gaits.

As shown in Table 5, most of the spatiotemporal and angular parameters are used in the analysis of pathological gaits caused by neurological disorders. For instance, *senile* gait studies all the spatiotemporal and angular parameters except the *distance traveled*, *step angle*, and *body posture* are used. The literature also suggests that the *step height* parameter is mainly used in the study of *prudent* and *senile* pathological gaits, the *traveled distance* is used in the analysis of *dancer* gait, and the *stop duration* temporal parameter is used in the

TABLE 4. Synthesis of the gait parameters according to the type of pathology.

		Pathological gait according to the origin of the problem				
Type of parameter	Gait parameter	Acronym	Neurological [19, 20, 53-56, 67-128]	Musculoskeletal [30, 57-60, 129-142]	Circulatory [61-63, 143]	Healthy gait [34, 64-66, 144-147]
Spatial	Step height	HS	X			
	Step length	SL	X	X	X	X
	Step width	SW	X	X	X	
	Stride length	STL	X	X	X	X
Temporal	Traveled distance	TD	X			
	Cadence	CAD	X	X	X	X
	Gait autonomy	GA	X			
	Gait phases	GP	X	X	X	X
	Gait velocity	GV	X	X	X	X
	Stance time	STT	X	X	X	X
	Step time	ST	X	X		X
	Stop duration	SD	X			
	Stride velocity	STV	X			X
Angular	Swing time	SWT	X	X	X	X
	Body posture	BP	X	X		
	Body segment orientation	BSO	X	X		X
	Joint angles	JAN	X	X		X
Force	Step angle	SA	X	X		
	Ground reaction forces	GRF	X	X		X
	Momentum	MO	X	X	X	
	Muscle activation index	EMG	X	X		X
	Muscle force	MF	X	X		
Others	Existence of tremors	ET	X			
	Falls	FA	X			
	Long-term monitoring of gait	LTMG	X			
	Route	RUT	X			

study of *Parkinsonian* and *senile* gaits. Likewise, in the study of *Parkinsonian* and *ataxic cerebellar* pathological gaits, all *angular* parameters are used; in contrast, in the analysis of *prudent* pathological gaits these *angular* parameters are not used. The *joint angles* and *body segment orientation* parameters are commonly used in the analysis of *hemiplegic*, *Parkinsonian*, *paraparetic*, *dancer*, *cerebellar ataxic*, *equinus*, and *senile* gaits.

On the other hand, the analysis of pathologic gaits caused by musculoskeletal disorders makes use of many spatio-temporal parameters, and all angular parameters. In the *antaligic* gait analysis, the *ground reaction force* and the *momentum* parameters are used, whilst in the study of *dysmetric* and *Trendelenburg* gaits the *muscle force* parameter is used. Regarding other parameters, the *gait phases* parameter is used in the analysis of musculoskeletal pathologies.

TABLE 5. Gait parameters and data for pathological and healthy gaits.

Type of parameters		Pathological Gait (Origin of the problem)														
		Neurological														
Spatial		Biomechanical gait parameters						Abnormalities associated with multisensory deficits								
		Hemiplegic [53-56, 67, 68]	Paraparetic (in scissors) [74-78]	Dancer (typical of Korea) [79-86]	Apraxic [20, 87-89]	Ataxic (taloneant) [90-93]	Ataxic (cerebellar) [94-99]	Vestibular (star or compass) [100-106]	Equinus (step)e [107-112]	Prudent [113-118]	Senile [123-128]	Antalgic [30, 57-60, 129-132]	Dysmetric [133-137]	Trendelenburg [138-142]	Claudic [61-63, 143]	Healthy Gait [34, 64-66, 144-147]
		Step height	X	X	X	X	X	X	X	X	X	X	X	X	X	
		Step length	X	X	X	X	X	X	X	X	X	X	X	X	X	
		Step width	X	X	X	X	X	X	X	X	X	X	X	X	X	
		Stride length	X	X	X	X	X	X	X	X	X	X	X	X	X	
Temporal		Traveled distance			X											
		Cadence	X	X	X	X	X	X	X	X	X	X	X	X	X	
		Gait autonomy				X			X							
		Gait phases	X	X					X	X	X	X	X	X	X	
		Gait velocity	X	X	X	X	X	X	X	X	X	X	X	X	X	
		Stance time	X	X	X	X	X	X	X	X	X	X	X	X	X	
		Step time	X							X		X			X	
		Stop duration	X								X				X	
		Stride velocity								X	X	X			X	
Angular		Swing time	X	X	X	X	X	X	X	X	X	X	X	X	X	
		Body posture	X			X		X	X			X	X	X		
		Body segment orientation	X	X	X	X		X		X		X	X	X	X	
		Joint angles	X	X	X	X	X	X	X	X	X	X	X	X	X	
		Step angle	X			X	X					X			X	

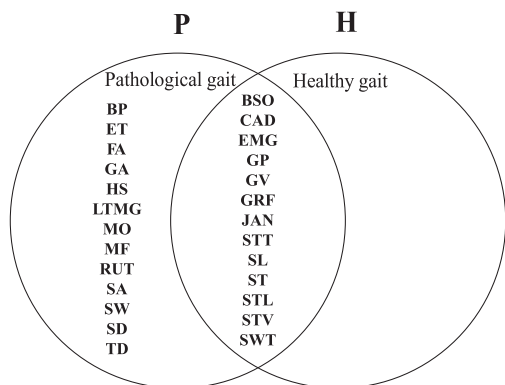


FIGURE 3. Parameters used in the study of pathological and healthy gaits.

The main circulatory pathological gait reported in the literature is the *claudic* gait, which requires several *spatiotemporal* parameters, and the *momentum* and *gait phases* parameters. The *gait phases* parameter is important in order to identify the most critical phase or phases of this pathological gait.

Figure 4 shows the gait parameters used to analyze Musculoskeletal, Neurological, and Circulatory pathologies, referred to as sets **M**, **N**, and **R**, respectively. In this figure, the common parameters used for these pathologies correspond to the intersection of the three sets. On the other hand, the common parameters between the musculoskeletal and neurological pathologies, besides those given by the intersection: **M**∩**N**∩**R**, are: *muscle activation index*, *step angle*, *step time*, *body posture*, *muscle strength*, *joint angles*, *body segment orientation*, and *ground reaction forces*. It is observed that the analysis of neurological pathologies demands the use of all the parameters, whereas the analysis of circulatory pathologies makes use of the common parameters of the three clinical applications.

Spatial parameters

Figure 5(a) shows the spatial parameters used in the analysis of pathological and healthy gaits. It is observed that the common parameters used for both pathological and healthy gaits are the *step length* and *stride length*. On the other hand, the most common

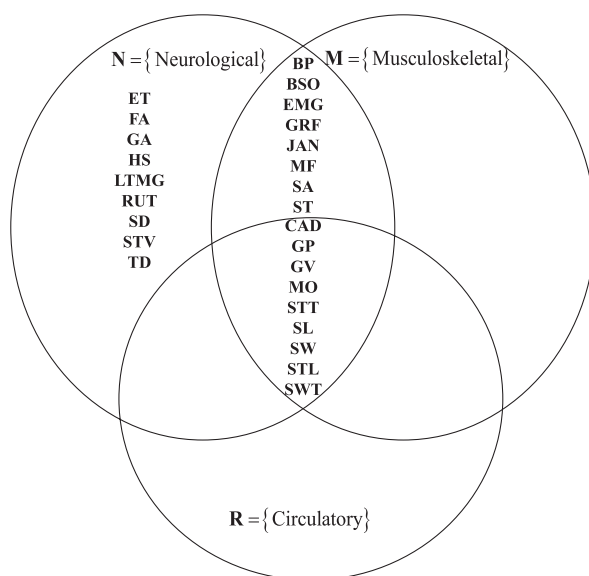


FIGURE 4. Gait parameters used to analyze pathological gaits.

spatial parameters used in pathological gait studies are the *step length*, *step width*, and *stride length*. The *traveled distance* and *height of step* are mainly used in the study of pathological gait because of neurological disorders.

Temporal parameters

Figure 5(b) shows that the *gait velocity*, *cadence*, *gait phases*, *swing time*, and *stance time* parameters are the most used temporal parameters, and they correspond to the intersection of the four sets **H**∩**M**∩**N**∩**R**. The *step time* is the most common parameter in the study of healthy gaits, and musculoskeletal, and neurological gaits. The *stride velocity* parameter is used in neurological and healthy gait analyses. The *gait autonomy* and *stop duration* parameters are only used in the analysis of pathological gait caused by neurological disorders.

Angular parameters

Figure 5(c) shows the common angular parameters used in the analysis of healthy, musculoskeletal, and neurological gaits. The literature also suggests that the analysis of pathological gaits due to circulatory prob-

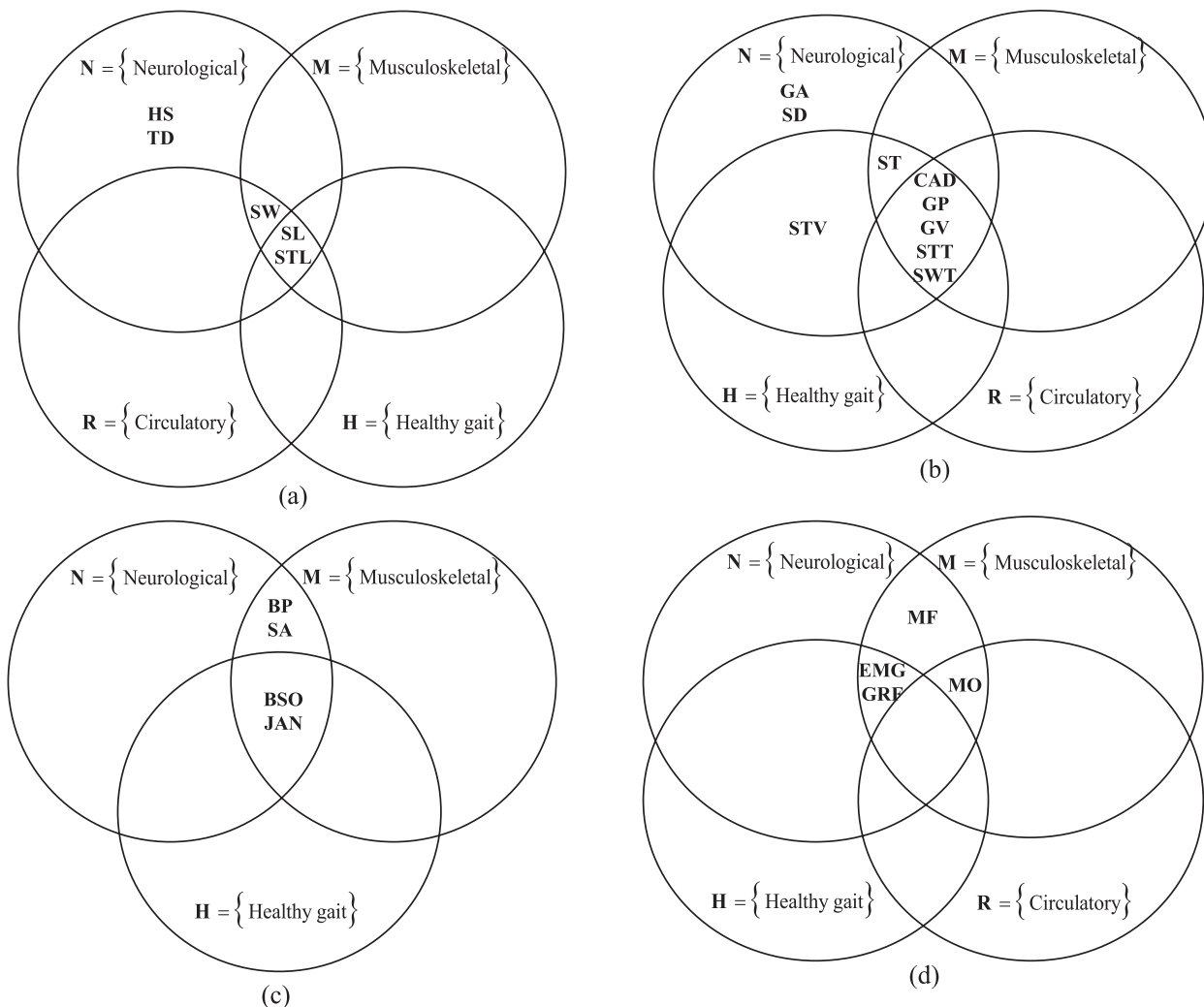


FIGURE 5. Gait parameters used in the analysis of pathological and healthy gaits:

a) Spatial gait parameters, b) Temporal gait parameters, c) Angular gait parameters, and d) Force gait parameters.

lems does not use angular parameters [31] [32] [33]. The angular parameters *BP* and *SA* are mainly used in the assessment of pathological gaits caused by musculoskeletal and neurological problems.

Force parameters

Figure 5(d) shows that the *EMG* and *GRF* are frequent force parameters used in the analysis of musculoskeletal, neurological, and healthy gaits. The *MF* parameter is mainly used in the analysis of musculoskeletal and neurological pathologies, whilst the *MO* parameter has only been used in pathological gait studies.

Ranking of parameters

In order to rank the biomechanical parameters used in the analysis of pathological and healthy gaits, two criteria were defined: 1) the relevance of the parameter in the research studies, and 2) the frequency, which was calculated using the following expression:

$$f = 100n/144 \quad (1)$$

where *f* is the frequency percentage, *n* is the number of times the parameter was used in the selected papers. A normalization process was then considered, given a value of 1 to the most used parameter. Regarding the

relevance criterion, a value of 1 was given to those parameters with the largest reliability, the most common in different gait analysis (set theory), and the most cited. A relevance value of 0 was assigned to the rest of the parameters. Table 6 shows the results, where it is observed that *gait velocity* is the most frequently used parameter in the study of human gait because it assesses the functional mobility of an individual and affects his/her gait pattern. Moreover, most of the biomechanical parameters decrease at slower gait velocities and increase at faster gait velocities.

The next most used parameters are *cadence*, *stance time*, *step length*, and *stride length*. It is also observed that the spatiotemporal and angular biomechanical parameters are the most used in the study of both pathological and healthy gaits. The least popular biomechanical parameters reported in the literature are *traveled distance*, *long-term monitoring of gait*, and *route*, which are specific for the evaluation of *dancer*, *ataxia (taloneant)*, and *vestibular* pathologies, respectively. Notice that although these parameters are not very popular parameters, they may be as important as the spatiotemporal parameters for some particular pathologies. The results also revealed that the temporal parameters are the most popular with 37% of use, followed by the spatial parameters with 24%, the angular parameters with 18%, the force parameters with 8%, and others with 13%.

According to Whittle MW [27], the cadence, gait velocity, and stride length parameters provide a general idea of how well a patient walks. However, the results of this research work suggest that the stance time is also important. For instance, in the study of musculoskeletal-related gait pathologies [57] [60] [140] [142], the stance time is an indicator of the improvement or deterioration of the pathology. On the other hand, although the stride length of both limbs may be the same, the step length of each limb may be different, as reported by Kirtley C [148]; for this reason, many studies have

considered it relevant. The step width is another relevant parameter, [67] [68] [143] [148], which tends to increase with a balance disorder.

General discussion

The proposed analysis and classification of the gait parameters represent a general and practical guide to select the parameters for healthy or pathological gait studies. In general, the *spatiotemporal* and *angular* parameters are the most used because they allow a detailed and objective study of the human gait. However, other parameters are specific and important for particular pathologies, such as the *cartilage thickness* [149], which is used in the study of antalgic gait due to knee or hip osteoarthritis. In this work, only the most general pathologies and parameters reported in the literature have been considered.

It was also observed that most of the pathological gait studies (90%) reported in the literature were conducted on a walkway instead of an electric treadmill. This is because in the analysis of pathological gaits, the *gait velocity* is a parameter that depends on the pathology, and the evolution and progress of the patient. In contrast, in the studies related to healthy gait, the *gait velocity* is usually an independent variable that is defined and varied using an electric treadmill.

The *stance time* parameter is indicative of the improvement, or severity of pain, in the antalgic gait caused by knee osteoarthritis [131]. For example, an increment of the stance time is an indication that the pain experienced by the patient is less and therefore the support of the loading has improved. The use of the *step height* parameter has not been reported in the literature; however, it can be used in the study of musculoskeletal pathological gaits since it is closely linked to the angular parameter of the knee articulation. The *step height* parameter may vary due to musculoskeletal pathologies or due to the use of certain footwear, such as the use of high heels, as reported by Arellano [28].

TABLE 6. General ranking of gait parameters based on their relevance and frequency of use in the literature.

Gait parameters	Relevance value	% frequency of use	Frequency value	Relevance and frequency value	Ranking
Gait velocity	1	8.76	1.00	2.00	1
Cadence	1	7.73	0.88	1.88	
Stance time	1	7.73	0.88	1.88	2
Step length	1	7.73	0.88	1.88	
Stride length	1	7.73	0.88	1.88	
Step width	1	7.22	0.82	1.82	3
Joint angles	1	6.70	0.76	1.76	
Swing time	1	6.70	0.76	1.76	4
Gait phases	1	5.67	0.65	1.65	5
Ground reaction forces	1	3.09	0.35	1.35	6
Muscle activation index	1	2.06	0.24	1.24	7
Body segment orientation	0	5.67	0.65	0.65	8
Body posture	0	3.61	0.41	0.41	9
Falls	0	2.58	0.29	0.29	
Momentum	0	2.58	0.29	0.29	10
Step time	0	2.58	0.29	0.29	
Muscle force	0	2.06	0.24	0.24	
Step angle	0	2.06	0.24	0.24	11
Stride velocity	0	2.06	0.24	0.24	
Existence of tremors	0	1.03	0.12	0.12	
Gait autonomy	0	1.03	0.12	0.12	
Step height	0	1.03	0.12	0.12	12
Stop duration	0	1.03	0.12	0.12	
Long-term monitoring of gait	0	0.52	0.06	0.06	
Route	0	0.52	0.06	0.06	13
Traveled distance	0	0.52	0.06	0.06	

The *leg shortening effect* parameter is also an important parameter that has been mentioned qualitatively in some works, but a complete quantitative study has not been reported yet. This *leg shortening effect* may be relevant when designing knee prostheses.

Finally, it can be said that most of the research works related to pathological gait have been conducted considering only intrinsic conditions such as age, gender, weight, etc., or the type of pathology. Few studies have considered both intrinsic and extrinsic conditions

such as climbing slopes, walking with a front-load, using a certain type of footwear, walking whilst texting or calling by cell phone, etc.

CONCLUSIONS

A review and analysis of the main biomechanical gait parameters used in the literature to study pathological and healthy gaits has been presented. The gait parameters have been identified and classified according to the type of physical quantity (spatial, temporal, angular, force and others) and according to the application

area (clinical, sports and research). The clinical applications were subdivided according to the pathological disorder into neurological, musculoskeletal, and circulatory applications, being the neurological area the one that uses most of the gait parameters. The overall most common parameters are body posture, cadence, gait phases, gait velocity, step angle, step length, step width, stride length, and stride velocity. Finally, it can be said that the results presented in this investigation can be used as a practical guide to identify and select the main biomechanical parameters commonly used in the analysis and monitoring of human gaits under pathological or normal conditions.

AUTHOR CONTRIBUTIONS

The four authors participated in all the stages of the project from the conceptualization to the writing of the manuscript. In this sense, each author participated in the following roles: J.C.A.G. contributed to the conceptualization, data curation, formal analysis, investigation, methodology, visualization, and writing the

original draft. H.I.M.C. contributed to the conceptualization, formal analysis, investigation, project administration, resources, supervision, validation, writing original draft, and writing, reviewing, and editing the final version. J.J.C.S. contributed to the conceptualization, validation, visualization, and writing, reviewing, and editing the final version. A.V.L. contributed to the conceptualization, validation, and writing, reviewing, and editing the final version.

ACKNOWLEDGMENTS

The first author acknowledges the Program for Professional Development of Academics (PRODEP) of the Secretary of Public Education (SEP) of Mexico, for the scholarship provided during his Ph.D. studies. The authors would like to thank Professor Jonathan Corney from University of Edinburgh for his help and advice to this work.

CONFLICTS OF INTEREST

The authors do not report any conflict of interest.

REFERENCES

- [1] Detrembleur C, van den Hecke A, Dierick F. Motion of the body centre of gravity as a summary indicator of the mechanics of human pathological gait. *Gait Posture* [Internet]. 2000;12(3):243-250. Available from: [https://doi.org/10.1016/S0966-6362\(00\)00081-3](https://doi.org/10.1016/S0966-6362(00)00081-3)
- [2] Khokhlova M, Mignot C, Morozov A, Sushkova O, et al. Normal and pathological gait classification LSTM model. *Artif Intell Med* [Internet]. 2019;94:54-66. Available from: <https://doi.org/10.1016/j.artmed.2018.12.007>
- [3] Moreno-Hernández A, Rodríguez-Reyes G, Quiñones-Urióstegui I, Núñez-Carrera L, et al. Temporal and spatial gait parameters analysis in non-pathological Mexican children. *Gait Posture* [Internet]. 2010;32(1):78-81. Available from: <https://doi.org/10.1016/j.gaitpost.2010.03.010>
- [4] Bruening DA, Ridge ST. Automated event detection algorithms in pathological gait. *Gait Posture* [Internet]. 2014;39(1):472-477. Available from: <https://doi.org/10.1016/j.gaitpost.2013.08.023>
- [5] Phinyomark A, Osis ST, Hettinga BA, Kobsar D, et al. Gender differences in gait kinematics for patients with knee osteoarthritis. *BMC Musculoskelet Disord* [Internet]. 2016;17:157. Available from: <https://doi.org/10.1186/s12891-016-1013-z>
- [6] Smith Y, Louw Q, Brink Y. The three-dimensional kinematics and spatiotemporal parameters of gait in 6-10 years old typically developed children in the cape metropole of South Africa - a pilot study. *BMC Pediatr* [Internet]. 2016;16:200. Available from: <https://doi.org/10.1186/s12887-016-0736-1>
- [7] Washabaugh EP, Augenstein TE, Krishnan C. Functional resistance training during walking: Mode of application differentially affects gait biomechanics and muscle activation patterns. *Gait Posture* [Internet]. 2020;75:129-136. Available from: <https://doi.org/10.1016/j.gaitpost.2019.10.024>
- [8] Simon SR. Quantification of human motion: gait analysis-benefits and limitations to its application to clinical problems. *J Biomech* [Internet]. 2004;37(12):1869-1880. Available from: <https://doi.org/10.1016/j.jbiomech.2004.02.047>
- [9] Naili JE, Wretenberg P, Lindgren V, Iversen MD, et al. Improved knee biomechanics among patients reporting a good outcome in knee-related quality of life one year after total knee arthroplasty. *BMC Musculoskelet Disord* [Internet]. 2017;18:122. Available from: <https://doi.org/10.1186/s12891-017-1479-3>
- [10] Hussain S, Xie SQ, Jamwal PK. Control of a robotic orthosis for gait rehabilitation. *Robot Auton Syst* [Internet]. 2013;61(9):911-919. Available from: <https://doi.org/10.1016/j.robot.2013.01.007>
- [11] Khas KS, Pandey PM, Ray AR. Development of an orthosis for simultaneous three-dimensional correction of clubfoot deformity. *Clin Biomech* [Internet]. 2018;51:67-75. Available from: <https://doi.org/10.1016/j.clinbiomech.2017.12.002>
- [12] Arnez-Paniagua V, Rifai H, Amirat Y, Ghedira M, et al. Adaptive control of an actuated ankle foot orthosis for paretic patients. *Control Eng Pract* [Internet]. 2019;90:207-220. Available from: <https://doi.org/10.1016/j.conengprac.2019.06.003>
- [13] Kobayashi T, Orendurff MS, Singer ML, Gao F, et al. Contribution of ankle-foot orthosis moment in regulating ankle and knee motions during gait in individuals post-stroke. *Clin Biomech* [Internet]. 2017;45:9-13. Available from: <https://doi.org/10.1016/j.clinbiomech.2017.04.002>
- [14] Segal AD, Orendurff MS, Klute GK, McDowell ML, et al. Kinematic and kinetic comparisons of transfemoral amputee gait using C-Leg® and Mauch SNS® prosthetic knees. *J Rehabil Res Dev* [Internet]. 2006;43(7):857-870. Available from: <https://doi.org/10.1682/jrrd.2005.09.0147>
- [15] Amemiya A, Noguchi H, Oe M, Ohashi Y, et al. Elevated plantar pressure in diabetic patients and its relationship with their gait features. *Gait Posture* [Internet]. 2014;40(3):408-414. Available from: <https://doi.org/10.1016/j.gaitpost.2014.05.063>
- [16] Bejek Z, Paróczai R, Illyés Á, Kocsis L, et al. Gait parameters of patients with osteoarthritis of the knee joint. *Phys Educ Sport* [Internet]. 2006;4(1): 9-16. Available from: <http://facta.junis.ni.ac.rs/pe/pe2006/pe2006-02.pdf>
- [17] Andriacchi TP, Galante JO, Fermier RW. The influence of total knee replacement design on walking and stair-climbing. *J Bone Joint Surg Am* [Internet]. 1982;64(9):1328-1335. Available from: <https://doi.org/10.2106/00004623-198264090-00008>
- [18] Gök H, Ergin S, Yavuzer G. Kinetic and kinematic characteristic of gait in patients with medial knee arthrosis. *Acta Orthop Scand* [Internet]. 2002;73(6): 647-652. Available from: <https://doi.org/10.3109/17453670209178029>
- [19] Tangen GG, Bergland A, Engedal K, Mengshoel AM. The importance of parkinsonian signs for gait and balance in patients with Alzheimer's disease of mild degree. *Gait Posture* [Internet]. 2017;51:159-161. Available from: <https://doi.org/10.1016/j.gaitpost.2016.10.00>
- [20] Axer H, Axer M, Sauer H, Witte OW, et al. Falls and gait disorders in geriatric neurology. *Clin Neurol Neurosurg* [Internet]. 2010;112(4):265-274. Available from: <https://doi.org/10.1016/j.clineuro.2009.12.015>
- [21] Wallard L, Dietrich G, Kerlirzin Y, Brendin J. Effects of robotic gait rehabilitation on biomechanical parameters in the chronic hemiplegic patients. *Clin Neurophysiol* [Internet]. 2015;45(3):215-219. Available from: <https://doi.org/10.1016/j.neucli.2015.03.002>
- [22] Van Der Krogt M, Doorenbosch C, Becher J, Harlaar J. Po80 Gait patterns vary with walking speed. *Gait Posture* [Internet]. 2008;28(2S): S49-S118. Available from: [https://doi.org/10.1016/S0966-6362\(08\)70149-8](https://doi.org/10.1016/S0966-6362(08)70149-8)
- [23] Afilalo J, Eisenberg MJ, Morin JF, Bergman H, et al. Gait Speed as an Incremental Predictor of Mortality and Major Morbidity in Elderly Patients Undergoing Cardiac Surgery. *J Am Coll Cardiol* [Internet]. 2010;56(20):1668-1676. Available from: <https://doi.org/10.1016/j.jacc.2010.06.039>
- [24] Mills K, Hunt MA, Ferber R. Biomechanical Deviations During Level Walking Associated With Knee Osteoarthritis: A Systematic Review and Meta-Analysis. *Arthritis Care Res* [Internet]. 2013;65(10):1643-1665. Available from: <https://doi.org/10.1002/acr.22015>
- [25] Duffell LD, Jordan SJ, Cobb JP, McGregor AH. Gait adaptations with aging in healthy participants and people with knee-joint osteoarthritis. *Gait Posture* [Internet]. 2017;57:246-251. Available from: <https://doi.org/10.1016/j.gaitpost.2017.06.015>
- [26] Andriacchi TP, Mündermann A. The role of ambulatory mechanics in the initiation and progression of knee osteoarthritis. *Curr Opin Rheumatol* [Internet]. 2006;18(5):514-518. Available from: <https://doi.org/10.1097/01.bor.0000240365.16842.4e>

- [27] Whittle MW. Clinical gait analysis: A review. *Hum Mov Sci* [Internet]. 1996;15(3):369–387. Available from: [https://doi.org/10.1016/0167-9457\(96\)00006-1](https://doi.org/10.1016/0167-9457(96)00006-1)
- [28] Arellano-González JC, Medellín-Castillo HI, Cárdenas-Galindo JA. Analysis of the kinematic variation of human gait under different walking conditions using computer vision. *RMIB* [Internet]. 2017;38(2):437–457. Available from: <http://dx.doi.org/10.17488/rmib.38.2.2>
- [29] Perry J, Burnfield JM. Gait analysis: Normal and pathological function. 2nd ed., New Jersey: SLACK Incorporated; 2010. 551p.
- [30] Hicks GE, Sions JM, Coyle PC, Pohl RT. Altered spatiotemporal characteristics of gait in older adults with chronic low back pain. *Gait Posture* [Internet]. 2017;55:172–176. Available from: <https://doi.org/10.1016/j.gaitpost.2017.04.02>
- [31] Allet L, Armand S, de Bie RA, Pataky Z, et al. Gait alterations of diabetic patients while walking on different surfaces. *Gait Posture* [Internet]. 2009;29(3):488–493. Available from: <https://doi.org/10.1016/j.gaitpost.2008.11.012>
- [32] Mummo C, Mangialardi L, Kim JH. Quantifying Dynamic Characteristics of Human Walking for Comprehensive Gait Cycle. *J Biomech Eng* [Internet]. 2013;135(9): (9): 091006. Available from: <https://doi.org/10.1115/1.4024755>
- [33] Muro-de-la-Herran A, Garcia-Zapirain B, Mendez-Zorrilla A. Gait Analysis Methods: An Overview of Wearable and Non-Wearable Systems, Highlighting Clinical Applications. *Sensors* [Internet]. 2014;14(2):3362–3394. Available from: <https://doi.org/10.3390/s140203362>
- [34] Kadaba MP, Ramakrishnan HK, Wootten ME. Measurement of lower extremity kinematics during level walking. *J Orthop Res* [Internet]. 1990;8(3):383–392. Available from: <https://doi.org/10.1002/jor.1100080310>
- [35] Frigo C, Rabuffetti M, Kerrigan DC, Deming LC, et al. Functionally oriented and clinically feasible quantitative gait analysis method. *Med Biol Eng Comput* [Internet]. 1998;36(2):179–185. Available from: <https://doi.org/10.1007/BF02510740>
- [36] van den Bogert AJ, Geijtenbeek T, Even-Zohar O, Steenbrink F, et al. A real-time system for biomechanical analysis of human movement and muscle function. *Med Biol Eng Comput* [Internet]. 2013;51(10):1069–1077. Available from: <https://doi.org/10.1007/s11517-013-1076-z>
- [37] Leardini A, Sawacha Z, Paolini G, Ingrosso S, et al. A new anatomically based protocol for gait analysis in children. *Gait Posture* [Internet]. 2007;26(4):560–571. Available from: <https://doi.org/10.1016/j.gaitpost.2006.12.018>
- [38] Sholukha V, Bonnechere B, Salvia P, Moiseev F, et al. Model-based approach for human kinematics reconstruction from markerless and marker-based motion analysis systems. *J Biomech* [Internet]. 2013;46(14):2363–2371. Available from: <https://doi.org/10.1016/j.jbiomech.2013.07.037>
- [39] Benedetti MG, Catani F, Leardini A, Pignotti E, et al. Data management in gait analysis for clinical applications. *Clin Biomech* [Internet]. 1998;13(3):204–215. Available from: [https://doi.org/10.1016/S0268-0033\(97\)00041-7](https://doi.org/10.1016/S0268-0033(97)00041-7)
- [40] Motek. Applications for human movement research and rehabilitation [Internet]; 2021. Available from: <http://www.motekmedical.com/>
- [41] Baker R. Gait analysis methods in rehabilitation. *J NeuroEng Rehabil* [Internet]. 2006;3:4. Available from: <https://doi.org/10.1186/1743-0003-3-4>
- [42] Khan T, Grenholm P, Nyholm D. Computer Vision Methods for Parkinsonian Gait Analysis: A Review on Patents. *Recent Pat Biomed Eng* [Internet]. 2013;6(2):97–108. Available from: <https://doi.org/10.2174/1874764711306020004>
- [43] Ali A, Sundaraj K, Ahmad B, Ahmad N, et al. Gait disorder rehabilitation using vision and non-vision based sensors: A systematic review. *Bosn J of Basic Med Sci* [Internet]. 2012;12(3):193–202. Available from: <https://doi.org/10.17305/bjms.2012.2484>
- [44] Federolf PA, Boyer KA, Andriacchi TP. Application of principal component analysis in clinical gait research: identification of systematic differences between healthy and medial knee-osteoarthritic gait. *J Biomech* [Internet]. 2013;46(13):2173–2178. Available from: <https://doi.org/10.1016/j.jbiomech.2013.06.032>
- [45] Stancic I, Supuk TG, Bonkovic M. New Kinematic Parameters for Quantifying Irregularities in the Human and Humanoid Robot Gait. *Int J Adv Robot* [Internet]. 2017;9(5):1–8. Available from: <https://doi.org/10.5772/54563>
- [46] CAD. Engineering Services, Solutions and services offering [Internet]. 2021; Available from: <http://www.cadengineering.co.in/>
- [47] Bartlett R. Introduction to Sport in Biomechanics: Analyzing Human Movement Patterns. 2nd ed. New York: Taylor & Francis Group; 2007. 292p.
- [48] Huston RL. Principles of biomechanics. 1st ed. NW: Taylor & Francis Group; 2009.
- [49] Knudson D. Fundamentals of biomechanics. 2nd ed. California: Springer; 2007. 319p.
- [50] Center for Disease Control and Prevention. National Center for Health Statistics [Internet]. 2021; Available from: <https://www.cdc.gov/nchs/index.htm>
- [51] Sánchez-Lacuesta J, Prat Pastor JM, Hoyos Fuentes JV, Viosca Herrero E, et al. Biomecánica de la marcha humana patológica. 2nd ed. España: Instituto de Biomecánica de Valencia; 1999. 444p.
- [52] Arellano-González JC, Medellín-Castillo HI, Cervantes-Sánchez JJ. Identification and analysis of the biomechanical parameters used for the assessment of normal and pathological gait: A literature review. Proceedings of the ASME 2019 International Mechanical Engineering Congress and Exposition. Volume 3: Biomedical and Biotechnology Engineering [Internet]. Salt Lake City: ASME; 2019:11–17. Available from: <https://doi.org/10.1115/IMECE2019-10140>
- [53] Granat MH, Maxwell DJ, Bosch CJ, Ferguson AC, et al. A body-worn gait analysis system for evaluating hemiplegic gait. *Med Eng Phys* [Internet]. 1995;17(5):390–394. Available from: [https://doi.org/10.1016/1350-4533\(95\)97321-F](https://doi.org/10.1016/1350-4533(95)97321-F)
- [54] Di Nardo F, Mengarelli A, Malavolta M, Strazza A, et al. Ankle muscle co-contractions in Winters I hemiplegic children during gait. *Gait Posture* [Internet]. 2017;57(S3):4–5. Available from: <https://doi.org/10.1016/j.gaitpost.2017.07.051>

- [55] Gross R, Leboeuf F, Hardouin JB, Perrouin-Verbe B, et al. Does muscle coactivation influence joint excursions during gait in children with and without hemiplegic cerebral palsy? Relationship between muscle coactivation and joint kinematics. *Clin Biomech* [Internet]. 2015;30(10):1088-1093. Available from: <https://doi.org/10.1016/j.clinbiomech.2015.09.001>
- [56] Hussein ZA, Abd-Elwahab MS, El-Shennawy SAW. Effect of arm cycling on gait of children with hemiplegic cerebral palsy. *Egypt J Med Hum Genet* [Internet]. 2014;15(3):273-279. Available from: <https://doi.org/10.1016/j.ejmhg.2014.02.008>
- [57] de Kruijf M, Verlinden VJA, Huygen FJPM, Hofman A, et al. Chronic joint pain in the lower body is associated with gait differences independent from radiographic osteoarthritis. *Gait Posture* [Internet]. 2015;42(3):354-359. Available from: <https://doi.org/10.1016/j.gaitpost.2015.06.193>
- [58] Vickers J, Reed A, Decker R, Conrad BP, et al. Effect of investigator observation on gait parameters in individuals with and without chronic low back pain. *Gait Posture* [Internet]. 2015;53:35-40. Available from: <https://doi.org/10.1016/j.gaitpost.2017.01.002>
- [59] Stewart S, Morpeth T, Dalbeth N, Vandal AC, et al. Foot-related pain and disability and spatiotemporal parameters of gait during self-selected and fast walking speeds in people with gout: A two-arm cross sectional study. *Gait Posture* [Internet]. 2016;44:18-22. Available from: <https://doi.org/10.1016/j.gaitpost.2015.11.004>
- [60] Phillips A, McClinton S. Gait deviations associated with plantar heel pain: A systematic review. *Clin Biomech* [Internet]. 2017;42:55-64. Available from: <https://doi.org/10.1016/j.clinbiomech.2016.12.012>
- [61] Koutakis P, Pipinos II, Myers SA, Stergiou N, et al. Joint torques and powers are reduced during ambulation for both limbs in patients with unilateral claudication. *J Vasc Surg* [Internet]. 2010;51(1):80-88. Available from: <https://doi.org/10.1016/j.jvs.2009.07.117>
- [62] WurdeMAN SR, Koutakis P, Myers SA, Johanning JM, et al. Patients with peripheral arterial disease exhibit reduced joint powers compared to velocity-matched controls. *Gait Posture* [Internet]. 2012;36(3):506-509. Available from: <https://doi.org/10.1016/j.gaitpost.2012.05.004>
- [63] Scherer SA, Bainbridge JS, Hiatt WR, Regensteiner JG. Gait characteristics of patients with claudication. *Arch Phys Med Rehabil* [Internet]. 1998;79(5):529-531. Available from: [https://doi.org/10.1016/s0003-9993\(98\)90067-3](https://doi.org/10.1016/s0003-9993(98)90067-3)
- [64] Pérez-Orive J, Pichardo AE, Chávez-Arias D. Análisis de parámetros cinemáticos de la marcha normal. *Rev Mex Ortop Traum* [Internet]. 1998; 12(5):372-376.
- [65] Dankloff Mora C, Rodríguez R, Fernández-Valencia R. Estudio morfológico de la marcha humana. *J Biomecánica* [Internet]. 1993;1(1):54-58. Available from: <http://hdl.handle.net/2099/6593>
- [66] Díaz-Novo D, López-Ríos N, Montoya-Padrón A, Carvajal Fals H, et al. Evaluación preliminar de la marcha en individuos sanos. Universidad, Ciencia y Tecnología [Internet]. 2007;11(44):135-140. Available from: http://ve.scielo.org/scielo.php?script=sci_arttext&pid=S1316-48212007000300005
- [67] Galli M, Cimolin V, Rigoldi C, Tenore N, et al. Gait patterns in hemiplegic children with Cerebral Palsy: Comparison of right and left hemiplegia. *Res Dev Disabil* [Internet]. 2010;31(6):1340-1345. Available from: <https://doi.org/10.1016/j.ridd.2010.07.007>
- [68] Spaich EG, Hinge HH, Arendt-Nielsen L, Andersen OK. Modulation of the withdrawal reflex during hemiplegic gait: Effect of stimulation site and gait phase. *Clin Neurophysiol* [Internet]. 2006;117(11):2482-2495. Available from: <https://doi.org/10.1016/j.clinph.2006.07.139>
- [69] Ambrose A, LeValley A, Vergheze J. A comparison of community-residing older adults with frontal and parkinsonian gaits. *J Neurol Sci* [Internet]. 2006;248(1-2):215-218. Available from: <https://doi.org/10.1016/j.jns.2006.05.035>
- [70] You-Yin C, Chien-Wen C, Sheng-Huang L, Hsin-Yi L, et al. A vision-based regression model to evaluate Parkinsonian gait from monocular image sequences. *Expert Syst Appl* [Internet]. 2012;39(1):520-526. Available from: <https://doi.org/10.1016/j.eswa.2011.07.042>
- [71] Minji S, Sang-Myung C, Changhong Y, Youkyung K, et al. Impacts of freezing of gait on forward and backward gait in Parkinson's Disease. *Gait Posture* [Internet]. 2018;61:320-324. Available from: <https://doi.org/10.1016/j.gaitpost.2018.01.034>
- [72] Shih-Lin C, Shinn-Zong L, Chung-Chao L, Yi-Sheng S, et al. The efficacy of quantitative gait analysis by the GAITRite system in evaluation of parkinsonian bradykinesia. *Parkinsonism Relat Disord* [Internet]. 2006;12(7):438-442. Available from: <https://doi.org/10.1016/j.parkreldis.2006.04.004>
- [73] Volpea D, Pavan D, Morris M, Guiotto A, et al. Underwater gait analysis in Parkinson's disease. *Gait Posture* [Internet]. 2017;52:87-94. Available from: <https://doi.org/10.1016/j.gaitpost.2016.11.019>
- [74] Denton AL, Hough AD, Freeman JA, Marsden JF. Effects of superficial heating and insulation on walking speed in people with hereditary and spontaneous spastic paraparesis: A randomized crossover study. *Ann Phys Rehabil Med* [Internet]. 2018;61(2):72-77. Available from: <https://doi.org/10.1016/j.rehab.2017.12.001>
- [75] Rinaldi M, Ranavolo A, Conforto S, Martino G, et al. Increased lower limb muscle coactivation reduces gait performance and increases metabolic cost in patients with hereditary spastic paraparesis. *Clin Biomech* [Internet]. 2017;48:63-72. Available from: <https://doi.org/10.1016/j.clinbiomech.2017.07.013>
- [76] Zhang Y, Roxburgh R, Huang L, Parsons J, et al. The effect of hydrotherapy treatment on gait characteristics of hereditary spastic paraparesis patients. *Gait Posture* [Internet]. 2014;39(4):1074-1079. Available from: <https://doi.org/10.1016/j.gaitpost.2014.01.010>
- [77] McDermott A, Bolger C, Keating L, McEvoy L, et al. Reliability of three-dimensional gait analysis in cervical spondylotic myelopathy. *Gait Posture* [Internet]. 2010;32(4):552-558. Available from: <https://doi.org/10.1016/j.gaitpost.2010.07.019>
- [78] Piccinini L, Cimolin V, D'Angelo MG, Crivellini M, et al. 3D gait analysis in patients with hereditary spastic paraparesis and spastic diplegia: A kinematic, kinetic and EMG comparison. *Eur J Paediatr Neurol* [Internet]. 2011;15(2):138-145. Available from: <https://doi.org/10.1016/j.ejpn.2010.07.009>
- [79] Ryu T, Choi HS, Choi H, Chung MK. A comparison of gait characteristics between Korean and Western people for establishing Korean gait reference data. *Int J Ind Ergon* [Internet]. 2006;36(12):1023-1030. Available from: <https://doi.org/10.1016/j.ergon.2006.09.013>

- [80] Jung Young C, Heri B, Ngimwhichi J, Stephanie S, et al. Effects of wearing shoes on the feet: Radiographic comparison of middle-aged partially shod Maasai women's feet and regularly shod Maasai and Korean women's feet. *J Foot Ankle Surg* [Internet]. 2018;24(4):330-335. Available from: <https://doi.org/10.1016/j.fas.2017.03.012>
- [81] Dalgas U, Langeskov-Christensen M, Skjærbaek A, Jensen E, et al. Is the impact of fatigue related to walking capacity and perceived ability in persons with multiple sclerosis? A multicenter study. *J Neurol Sci* [Internet]. 2018;387:179-186. Available from: <https://doi.org/10.1016/j.jns.2018.02.026>
- [82] Bethoux F, Varsanik JS, Chevalier TW, Halpern EF, et al. Walking speed measurement with an Ambient Measurement System (AMS) in patients with multiple sclerosis and walking impairment. *Gait Posture* [Internet]. 2018;61:393-397. Available from: <https://doi.org/10.1016/j.gaitpost.2018.01.033>
- [83] Kalron A, Aloni R. Contrasting relationship between depression, quantitative gait characteristics and self-report walking difficulties in people with multiple sclerosis. *Mult Scler Relat Disord* [Internet]. 2018;19:1-5. Available from: <https://doi.org/10.1016/j.msard.2017.10.012>
- [84] van den Berg MEL, Barr CJ, McLoughlin JV, Crotty M. Effect of walking on sand on gait kinematics in individuals with multiple sclerosis. *Mult Scler Relat Disord* [Internet]. 2017;16:15-21. Available from: <https://doi.org/10.1016/j.msard.2017.05.008>
- [85] Kalron A, Menascu S, Dolev M, Givon U. The walking speed reserve in low disabled people with multiple sclerosis: Does it provide greater insight in detecting mobility deficits and risk of falling than preferred and fast walking speeds? *Mult Scler Relat Disord* [Internet]. 2017;17:202-206. Available from: <https://doi.org/10.1016/j.msard.2017.08.010>
- [86] Pau M, Corona F, Pilloni G, Porta M, et al. Texting while walking differently alters gait patterns in people with multiple sclerosis and healthy individuals. *Mult Scler Relat Disord* [Internet]. 2018;19:129-133. Available from: <https://doi.org/10.1016/j.msard.2017.11.021>
- [87] Della Sala S, Spinnler H, Venneri A. Walking difficulties in patients with Alzheimer's disease might originate from gait apraxia. *J Neurol Neurosurg Psychiatry* [Internet]. 2004;75(2):196-201. Available from: <https://www.ncbi.nlm.nih.gov/pubmed/14742586>
- [88] Vieira Pereira F, Ferreira de Oliveira F, Rizek Schultz R, Ferreira Bertolucci PH. Balance impairment does not necessarily coexist with gait apraxia in mild and moderate Alzheimer's disease. *Arq Neuro-Psiquiatr* [Internet]. 2016;74(6):450-455. Available from: <https://doi.org/10.1590/0004-282x20160063>
- [89] Dale ML, Curtze C, Nutt JG. Apraxia of gait- or apraxia of postural transitions? *Parkinsonism Relat Disord* [Internet]. 2018;50:19-22. Available from: <https://doi.org/10.1016/j.parkreldis.2018.02.024>
- [90] Hong Jin J, Maeng Je C, Seong-Jin C, Seon-Uk K, et al. Quantitative analysis of ataxic gait in patients with schizophrenia: The influence of age and visual control. *Psychiatry Res* [Internet]. 2007;152(2-3):155-164. Available from: <https://doi.org/10.1016/j.psychres.2006.09.001>
- [91] Wen-Juh H. Reversible pseudoathetosis and sensory ataxic gait caused by cervical spondylotic myelopathy. *J Clin Neurosci* [Internet]. 2016;34:271-272. Available from: <https://doi.org/10.1016/j.jocn.2016.08.004>
- [92] Siasios ID, Spanos SL, Kanellopoulos AK, Fotiadou A, et al. The Role of Gait Analysis in the Evaluation of Patients with Cervical Myelopathy: A Literature Review Study. *World Neurosurg* [Internet]. 2017;101:275-282. Available from: <https://doi.org/10.1016/j.wneu.2017.01.122>
- [93] Miura M, Miyai I, Hatakenaka M, Kubota K, et al. Sustained prefrontal activation during ataxic gait: A compensatory mechanism for ataxic stroke? *Neuroimage* [Internet]. 2007;37(4):1338-1345. Available from: <https://doi.org/10.1016/j.neuroimage.2007.06.014>
- [94] Schmitz-Hübsch T, Brandt AU, Pfueler C, Zange L, et al. Accuracy and repeatability of two methods of gait analysis - GaitRiteTM und Mobility LabTM - in subjects with cerebellar ataxia. *Gait Posture* [Internet]. 2016;48:194-201. Available from: <https://doi.org/10.1016/j.gaitpost.2016.05.014>
- [95] Buckley E, Mazzà C, McNeill A. A systematic review of the gait characteristics associated with Cerebellar Ataxia. *Gait Posture* [Internet]. 2018;60:154-163. Available from: <https://doi.org/10.1016/j.gaitpost.2017.11.024>
- [96] Caliandro P, Iacovelli C, Conte C, Simbolotti C, et al. Trunk-lower limb coordination pattern during gait in patients with ataxia. *Gait Posture* [Internet]. 2017;57:252-257. Available from: <https://doi.org/10.1016/j.gaitpost.2017.06.267>
- [97] Pearson-Dennett V, Todd G, Wilcox RA, Vogel AP, et al. History of cannabis use is associated with altered gait. *Drug Alcohol Depend* [Internet]. 2017;178:215-222. Available from: <https://doi.org/10.1016/j.drugalcdep.2017.05.017>
- [98] Lambert CS, Philpot RM, Engberg ME, Johns BE, et al. Gait analysis and the cumulative gait index (CGI): Translational tools to assess impairments exhibited by rats with olivocerebellar ataxia. *Behav Brain Res* [Internet]. 2014;274:334-343. Available from: <https://doi.org/10.1016/j.bbr.2014.08.004>
- [99] Schniepp R, Wuehr M, Schlick C, Huth S, et al. Increased gait variability is associated with the history of falls in patients with cerebellar ataxia. *J Neurol* [Internet]. 2014;261:213-223. Available from: <https://doi.org/10.1007/s00415-013-7189-3>
- [100] Wuehr M, Nusser E, Krafczyk S, Straube A, et al. Noise-Enhanced Vestibular Input Improves Dynamic Walking Stability in Healthy Subjects. *Brain Stimul* [Internet]. 2016;9(1):109-116. Available from: <https://doi.org/10.1016/j.brs.2015.08.017>
- [101] Iwasaki S, Fujimoto C, Egami N, Kinoshita M, et al. Noisy vestibular stimulation increases gait speed in normal and in bilateral vestibulopathy. *Brain Stimul* [Internet]. 2018;11(4):709-715. Available from: <https://doi.org/10.1016/j.brs.2018.03.005>
- [102] Yin M, Ishikawa K, Omi E, Saito T, et al. Small vestibular schwannomas can cause gait instability. *Gait Posture* [Internet]. 2011;34(1):25-28. Available from: <https://doi.org/10.1016/j.gaitpost.2011.02.026>
- [103] Lang J, Ishikawa K, Hatakeyama K, Wong WH, et al. 3D body segment oscillation and gait analysis for vestibular disorders. *Auris Nasus Larynx* [Internet]. 2013;40(1):18-24. Available from: <https://doi.org/10.1016/j.anl.2011.11.007>

- [104] Henriksson M, Henriksson J, Bergenius J. Gait initiation characteristics in elderly patients with unilateral vestibular Impairment. *Gait Posture* [Internet]. 2011;33(4):661-667. Available from: <https://doi.org/10.1016/j.gaitpost.2011.02.018>
- [105] Angunseri N, Ishikawa K, Yin M, Omi E, et al. Gait instability caused by vestibular disorders –Analysis by tactile sensor. *Auris Nasus Larynx* [Internet]. 2011;38(4):462-468. Available from: <https://doi.org/10.1016/j.anl.2011.01.016>
- [106] de Souza Melo R. Gait performance of children and adolescents with sensorineural hearing loss. *Gait Posture* [Internet]. 2017;57:109-114. Available from: <https://doi.org/10.1016/j.gaitpost.2017.05.031>
- [107] Hösl M, Böhm H, Eck J, Döderlein L. Positive effects of backward downhill treadmill training on spastic equinus gait. *Gait Posture* [Internet]. 2015; 42S: S85-S86. Available from: <https://doi.org/10.1016/j.gaitpost.2015.06.156>
- [108] Houx L, Lempereur M, Rémy-Nériss O, Brochard S. Threshold of equinus which alters biomechanical gait parameters in children. *Gait Posture* [Internet]. 2013;38(4):582-589. Available from: <https://doi.org/10.1016/j.gaitpost.2013.01.026>
- [109] Gatt A, De Giorgio S, Chockalingam N, Formosa C. A pilot investigation into the relationship between static diagnosis of ankle equinus and dynamic ankle and foot dorsiflexion during stance phase of gait: Time to revisit theory? *The Foot* [Internet]. 2017;30:47-52. Available from: <https://doi.org/10.1016/j.foot.2017.01.002>
- [110] Houx L, Lempereur M, Rémy-Nériss O, Gross R, et al. Changes in muscle activity in typically developing children walking with unilaterally induced equinus. *Clin Biomech* [Internet]. 2014;29(10):1116-1124. Available from: <https://doi.org/10.1016/j.clinbiomech.2014.09.015>
- [111] Higginson JS, Zajac FE, Neptune RR, Kautz SA, et al. Effect of equinus foot placement and intrinsic muscle response on knee extension during stance. *Gait Posture* [Internet]. 2006;23(1):32-36. Available from: <https://doi.org/10.1016/j.gaitpost.2004.11.011>
- [112] Kläusler M, Speth BM, Brunner R, Tirosh O, et al. Long-term follow-up after tibialis anterior tendon shortening in combination with Achilles tendon lengthening in spastic equinus in cerebral palsy. *Gait Posture* [Internet]. 2017;58:457-462. Available from: <https://doi.org/10.1016/j.gaitpost.2017.08.028>
- [113] Allet L, Armand S, Aminian K, Pataky Z, et al. An exercise intervention to improve diabetic patients' gait in a real-life Environment. *Gait Posture* [Internet]. 2010;32(2):185-190. Available from: <https://doi.org/10.1016/j.gaitpost.2010.04.013>
- [114] Camargo MR, Barela JA, Nozabieli AJL, Mantovani AM, et al. Balance and ankle muscle strength predict spatiotemporal gait parameters in individuals with diabetic peripheral neuropathy. *Diabetes Metab Syndr* [Internet]. 2015;9(2):79-84. Available from: <https://doi.org/10.1016/j.dsx.2015.02.004>
- [115] Fernando M, Crowther R, Lazzarini P, Sangla K, et al. Biomechanical characteristics of peripheral diabetic neuropathy: A systematic review and meta-analysis of findings from the gait cycle, muscle activity and dynamic barefoot plantar pressure. *Clin Biomech* [Internet]. 2013;28(8):831-845. Available from: <https://doi.org/10.1016/j.clinbiomech.2013.08.004>
- [116] Sawacha Z, Gabriella G, Cristoferi G, Guiotto A, et al. Diabetic gait and posture abnormalities: A biomechanical investigation through three dimensional gait analysis. *Clin Biomech* [Internet]. 2009;24(9):722-728. Available from: <https://doi.org/10.1016/j.clinbiomech.2009.07.007>
- [117] Khalaf K, Al-Angari HM, Khandoher AH, Lee S, et al. Gait alterations in the UAE population with and without diabetic complications using both traditional and entropy measures. *Gait Posture* [Internet]. 2017;58:72-77. Available from: <https://doi.org/10.1016/j.gaitpost.2017.07.109>
- [118] Allet L, Armand S, de Bie RA, Golay A, et al. Reliability of diabetic patients' gait parameters in a challenging environment. *Gait Posture* [Internet]. 2008;28(4):680-686. Available from: <https://doi.org/10.1016/j.gaitpost.2008.05.006>
- [119] Jin-Hyuck P. The effects of plantar perception training on balance and falls efficacy of the elderly with a history of falls: A single-blind, randomized controlled trial. *Arch Gerontol Geriatr* [Internet]. 2018;77:19-23. Available from: <https://doi.org/10.1016/j.archger.2018.03.014>
- [120] Herman T, Giladi N, Gurevich T, Hausdorff JM. Gait instability and fractal dynamics of older adults with a “cautious” gait: why do certain older adults walk fearfully? *Gait Posture* [Internet]. 2005;21(2):178-185. Available from: <https://doi.org/10.1016/j.gaitpost.2004.01.014>
- [121] Tsai Y-J, Lin S-I. Older adults adopted more cautious gait patterns when walking in socks than barefoot. *Gait Posture* [Internet]. 2013;37(1):88-92. Available from: <https://doi.org/10.1016/j.gaitpost.2012.06.034>
- [122] Liang C-K, Chou M-Y, Peng L-N, Liao M-C, et al. Gait speed and risk assessment for falls among men aged 80 years and older: A prospective cohort study in Taiwan. *Eur Geriatr Med* [Internet]. 2014;5(5):298-302. Available from: <https://doi.org/10.1016/j.eurger.2014.06.034>
- [123] Balasubramanian CK, Clark DJ, Gouelle A. Validity of the Gait Variability Index in older adults: Effect of aging and mobility impairments. *Gait Posture* [Internet]. 2015;41(4):941-946. Available from: <https://doi.org/10.1016/j.gaitpost.2015.03.349>
- [124] Spaulding SJ, Patla AE, Flanagan J, Elliott DB, et al. Waterloo Vision and Mobility Study: Normal gait characteristics during dark and light adaptation in individuals with age-related maculopathy. *Gait Posture* [Internet]. 1995;3(4):227-235. Available from: [https://doi.org/10.1016/0966-6362\(96\)82852-9](https://doi.org/10.1016/0966-6362(96)82852-9)
- [125] Fan Y, Li Z, Han S, Lv C, et al. The influence of gait speed on the stability of walking among the elderly. *Gait Posture* [Internet]. 2016;47:31-36. Available from: <https://doi.org/10.1016/j.gaitpost.2016.02.018>
- [126] Cruz-Jimenez M. Normal Changes in Gait and Mobility Problems in the Elderly. *Phys Med Rehabil Clin N Am* [Internet]. 2017;28(4):713-725. Available from: <https://doi.org/10.1016/j.pmr.2017.06.005>
- [127] Auvinet B, Touzard C, Goëb V. Gait instability out-patients consultation in the elderly: Interests of simple and dual task gait analysis. *Ann Phys Rehabil Med* [Internet]. 2015;58:e155. Available from: <https://doi.org/10.1016/j.rehab.2015.07.368>

- [128] Hirose D, Ishida K, Nagano Y, Takashi T, et al. Posture of the trunk in the sagittal plane is associated with gait in community-dwelling elderly population. *Clin Biomechs* [Internet]. 2004;19(1):57-63. Available from: <https://doi.org/10.1016/j.clinbiomech.2003.08.005>
- [129] Leigh RJ, Osis ST, Ferber R. Kinematic gait patterns and their relationship to pain in mild-to-moderate hip osteoarthritis. *Clin Biomechs* [Internet]. 2016;34:12-17. Available from: <https://doi.org/10.1016/j.clinbiomech.2015.12.010>
- [130] Smith JA, Gordon J, Kulig K. The influence of divided attention on walking turns: Effects on gait control in young adults with and without a history of low back pain. *Gait Posture* [Internet]. 2017;58:498-503. Available from: <https://doi.org/10.1016/j.gaitpost.2017.09.019>
- [131] O'Connell M, Farrokhi S, Fitzgerald GK. The role of knee joint moments and knee impairments on self-reported knee pain during gait in patients with knee osteoarthritis. *Clin Biomechs* [Internet]. 2016;31:40-46. Available from: <https://doi.org/10.1016/j.clinbiomech.2015.10.003>
- [132] Sawa R, Doi T, Misu S, Saito T, et al. The severity and number of musculoskeletal pain associated with gait in community-dwelling elderly individuals. *Gait Posture* [Internet]. 2017;54:242-247. Available from: <https://doi.org/10.1016/j.gaitpost.2017.03.013>
- [133] Chen G, Nie Y, Xie J, Cao G, et al. Gait Analysis of Leg Length Discrepancy—Differentiated Hip Replacement Patients With Developmental Dysplasia: A Midterm Follow-Up. *J Arthroplast* [Internet]. 2018;33(5):1437-1441. Available from: <https://doi.org/10.1016/j.arth.2017.12.013>
- [134] Beresford MW, Cleary AG. Evaluation of a limping child. *Curr Paediatr* [Internet]. 2005;15(1):15-22. Available from: <https://doi.org/10.1016/j.cupe.2004.10.004>
- [135] Khamis S, Carmeli E. Relationship and significance of gait deviations associated with limb length discrepancy: A systematic review. *Gait Posture* [Internet]. 2017;57:115-123. Available from: <https://doi.org/10.1016/j.gaitpost.2017.05.028>
- [136] Khamis S, Carmeli E. The effect of simulated leg length discrepancy on lower limb biomechanics during gait. *Gait Posture* [Internet]. 2018;61:73-80. Available from: <https://doi.org/10.1016/j.gaitpost.2017.12.024>
- [137] Chopra S, Crevoisier X. Preoperative gait asymmetry in end-stage unilateral ankle osteoarthritis patients. *Foot Ankle Surg* [Internet]. 2019;25(3):298-302. Available from: <https://doi.org/10.1016/j.fas.2017.12.004>
- [138] Vasudevan PN, Vaidyalingam KV, Nair PB. Can trendelenburg's sign be positive if the hip is normal? *J Bone Joint Surg [Br]* [Internet]. 1997;79-B(3):462-466. Available from: <https://doi.org/10.1302/0301-620X.79B3.0790462>
- [139] Physiopedia USA, Trendelenburg Gait [Internet]. 2021; Available from: https://www.physio-pedia.com/Trendelenburg_Gait
- [140] Pai VS. Significance of the Trendelenburg test in total hip arthroplasty influence of lateral approaches. *J Arthroplast* [Internet]. 1996;11(2):174-179. Available from: [https://doi.org/10.1016/S0883-5403\(05\)80013-0](https://doi.org/10.1016/S0883-5403(05)80013-0)
- [141] Petrofsky JS. The use of electromyogram biofeedback to reduce Trendelenburg gait. *Eur J Appl Physiol* [Internet]. 2001;85(5):491-495. Available from: <https://doi.org/10.1007/s004210100466>
- [142] Gilliss AC, Swanson RL, Janora D, Venkataraman V. Use of Osteopathic Manipulative Treatment to Manage Compensated Trendelenburg Gait Caused by Sacroiliac Somatic Dysfunction. *JOM* [Internet]. 2010;110(3):81-86. Available from: <https://doi.org/10.7556/joa.2010.110.2.81>
- [143] Koutakis P, Johanning JM, Haynatzki G, Myers SA, et al. Abnormal joint powers before and after the onset of claudication symptoms. *J Vasc Surg* [Internet]. 2010;52(2):340-347. Available from: <https://doi.org/10.1016/j.jvs.2010.03.005>
- [144] Zijlstra W. Assessment of spatio-temporal parameters during unconstrained walking. *Eur J Appl Physiol* [Internet]. 2004;92:39-44. Available from: <https://doi.org/10.1007/s00421-004-1041-5>
- [145] Öberg T, Karsznia A, Öberg K. Basic gait parameters: Reference data for normal subjects, 10-79 years of age. *J Rehabil Res Dev* [Internet]. 1993;30(2):210-223. Available from: <https://www.rehab.research.va.gov/jour/93/30/2/pdf/oberg.pdf>
- [146] Chung M-J, Wang M-J J. The change of gait parameters during walking at different percentage of preferred walking speed for healthy adults aged 20-60 years. *Gait Posture* [Internet]. 2010;31(1):131-135. Available from: <https://doi.org/10.1016/j.gaitpost.2009.09.013>
- [147] Stolze H, Kuhtz-Buschbeck JP, Mondwurf C, Jöhnk K, et al. Retest reliability of spatiotemporal gait parameters in children and adults. *Gait Posture* [Internet]. 1998;7(2):125-130. Available from: [https://doi.org/10.1016/S0966-6362\(97\)00043-X](https://doi.org/10.1016/S0966-6362(97)00043-X)
- [148] Kirtley C. Clinical Gait Analysis: Theory and Practice. China: Elsevier, Churchill Livingstone; 2006. 316p.
- [149] Erhart-Hledik JC, Favre J, Andriacchi TP. New insight in the relationship between regional patterns of knee cartilage thickness, osteoarthritis disease severity, and gait mechanics. *J Biomech* [Internet]. 2015;48(14):3868-3875. Available from: <https://doi.org/10.1016/j.biomech.2015.09.033>

dx.doi.org/10.17488/RMIB.42.3.2

E-LOCATION ID: 1188

Image-based Glaucoma Classification Using Fundus Images and Deep Learning

Clasificación de Glaucoma Basada en Imágenes de Fondo de Ojo y Aprendizaje Profundo

H. J. Sandoval-Cuellar¹, G. Alfonso-Francia¹, M. A. Vázquez-Membrillo², J. M. Ramos-Arreguín¹, S. Tovar-Arriaga¹

¹Universidad Autónoma de Querétaro

²Instituto Mexicano de Oftalmología, IAP

ABSTRACT

Glaucoma is an eye disease that gradually affects the optic nerve. Intravascular high pressure can be controlled to prevent total vision loss, but early glaucoma detection is crucial. The optic disc has been a notable landmark for finding abnormalities in the retina. The rapid development of computer vision techniques has made it possible to analyze eye conditions from images enabling to help a specialist to make a diagnosis using a technique that is non-invasive in its initial stage through fundus images. We propose a methodology glaucoma detection using deep learning. A convolutional neural network (CNN) is trained to extract multiple features, to classify fundus images. The accuracy, sensitivity, and the area under the curve obtained using the ORIGA database are 93.22%, 94.14%, and 93.98%. The use of the algorithm for the automatic region of interest detection in conjunction with our CNN structure considerably increases the glaucoma detecting accuracy in the ORIGA database.

KEYWORDS: Deep Learning, Glaucoma diagnosis, Image-based classification, Convolutional Neural Network

RESUMEN

El glaucoma es una enfermedad que afecta gradualmente al nervio óptico. La presión intravascular se puede controlar para prevenir la pérdida de visión, por lo que la detección temprana del glaucoma es crucial. El disco óptico ha sido un punto de referencia importante para encontrar anomalías en la retina. El rápido desarrollo de técnicas de visión por computadora ha hecho posible el analizar las condiciones del ojo ayudando al especialista a realizar un diagnóstico utilizando una técnica no invasiva en su estadio inicial en imágenes de fondo de ojo. En este artículo, se propone una arquitectura para la detección de glaucoma utilizando aprendizaje profundo. Una red neuronal convolucional (RNC) es entrenada para extraer múltiples características, para clasificar imágenes de fondo de ojo. La exactitud, sensibilidad, y el área bajo la curva obtenidos en la base de datos ORIGA son 93.22%, 94.14% y 93.98%. El uso del algoritmo para la detección automática de la región de interés, incrementa considerablemente la exactitud de detección de glaucoma en la base de datos ORIGA.

PALABRAS CLAVE: Aprendizaje profundo, Diagnóstico del glaucoma, Clasificación de imágenes, Red neuronal convolucional

Corresponding author

TO: Saúl Tovar Arriaga

INSTITUTION: Universidad Autónoma de Querétaro

ADDRESS: Cerro de las Campanas S/N,

Cto. Universitario, C. P. 76110, Las Campanas,

Santiago de Querétaro, México

E-MAIL: saul.tovar@uaq.mx

Received:

8 June 2021

Accepted:

11 September 2021

INTRODUCTION

The World Health Organization (WHO) states that glaucoma is the second leading cause of blindness in the world, only after cataracts [1]. Since there is no cure for glaucoma [2], it is necessary to diagnose this disease early to delay its development [3].

Glaucoma is characterized by optic nerve damage due to increased degeneration of nerve fibers [4]. Since symptoms appear until the disease is severe, glaucoma is called a silent thief of sight [5]. Typically, aqueous humor drains out of the eye through the trabecular meshwork, but when the passage is obstructed, aqueous humor accumulates. The increase in this fluid will cause pressure to grow and cause ganglion cell damage [6]. However, it was found that the pressure measurement was not specific or sensitive enough to be the only useful indicator for detecting glaucoma because visual impairment would occur without increasing pressure. Therefore, a comprehensive examination should also include the use of images and visual field tests to analyze the retina [7].

Fundus imaging is the process of obtaining a two-dimensional projection of the retinal tissue employing reflected light. Finally, the resulting 2D image contains the image intensity that indicates the reflected light amount. Color fundus imaging is used to detect disease, where the image has R, G, and B bands, and their intensity changes highlight different parts of the retina [8].

Due to their non-invasiveness, fundoscopy and optical coherence tomography (OCT) has become the imaging methods of choice for the detection and evaluation of glaucoma [9]. Nevertheless, due to its cost, OCT is not readily available.

There are different types of glaucoma, such as open-angle, closed-angle, secondary, normal-tension, pigmentary, and congenital glaucoma [10]. Some types require surgical treatment [11]. The optic disc and cup,

peripapillary atrophy, and retinal nerve fiber layer [12] are four structures that are considered essential for detecting glaucoma. Family history has also been shown to be genetically related to the onset of the disease [13].

In most cases, treatment in the early stage of the disease can prevent total vision loss in glaucoma patients [14], so a system that can help ophthalmologists make a diagnosis could increase the chances of saving people's vision. However, designing a system that provides reliable tests for glaucoma diagnosis is a complicated and stimulating task in clinical practice [15].

Figure 1 shows an image of the fundus in a healthy condition where the most important parts can be seen, such as the optic nerve, which is where the study of this work will be focused. The outer part of the optic nerve is called the optic disk (OD), and the smaller blurry inner circle is called the optic cup (OC). In the OD area, we can see the main arteries and veins, whereas the veins have a darker color than the arteries. Veins usually are larger in caliber than arteries, having an average AVR ratio of 2:3 [17].

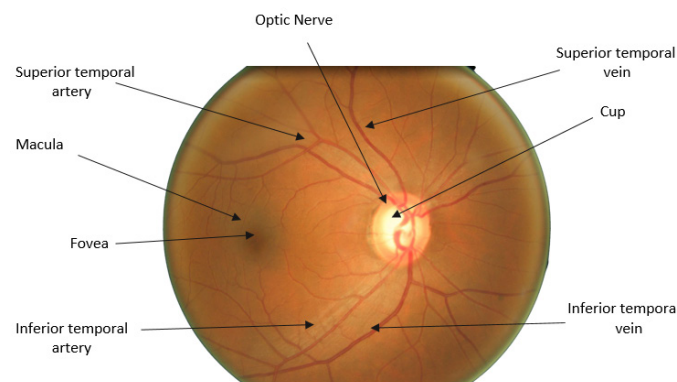


FIGURE 1. Image of the optic nerve [16].

The region of interest (ROI) usually is less than 11% of the retina's fundus image's total size. By decreasing the size of the image with the ROI's detection, a reduction in the computational resources used is possible

^[18]. Both optic disc and cup segmentation are essential components of optic nerve segmentation and, together, form the basis of a glaucoma evaluation. In ^[19], a reference data set for evaluating the cup segmentation method was published. Nevertheless, it does not provide free access to the general public.

There are relatively few public data sets for glaucoma evaluation compared to available data sets for diabetic retinopathy ^[20] and vascular segmentation ^[21]. The ORIGA database contains 650 retinal images labeled by retina specialists from the Singapore Eye Research Institute. An extensive collection of image signs usually taken into account for the diagnosis of glaucoma are annotated. In the Drishti-GS dataset ^[22], all images were collected from the Madurai Aravind Eye Hospital of the hospital visitors with their consent. The selection of glaucoma patients is made based on the clinical findings during the study. The selected subjects are between 40 and 80 years old, and the number of males and females is roughly equal. Patients who choose to undergo routine optometry and who are not glaucoma represent the normal category.

Usually, the fundus image analysis with artificial intelligence is carried out from two approaches, 1) the classification at the image level and 2) the classification at the pixel level. In image-level classification, the learning model is trained with images previously classified by an expert, in this case, a retina specialist. This classification generally contains the disease progression ^[23]. For example, the severity of DR is classified into five grades, and each of these grades is associated with a number. The learning model begins to associate the patterns in the image to their labels. The second approach is the anatomical and lesion segmentation, such as separating the blood vessels from the rest of the retina in order to measure their caliber. For example, in the case of Hypertensive Retinopathy, the vein/artery relationship plays an essential role in the diagnosis of the disease ^[24].

There are several works carried out for the detection of glaucoma. Both images based and pixel-based classification have been used. We will follow an image-based classification approach in this research.

A six-layer CNN architecture was proposed by Chen *et al.* ^[5], where four layers are convolutional, and the final two are fully connected. ORIGA and SCES are used in this study. From the ORIGA database, 99 images were randomly selected for training and the remaining 551 images for the testing, obtaining results of 0.831 for AUC. In a second experiment, 650 images from the ORIGA database are used for training, and 1676 images from the SCES database for the testing, the area under the curve obtained is 0.887.

Acharya *et al.* ^[6] proposed to use a Support Vector Machine for classification and the Gabor transform that will notice the subtle changes in the image's background. The database used was a private database of Kasturba Medical College, Manipal, India, with 510 images. 90% of the images were used for training, while the remaining 10% for testing. The results obtained were 93.10% accuracy, 89.75% sensitivity, and a specificity of 96.20%.

Raghavendra *et al.* ^[1] proposes to perform the automatic recognition of glaucoma utilizing a convolutional neural network of 18 layers. This work consists of a standard CNN, with convolution layers and max-pooling, and a fully connected layer where classification is performed. Initially, 70% of the randomly selected samples are used for training and 30% for testing. 589 healthy images and 837 with glaucoma of a private database were deployed. The process was repeated fifty times with random training and test partitions. The results obtained were 98.13% accuracy, 98% sensitivity, and 98.3% specificity.

Gour *et al.* ^[8] proposes an automatic glaucoma detection system using Support Vector Machine (SVM) for classification. Combine GIST and PHOG to extract features in images. This technique eliminates the need for

image segmentation. Instead, it works with a diagnostic system that makes use of characteristics such as texture and shape to detect the disease. This technique yielded an accuracy of 83.4% using the Drishti-GS1 and High-Resolution Fundus (HRF) databases.

Gheisari *et al.*^[25] implement two architectures, the VGG16 and ResNet, concatenating LSTM blocks. To determine the best one, they carry out several experiments varying the number of epochs and learning rate. The best results are achieved with the VGG16 network, achieving 95% sensitivity and 96% specificity.

Gómez-Valverde *et al.*^[26] use architectures such as VGG19, ResNet, GoogleNet and Denet Disc. The best results obtained were obtained using VGG19 with transfer learning, obtaining 94.20 of AUC, 87.01 of sensitivity, and 89.01 of specificity.

Pinto *et al.*^[27] use 5 databases adding a total of 1707 images. They carry out the experimentation with each of the databases separately, but the best results were obtained by putting together all the available images. They achieve an AUC of 96.05, a specificity of 85.8 and a sensitivity of 93.46 using Xception architecture.

We propose an image-based classification approach using a deep neural network for glaucoma diagnosis in fundus images in the present work. A preprocessing step will be carried out where the region of interest will be extracted, specifically the region where the optic disc is located. Once that region is obtained, a neural network is fed with the cropped images in order to classify if the image has or not glaucoma.

MATERIALS AND METHODS

Preprocessing

This section introduces a method to locate the retina optic disc, which contains the necessary features to diagnose glaucoma. These image areas will be the input to the neural network proposed in this work. Since the images' size is 3072 x 2048 pixels, it is reduced to four times its original size, leaving the images' dimensions in 768 x 512. The input images are converted to grayscale. Therefore, it is reasonable to obtain a higher contrast of the optic disc than the original image. For this, the red and green channels are used, which are the ones that have the most significant impact on the optic disc. To do this, Equation 1 is applied.

$$Img_{gray} = R * 0.9 + G * 0.5 \quad (1)$$

Where Img_{gray} is the grayscale image, and R and G are the corresponding red and green channels. To determine which channels would be used, the histograms per channel of the image were obtained, in which it is determined which of them have the greatest impact on the contrast of the image. Conventional grayscale conversion is obtained using the luminance coefficients in ITU-R BT. 601-7, which is a recommendation that specifies digital video signal encoding methods^[28].

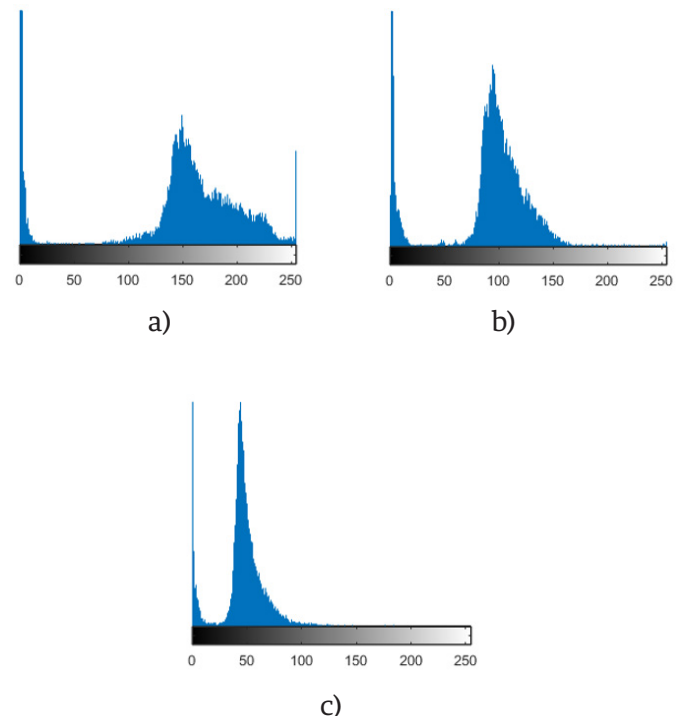


FIGURE 2. The histogram of the red channel is shown in a), the green channel in b), and the blue channel in c).

The coefficients and channels used in our method were obtained by analyzing the histograms in each channel of the images. These histograms are shown in Figure 2.

The results obtained after the transformation are shown in Figure 3.

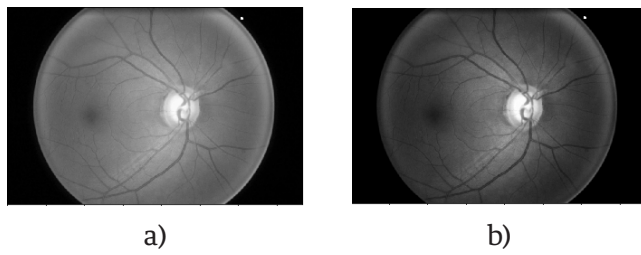


FIGURE 3. The conventional transformation to grayscale is represented by a), and the one proposed by b).

The next step is to scroll a kernel through the image to divide it into different sub-images to determine where the optic disc is located as shown in Figure 4. The optic disc is the most brilliant part of the retina. Excess brightness can be eliminated in parts where the optic disc is not located.

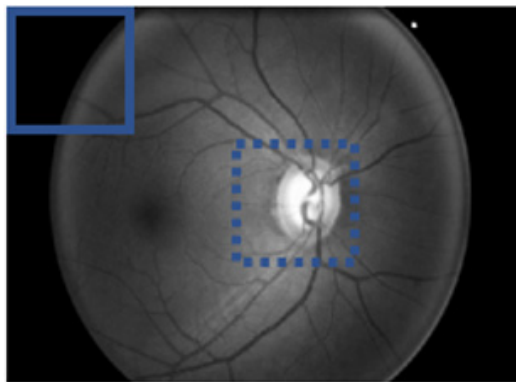


FIGURE 4. Kernel scrolling through original image.

Because the optical disk represents approximately 10% of the original image, the scrolling box's size, or kernel, was chosen to ensure that any sub-images would be selected. The selected size was 192 x 192 pixels, four times smaller than the image width after size reduction.

Equation 2 is applied to calculate the sub-images, depending on the size of the scrolling box and the step used

$$ubImg(x, y) = Img(x + x_0, y + y_0), \quad \forall (x, y) \in R \quad (2)$$

Where *SubImg* is the image inside the kernel, *Img* is the image after resizing, *x* is the kernel's horizontal starting point, *y* the vertical starting point, *x₀* the horizontal endpoint, that is, *x* + 192 and *y₀* the vertical endpoint, that is, *y* + 192.

To reduce the processing time, the kernel step will be 165 pixels in the horizontal direction and 150 in the vertical direction. With this step, we guarantee that the optical disc is in one of the sub-images at least once. Each time a new sub-image is selected, the average of all the pixels is calculated by applying Equation 3. This average is stored, and once all the sub-images have been analyzed, it is located where the highest average is. In this way, the sub-image where the optic disk is predicted is chosen.

$$promPix = \frac{\sum_{i=1}^n p_i}{n} \quad (3)$$

Where *promPix* is the average of the pixel values, *p_i* is the current pixel value, and *n* is the total number of pixels. With this new sub-image selected, the pixels' average value is taken, but now of each column and row.



FIGURE 5. A red dot represents the center of the image to be cropped.

This average will give us x and y coordinates. These coordinates represent the new image center that will be cropped to obtain the ROI. An example of this can be found in Figure 5.

The result after cropping an image can be found in Figure 6.

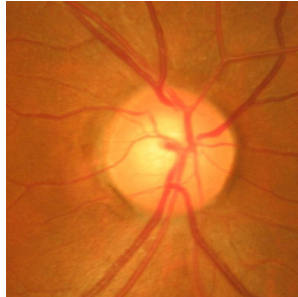


FIGURE 6. Result after cropping the image and obtaining the region of interest.

The entire process explained above for the ROI detection is shown in the pseudo-code in Algorithm 1.

Algorithm: Region of interest

```

Input: number of images Images
Output: Region of interest ROI
1: while Images is not empty
2:   Images  $\leftarrow$  Images/4
3:   Images  $\leftarrow$  (RedChannel * 0.9) + (GreenChannel * 0.5)
4:   kernel = 192x192
5:   if kernel  $\in$  Images then
6:     average = averageKernel
7:     if average > previousAverage
8:       previousAverage  $\rightarrow$  average
9:       Images  $\rightarrow$  kernel
10:    end
11:   end
12:   valMax = where (valMaxPix = Images)
13:   x = mean(posValMaxX)
14:   y = mean(posValMaxY)
15:   ROI = center(x, y)
16: end

```

The preprocessing described in Algorithm 1 is applied to the 650 images of the ORIGA database [16] to obtain the ROI. With the region of interest located, we pro-

ceed to perform normalization to the images. What is sought is that the values are within a smaller range, since the CNN's do not perform well when the input numerical attributes have a very large range. The normalization used (Equation 4) was the min-max [23].

$$valNorm = \frac{val - min_{img}}{max_{img} - min_{img}} \quad (4)$$

Where *valNorm* is the normalized value, *val* is the current value, *min_{img}* and *max_{img}* are the minimum and maximum image values. The values before normalization range from 0 to 255. After normalization, they will be in a range from 0 to 1.

Architecture

The images fed to the network have a size of 128 x 128 pixels. Convolution layers, ReLU, max-pooling, and fully connected layers comprise the proposed neural network. The output of each layer is the input of another, thus allowing the extraction of features. Since it is sought to differentiate between small and local image characteristics, which may differentiate a person's distinctive features with glaucoma, small 3x3 and 5x5 filters are used in the network. The final two layers will unite these characteristics to make a classification.

The order of the layers; convolution, ReLu and max-pooling is used in several well-known architectures, such as VGG16 [29]. The idea of using two fully connected layers came from the AlexNet [30] network, which uses 3 fully connected layers. Based on these two articles, an architecture is proposed.

As activation function at the output of the network, the sigmoidal function was used. This function was chosen because we are interested in a binary classification, so it will give us a probability of which class it can belong to. This activation function should not be confused with the one used between each convolutional layer. ReLU is used to add non-linearity to the

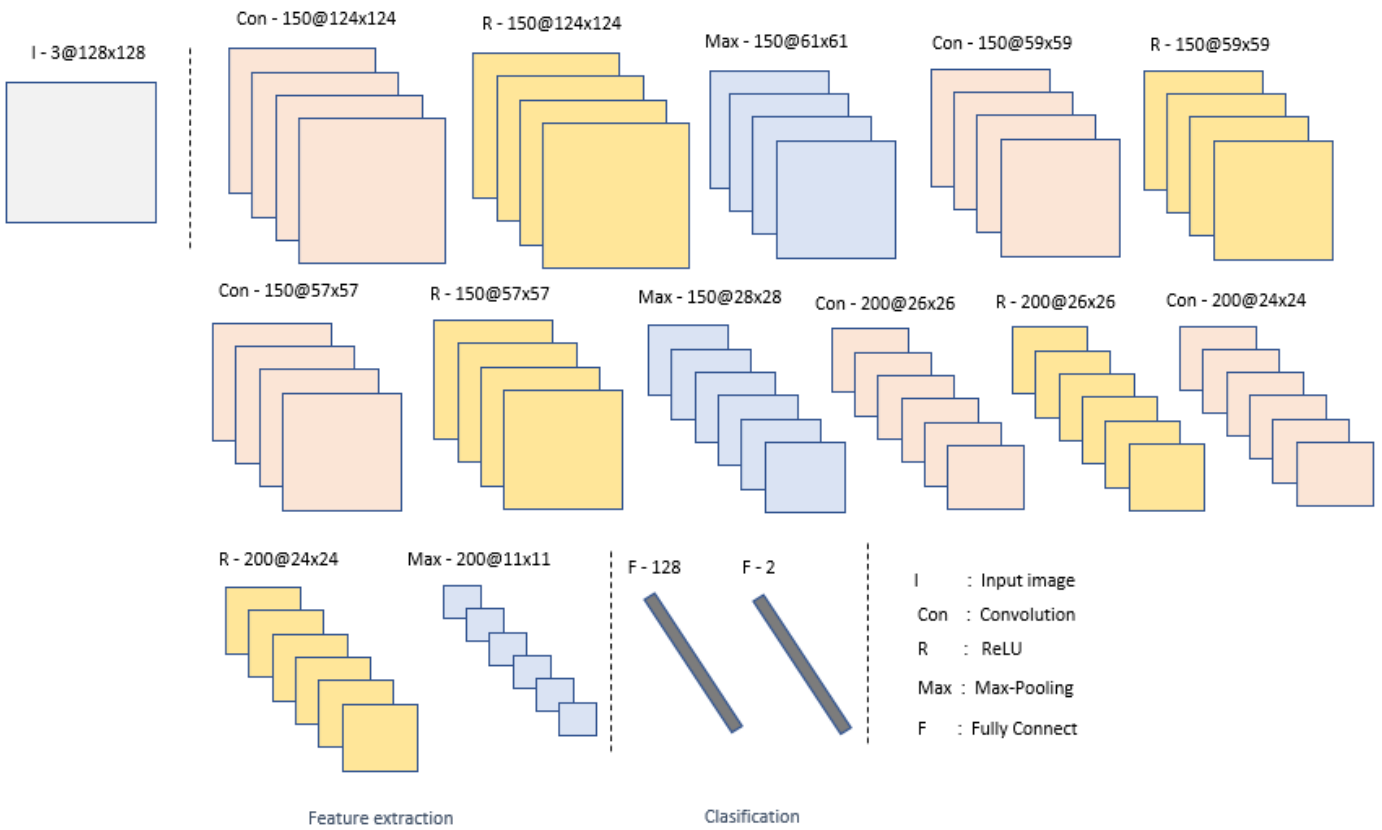


FIGURE 7. Overview of the proposed convolutional neural network architecture.

network and sigmoidal is used to regularize the output. The first fully connected layer has 128 neurons and the second has 2 neurons for classification.

As a loss function, we use Binary Cross Entropy. This was chosen due to the fact that binary classification is sought. This function will give us the prediction error, which will indicate to the network how correct its classification, which will help the network to improve as they pass the epochs. To avoid overfitting, dropout was used, which randomly turns off neurons in each training period, in order to distribute the power of selection of characteristics to all neurons equally, in this way, the model to learn independent characteristics. Adam was used as an optimizer, which combines the advantages of some others, such as the Momentum, maintaining the exponential moving average of the gradients, and the RMSprop, which maintains the exponential moving average, but of squared gradients.

The proposed neural network consists of fifteen layers. This number of layers was determined by experimentation. We have to take into account that with a shallower network, the extraction of features could be poor and therefore increase the difficulty to identify the desired features. However, with a deeper architecture, there is a risk of overfitting.

Convolutional layers represent high-level data features, and combining with a fully connected layer is one way to learn non-linear combinations of those features. In the network, two completely connected layers are used, seeking more significant learning of these combinations. To choose the best learning rate, we carried out tests with different values, and the one that had a better relationship between learning rate and performance is the selected one. The two images where the optic disc was not correctly detected are shown in Figure 8.

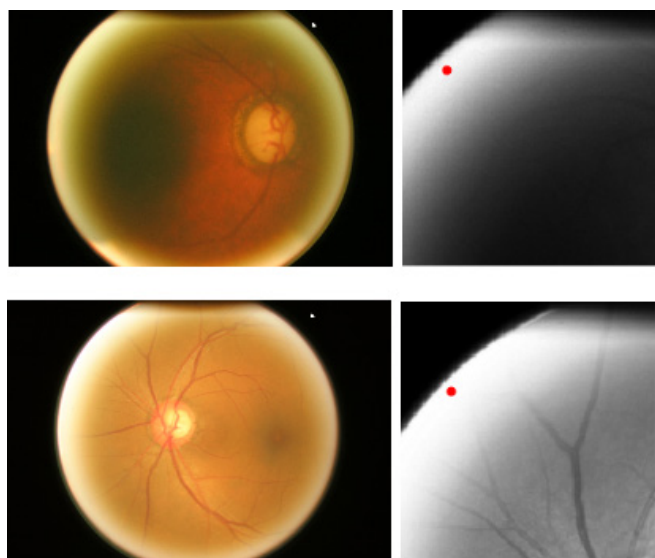


FIGURE 8. Unidentified optic disc.

In images that were not appropriately cropped, excess brightness may be noticed on the circumference of the fundus image. For this reason, the algorithm places the optic disc in that position and does not cut the image correctly. Of the 650 used images, 482 are from healthy patients and 168 from glaucoma patients.

Training and testing

455 images were used for training and 195 for validation, that is, 70% for training and 30% for validation. The images were chosen at random. The algorithm was developed in Python and ran on a computer with an Intel Core i7-3160QM 2.3 GHz CPU and 8 GB of RAM. The training execution time was 18.5 hours. Python 3 and TensorFlow were used. To implement the algorithm, it was necessary to use the Keras, Pandas, Numpy and Matplotlib libraries.

To ensure the obtained results were correct, we implemented cross-validation. For this validation, the algorithm was executed ten times for a k-fold with a value of $k = 10$. Each of the executions had 50 epochs. The advantage that it gives our model the opportunity to perform multiple training-test partitions. This can better show how our model performs on unseen data.

RESULTS AND DISCUSSION

For evaluation of the obtained results, some metrics such as accuracy, sensitivity, and area under the curve were used:

- True-Positives (TP): The predicted value was positive and agreed with the true value.
- True-Negatives (TN): The predicted value was negative and agrees with the true value.
- False-Positives (FP): The model is classified as a positive class, and the true value is negative.
- False-Negatives (FN): The model is classified as a negative class, and the actual value is positive.

Accuracy tells us the percentage of predictions that were made correctly.

$$\text{Accuracy} = \frac{TP + TN}{TP + FP + TN + FN} \quad (5)$$

The sensitivity tells us how many of the positive cases the model was able to predict correctly.

$$\text{Sensitivity} = \frac{TP}{TP + FN} \quad (6)$$

The ROC-AUC is the metric that shows us a probability curve, which is shown by sketching the range of true positives against the range of false positives at various threshold values. The results obtained with different learning rates without ROI are shown in Table 1.

TABLE 1. Performance without ROI.

Learning rate	Accuracy	Sensitivity	ROC-AUC
0.01	88.72	89.42	89.71
0.001	90.01	90.01	90.35
0.0001	91.02	93.01	89.14

The results obtained with different learning rates and ROI are shown in Table 2.

TABLE 2. Performance with ROI.

Learning rate	Accuracy	Sensitivity	ROC-AUC
0.01	91.36	92.62	92.87
0.001	92.13	93.18	92.57
0.0001	93.03	94.02	93.56

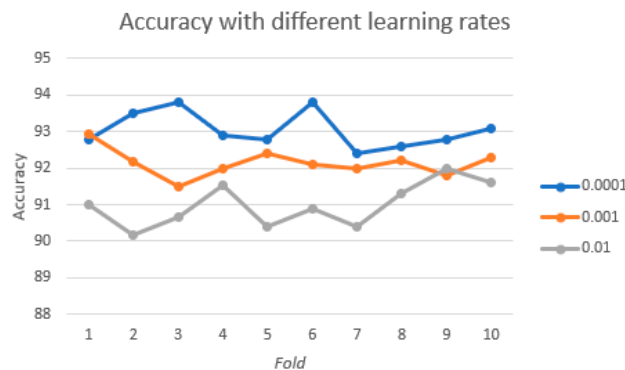


FIGURE 9. Performance with different learning rate.

Figure 10 shows the graph obtained for ROC-AUC, threshold values are in intervals of 0.01.

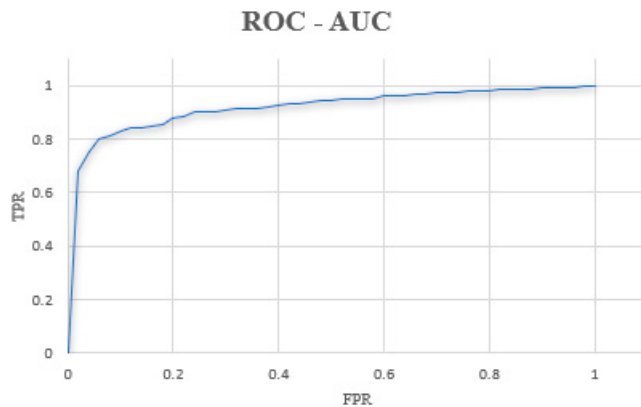


FIGURE 10. ROC-AUC.

In order to check on which part of the image the network was more focused to perform the classification, it was decided to obtain a method of visualization of neuron activations. There are several options to perform this task. Erhan *et al.* [31] propose a method that seeks to

produce an image that shows the activation of the specific neuron we are trying to visualize. Zeiler *et al.* [32] propose a method to find the patterns of the input image that activate a specific neuron in a layer of a CNN. Dosovitskiy *et al.* [33] propose a method that consists of training a neural network that performs the steps in the opposite direction to the original one so that the output of this new network is the reconstructed image.

The method used in this work is the one proposed by Selvaraju *et al.* [34] that adopts a CAM architecture, which generates a class activation map that indicates the most used image regions. Retraining is required for this purpose. In Figure 11 we can visualize the regions in the image that have the most weight while making the classification in some of the images.

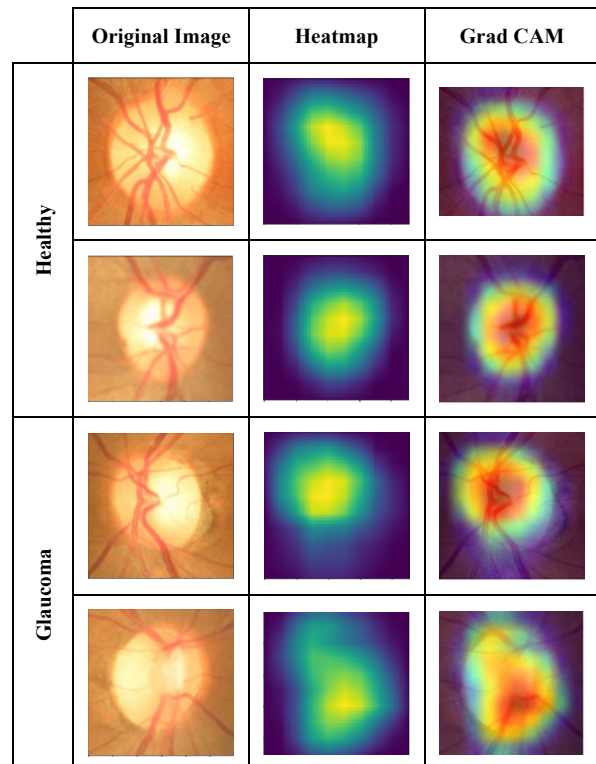


FIGURE 11. Class activation map display.

For the color map, the Jet configuration was used, which returns a color map in a three-column matrix, with the same number of rows as the color map of the original image.

Each row will have different intensities between the color red, green, and blue.

Table 3 compares the performance of our method against other methods found in the literature. It outperforms all other results in any of the displayed metrics.

TABLE 3. Comparison of our method against other methods of state-of-the-art.

Method	Performance
Six layers CNN [5]	ROC-AUC: 88.7
Different features from Gabor transform (SVM) [6]	Accuracy: 93.1 Sensitivity: 89.75 Specificity: 96.2
Eighteen layers CNN [1]	Accuracy: 98.13 Sensitivity: 98 Specificity: 98.3
GIST y PHOG (SVM) [8]	Accuracy: 83.4 ROC-AUC: 88
VGG16 + LSTM [25]	Sensitivity: 95 Specificity: 96
VGG19 + Transfer learning [26]	ROC-AUC: 94.2 Sensitivity: 87 Specificity: 89.01
Xception [27]	ROC-AUC: 96.05 Specificity: 85.8 Sensitivity: 93.46
Proposed	Accuracy: 93.03 Sensitivity: 94.02 ROC-AUC: 93.56

CONCLUSIONS

As we stated, glaucoma is one of the principal causes of blindness globally. It could be vitally important to have a tool capable of supporting ophthalmologists to diagnose this condition more quickly.

The proposed method achieves excellent metrics with a not-so-deep neural network, achieving an accuracy, sensitivity, and area under the curve of 93.22, 94.14, and 93.98, respectively. To corroborate the performance of our approach, we did our analysis on the ORIGA database, which is public, and it is one of the most used databases for glaucoma analysis.

The preprocessing of the images to obtain the ROI also helps the algorithm be more effective. It obtains the region where the optical disc is located in almost all the images of the database used, being a method to use in future work.

We will further examine different alternatives to increase the classification performance, either by pre-processing or modifying the network structure.

The purpose of this investigation is to get a high classification method that could be implemented for automatic glaucoma detection; this would save specialists time and speed up the diagnostic process.

By obtaining the characteristics map, we were able to visualize in which part of the image the decision of the network has more weight. Therefore, we conclude that the decision is made depending on the disc and optical cup characteristics, as shown in the results.

For any reader that would like to see the implementation code, it can be provided by requesting it to the corresponding author.

AUTHOR CONTRIBUTIONS

Authors H.S.-C., S.T.-A. and M.A.V.-M. conceptualized the project from the beginning. H.S.-C. acquired data and performed its curation; and participated in the following activities: data analysis, proposed the use of a CNN as classifier and the algorithm for finding the ROI, carried out the classification and research, compared the method with other glaucoma classifications, included methodology in the software, also with a visualization interface, and wrote the original draft. G.A.-F. analyzed the data and carried out the classification, validate the methods and wrote the original draft. S.T.-A. also wrote the original draft. M.A.V.-M. and J.M.R.-A. reviewed and edit the final version of the manuscript.

AKNOWLEDGMENT

We would like to thank CONACyT for partially funding the project.

ETHICAL STATEMENT

The database used in this work is public; therefore, all ethical considerations are met.

REFERENCES

- [1] Raghavendra U, Fujita H, Bhandary SV, Gudigar A, et al. Deep convolution neural network for accurate diagnosis of glaucoma using digital fundus images. *Inf Sci* [Internet]. 2018;441:41-49. Available from: <https://doi.org/10.1016/j.ins.2018.01.051>
- [2] Belghith A, Balasubramanian M, Bowd C, Weinreb RN, et al. Glaucoma progression detection using variational expectation maximization algorithm. In: 2013 IEEE 10th International Symposium on Biomedical Imaging [Internet]. San Francisco: IEEE. 2013:876-879. Available from: <https://doi.org/10.1109/ISBI.2013.6556615>
- [3] Yin F, Liu J, Wong DWJ, Tan NM, et al. Automated segmentation of optic disc and optic cup in fundus images for glaucoma diagnosis. In: 2012 25th IEEE International Symposium on Computer-Based Medical Systems (CBMS). Rome: IEEE. 2012:1-6. Available from: <https://doi.org/10.1109/CBMS.2012.6266344>
- [4] Zilly J, Buhmann JM, Mahapatra D. Glaucoma detection using entropy sampling and ensemble learning for automatic optic cup and disc segmentation. *Comput Med Imaging Graph* [Internet]. 2017;55:28-41. Available from: <https://doi.org/10.1016/j.compmedimag.2016.07.012>
- [5] Chen X, Xu Y, Kee Wong DWK, Wong TY, et al. Glaucoma detection based on deep convolutional neural network. In: 2015 37th Annual International Conference of the IEEE Engineering in Medicine and Biology Society (EMBC) [Internet]. Milan: IEEE. 2015:715-718. Available from: <https://doi.org/10.1109/EMBC.2015.7318462>
- [6] Acharya UR, Ng EYN, Eugene LW, Noronha KP, et al. Decision support system for the glaucoma using Gabor transformation. *Biomed Signal Process Control* [Internet]. 2015;15:18-26. Available from: <https://doi.org/10.1016/j.bspc.2014.09.004>
- [7] Díaz Pinto AY. Machine Learning for Glaucoma Assessment using Fundus Images [Ph.D.'s thesis]. [Valencia]: Universitat Politècnica de València, 2019. 117P.
- [8] Gour N, Khanna P. Automated glaucoma detection using GIST and pyramid histogram of oriented gradients (PHOG) descriptors. *Pattern Recognit Lett* [Internet]. 2020;137:3-11. Available from: <https://doi.org/10.1016/j.patrec.2019.04.004>
- [9] Nawaldgi S. Review of automated glaucoma detection techniques. In: 2016 International Conference on Wireless Communications, Signal Processing and Networking (WiSPNET) [Internet]. Chennai: IEEE. 2016:1435-1438. Available from: <https://doi.org/10.1109/WiSPNET.2016.7566373>
- [10] Septiarini A, Harjoko A, Pulungan R, Ekantini R. Automated Detection of Retinal Nerve Fiber Layer by Texture-Based Analysis for Glaucoma Evaluation. *Healthc Inform Res* [Internet]. 2018;24(4):335. Available from: <https://doi.org/10.4258/hir.2018.24.4.335>
- [11] Del Portillo C. Cómo Entender y Vivir Con Glaucoma. Glaucoma Research Foundation. [Internet]. 2013; Available from: http://www.glaucoma.org/GRF_Understanding_Glaucoma_ES
- [12] Li A, Wang Y, Cheng J, Liu J. Combining Multiple Deep Features for Glaucoma Classification. In: 2018 IEEE International Conference on Acoustics, Speech and Signal Processing (ICASSP) [Internet]. Calgary: IEEE. 2018:985-989. Available from: <https://doi.org/10.1109/ICASSP.2018.8462089>
- [13] Carrillo J, Bautista L, Villamizar J, Rueda J, et al. Glaucoma Detection Using Fundus Images of the Eye. In: 2019 XXII Symposium on Image, Signal Processing and Artificial Vision (STSIVA) [Internet]. Bucaramanga: IEEE. 2019:1-4. Available from: <https://doi.org/10.1109/STSIVA.2019.8730250>
- [14] Sarhan A, Rokne J, Alhajj R. Glaucoma detection using image processing techniques: A literature review. *Comput Med Imaging Graph* [Internet]. 2019;78:101657. Available from: <https://doi.org/10.1016/j.compmedimag.2019.101657>
- [15] Li L, Xu M, Liu H, Li Y, et al. A Large-Scale Database and a CNN Model for Attention-Based Glaucoma Detection. *IEEE Trans Med Imaging* [Internet]. 2020;39(2):413-424. Available from: <https://doi.org/10.1109/TMI.2019.2927226>
- [16] Zhang Z, Lee BH, Liu J, Wong DWK, et al. Optic disc region of interest localization in fundus image for Glaucoma detection in ARGALI. In: 2010 5th IEEE Conference on Industrial Electronics and Applications [Internet]. Taichung: IEEE. 2010:1686-1689. Available from: <https://doi.org/10.1109/ICIEA.2010.5515221>
- [17] Rani A, Mittal D. Measurement of Arterio-Venous Ratio for Detection of Hypertensive Retinopathy through Digital Color Fundus Images. *J Biomed Eng Med Imaging* [Internet]. 2015;2(5):35. Available from: <https://doi.org/10.14738/jbemi.25.1577>
- [18] Zhang Z, Yin FS, Liu J, Wong WK, et al. ORIGA-light: An online retinal fundus image database for glaucoma analysis and research. In: 2010 Annual International Conference of the IEEE Engineering in Medicine and Biology [Internet]. Buenos Aires: IEEE. 2010:3065-3068. Available from: <https://doi.org/10.1109/EMBS.2010.5626137>
- [19] Sng CC, Foo L-L, Cheng C-Y, Allen JC, et al. Determinants of Anterior Chamber Depth: The Singapore Chinese Eye Study. *Ophthalmology* [Internet]. 2012;119(6):1143-1150. Available from: <https://doi.org/10.1016/j.ophtha.2012.01.011>
- [20] Decencière E, Zhang X, Cazuguel G, Lay B, et al. Feedback on a publicly distributed image database: the Messidor database. *Image Anal Stereol* [Internet]. 2014;33:231-234. Available from: <https://doi.org/10.5566/ias.1155>
- [21] Brandon L, Hoover A. Drusen Detection in a Retinal Image Using Multi-level Analysis. In: Ellis R.E., Peters T.M. (eds). *Medical Image Computing and Computer-Assisted Intervention - MICCAI 2003* [Internet]. Springer, Berlin, Heidelberg: Lecture Notes in Computer Science. 2003:618-625p. Available from: https://doi.org/10.1007/978-3-540-39899-8_76
- [22] Sivaswamy J, Krishnadas SR, Joshi GD, Jain M, et al. Drishti-GS: Retinal image dataset for optic nerve head segmentation. In: 2014 IEEE 11th International Symposium on Biomedical Imaging (ISBI) [Internet]. Beijing: IEEE. 2014:53-56. Available from: <https://doi.org/10.1109/ISBI.2014.6867807>
- [23] Han J, Kamber M, Pei J. *Data Mining: Concepts and Techniques* [Internet]. Waltham: Elsevier. 2011:113-114p. Available from: <https://doi.org/10.1016/B978-0-12-381479-1.00016-2>

- [24] Bhatkalkar BJ, Reddy DR, Prabhu S, Bhandary S. Improving the Performance of Convolutional Neural Network for the Segmentation of Optic Disc in Fundus Images Using Attention Gates and Conditional Random Fields. *IEEE Access* [Internet]. 2020;8:29299-29310. Available from: <https://doi.org/10.1109/ACCESS.2020.2972318>
- [25] Gheisari S, Shariflou S, Phu J, Kennedy PJ, et al. A combined convolutional and recurrent neural network for enhanced glaucoma detection. *Sci Rep* [Internet]. 2021;11(1):1995. Available from: <https://doi.org/10.1038/s41598-021-81554-4>
- [26] Gómez-Valverde J, Antón A, Fatti G, Liefers B, et al. Automatic glaucoma classification using color fundus images based on convolutional neural networks and transfer learning. *Biomed Opt Express* [Internet]. 2019;10(2):892-913. Available from: <https://doi.org/10.1364/BOE.10.000892>
- [27] Diaz-Pinto A, Morales S, Naranjo V, Köhler T, et al. CNNs for automatic glaucoma assessment using fundus images: an extensive validation. *BioMed Eng Online* [Internet]. 2019;18(1):1-19. Available from: <https://doi.org/10.1186/s12938-019-0649-y>
- [28] Unión Internacional de Telecomunicaciones. Parámetros de codificación de televisión digital para estudios con formatos de imagen normal 4:3 y de pantalla ancha 16:9. ITU [Internet]. 2011; Available from: RECOMENDACIÓN UIT-R BT.601-7 - Parámetros de codificación de televisión digital para estudios con formatos de imagen normal 4:3 y de pantalla ancha 16:9 (itu.int)
- [29] Simonyan K, Zisserman A. Very Deep Convolutional Networks for Large-Scale Image Recognition. *arXiv* [Internet]. 2014; Available from: <https://arxiv.org/abs/1409.1556>
- [30] Krizhevsky A, Sutskever I, Hinton GE. ImageNet classification with deep convolutional neural networks. *Commun [Internet]*. 2017; 60(6):84-90. Available from: <https://doi.org/10.1145/3065386>
- [31] Erhan D, Bengio Y, Courville AC, Vincent P. Visualizing Higher-Layer Features of a Deep Network [Internet]; 2009. Report 1341. Available from: (PDF) Visualizing Higher-Layer Features of a Deep Network (researchgate.net)
- [32] Zeiler MD, Taylor GW, Fergus R. Adaptive deconvolutional networks for mid and high level feature learning. In: 2011 International Conference on Computer Vision [Internet]. Barcelona: IEEE. 2011:2018-2025. Available from: <https://doi.org/10.1109/ICCV.2011.6126474>
- [33] Dosovitskiy A, Brox T. Inverting Visual Representations with Convolutional Networks. In: 2016 IEEE Conference on Computer Vision and Pattern Recognition (CVPR) [Internet]. Las Vegas: IEEE. 2016:4829-4837. Available from: <https://doi.org/10.1109/CVPR.2016.522>
- [34] Selvaraju RR, Cogswell M, Das A, Vedantam R, et al. Grad-CAM: Visual Explanations from Deep Networks via Gradient-Based Localization. In: 2017 IEEE International Conference on Computer Vision (ICCV) [Internet]. Venice: IEEE. 2017:618-626. Available from: <https://doi.org/10.1109/ICCV.2017.74>

dx.doi.org/10.17488/RMIB.42.3.3

E-LOCATION ID: 1192

Identification of 7 Movements of the Human Hand Using sEMG - 360° on the Forearm

Identificación de 7 Movimientos de la Mano Humana Utilizando sEMG - 360° en el Antebrazo

A. Ibarra-Fuentes, E. Morales-Sánchez

Instituto Politécnico Nacional. CICATA-IPN Unidad Querétaro. México.

ABSTRACT

This document shows the identification of 7 gestures (movements) of the human hand from sEMG - 360° signals on the forearm. sEMG - 360° is the sEMG measurement through 8 channels every 45° making a total of 360°. When making a hand gesture, there will be 8 independent sEMG signals that will be used to identify the gesture. The 7 gestures to identify are: relaxed hand (closed), open hand (fingers extended), flexion and extension of the little finger, the ring finger, the middle finger, the index finger, and the thumb separately. One hundred samples for each gesture were captured and 3 feature extraction methods were applied in the time domain: mean absolute value (MAV), root mean square value (RMS) and area under the curve (AUC). A vector support machine (SVM) classifier was applied to each extractor. The gestures were identified and the percentage of accuracy in the identification was calculated for each extractor + SVM classifier using the confusion matrix method and including the 8 channels for each gesture. An accuracy of 99.52% was achieved for the identification of the 7 gestures applying sEMG - 360°.

KEYWORDS: Electromyography; gesture; classifier

RESUMEN

Este documento muestra la identificación de 7 gestos (movimientos) de la mano humana a partir de sEMG - 360° en el antebrazo. sEMG-360 es la medición de sEMG por medio de 8 canales cada 45° haciendo un total de 360°. Al realizar un gesto de la mano se tendrán 8 señales sEMG independientes que se utilizarán para hacer la identificación del movimiento. Los 7 gestos a identificar fueron: mano relajada (cerrada), mano abierta (dedos extendidos), flexión y extensión del dedo meñique, del dedo anular, del dedo medio, del dedo índice y del dedo pulgar por separado. Se capturaron 100 muestras de cada gesto y se aplicaron 3 métodos de extracción de características en el dominio del tiempo: el valor medio absoluto (MAV), valor de la raíz cuadrática media (RMS) y el valor del área bajo la curva (AUC), después se aplicó un clasificador de máquina de soporte vectorial (SVM) a cada método de extracción. Se identificaron los movimientos y se calculó el porcentaje de exactitud en la identificación para cada extractor + clasificador SVM utilizando el método de la matriz de confusión e incluyendo los 8 canales para cada gesto. Se logró un 99.52% de exactitud en la identificación de los gestos de la mano humana aplicando sEMG - 360°.

PALABRAS CLAVE: Electromyography, gestures, classifier

Corresponding author

TO: Eduardo Morales Sánchez

INSTITUTION: Instituto Politécnico Nacional

ADDRESS: Av. Luis Enrique Erro S/N, Unidad Profesional

Adolfo López Mateos, Col. Zacatenco, Alc. Gustavo A.

Madero, C. P. 07738, CDMX, México

E-MAIL: emoraless@ipn.mx

Received:

18 June 2021

Accepted:

4 November 2021

INTRODUCTION

Electromyography is a technique that measures the bioelectrical signals that muscles generate when the body performs an action; these signals have been used for the performance analysis of athletes, for the remote control of highly complex mechanical and electronic systems in movement, to measure development in rehabilitation, among other applications. sEMG signals are acquired by means of surface electrodes.

The literature reports the use of 1, 2 and up to 3 electrode arrays using the RLD (Right Leg Driven) configuration. The commercial device called Myo Armband, Thalmic labs [1], is a wireless electronic bracelet consisting of 8 channels (8 arrays of 3 mini dry-surface electrodes). When this bracelet of 8 arrangements of 3 superficial electrodes is positioned on the forearm, you have a complete overview of the sEMG signals of the forearm muscles when the hand performs any movement. This way of measuring EMG around a human extremity is called sEMG-360°.

In recent years, different researches have considered sEMG signals to identify the intention of movement of the human hand and to be able to reproduce them in a robotic hand. These signals are acquired when different gestures (movements) are made and then they are processed to acquire the most important information of the signal and once processed they can be entered into a classifier in order to identify the movements made by the user.

Tavakoli et al. [2] reports the sEMG signals of the forearm when certain movements are performed: open hand, closed hand, hand at rest and wrist flexion, these are acquired with the use of 3 superficial electrodes, then an extraction of characteristics is made in the time domain to the signals, where the mean value (MV) of each of them is obtained, then an SVM classifier is used to predict the movements, where they obtained an accuracy of 90%.

Another study presented by Shi et al. [3], where superficial electrodes are used to acquire the sEMG signals from the forearm when performing 4 gestures such as: closed hand, extended index finger, extended thumb, and the 4 extended fingers together. An extraction of characteristics in the time domain was applied, where the main descriptors were: the MAV, the zero crossing (ZC), the slope sign change (SSC) and the waveform length (WL), these characteristics were used in the nearest neighbor classifier (KNN) where they obtained an accuracy of 94%.

In the study presented by Krishnan et al. [4], the Myo Armband device is used to acquire EMG signals by performing 5 movements of the human hand. The author used some feature extraction methods in the time domain as the simple square integral (SSI), the maximum value and the minimum value, the average frequency and the average potential; these methods were used in an SVM classifier where they obtained an identification accuracy percentage of 92.4% for one user and 84.27% for another user.

In Mukhopadhyay et al. [5], 8 arrays of 3 electrodes are used to predict 8 classes of hand movement: wrist flexion, wrist extension, wrist pronation, wrist supination, force grip, pinch grip, open hand, and rest. Powerspectral descriptors were used to extract the characteristics of the sEMG signals. Subsequently, they used a deep neural network (DNN) as a classifier, obtaining 98.88% accuracy.

In the study presented by Sanchez et al. [6], the author obtained sEMG signals by using the Myo Armband bracelet to predict 8 hand gestures to reproduce on a robotic hand. They used an extraction of characteristics in the time domain as MAV, the RMS, the WL, the mean amplitude change (AAC), the integrated EMG value (IEMG) and the absolute standard deviation (DASDV); these data were used in an extended associative memory (EAM) classifier and obtained an accuracy of 94.83% when using the MAV and RMS extractors.

Table 1 shows a summary of the previous literature that includes different characteristics such as the number of electrodes, their position, number of gestures, type of feature extraction method, and the identification accuracy.

TABLE 1. Summary of the previous works in the state of the art about EMG and classification of gestures.

Article	No. of Electrodes on forearm	No. Of Gesture	Feature extraction method	Classifier	Accuracy (%)
Tavakoli et al [2]	1	4	MV	SVM	90
Shi et al [3]	2	4	MAV, ZC, SSC and WL	KNN	94
Krishnan et al [4]	8	5	SSI, Max, Min, MF and MP	SVM	92.4-84.27
Mukhopadhyay et al [5]	7	8	fTDD	DNN SVMK NNRF DT	98.66, 90.64, 91.78, 88.36
Sanchez et al [6]	8	8	IEMG, MAV, VAR, RMS, DASDV AAC and WL	EAM	95.83

From the previous review it can be seen that there are different articles on the identification of some hand gestures using different extractors and classifiers [7] with 1, 2, 4, and 8 array electrodes but with different identification accuracy percentage. Due to the random nature of sEMG signals, it is of the researchers' interest to improve the identification accuracy of human hand gestures using EMG signals.

The present work proposes to improve the gesture accuracy identification using only sEMG-360 array and keeping the same feature extraction methods (MAV, RMS and AUC) in the time domain and the SVM classifier to identify 7 gestures of the human hand.

MATERIALS AND METHODS

This section shows the methodology used to extract the characteristics of the sEMG-360 signals acquired (in the 8 channels at 45° around the forearm) corre-

sponding to 7 movements of the human hand: open hand (5 fingers extended), closed hand (5 fingers flexed), and 5 flexion-extension movements for each finger individually, as well as to explain the method used to evaluate the performance of the identification.

Myo Armband bracelet

It is an electronic device developed by the Thalmic Lab company as illustrated in Figure 1 [1]. It is a bracelet that can be placed on the forearm to record the sEMG activity that is generated by the movement of the muscles. This device has 8 arrays of 3 dry-surface electrodes to monitor sEMG, it combines an accelerometer, a gyroscope, a magnetometer, an ARM Cortex M4 processor, indicator LEDs, motor vibrators, Bluetooth communication and a rechargeable power supply.

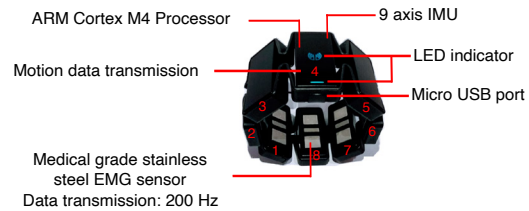


FIGURE 1. Characteristics of the Myo Armband.

The sampling frequency of the Myo Armband bracelet is 200 Hz. The total sample rate of the Myo Armband is 200 Hz, which gives us a sample time as shown in Equation 1:

$$T_{sampling} = 1/200 \text{ Hz} = 5ms \quad (1)$$

Where $T_{sampling}$ is the sampling time, Hz is the sample rate and ms equals milliseconds.

This indicates that every 5 ms, the EMG signals of the 8 channels are acquired in 360° configuration of the Myo Armband bracelet.

Acquisition of EMG signals

The Myo Armband device was used to acquire the 8 sEMG signals (8 channels) for each flexion-extension movement of the fingers of the human hand, the

extended hand position (open) and the relaxed hand (closed). By means of Bluetooth (integrated in the device) and using the Python software, each of the 8 channels of each of the established movements were captured and saved on a PC for later analysis.

A window of 400 data was generated as shown in Figure 2, where the sEMG signals of the 8 channels are graphed. The movement developed in Figure 2 corresponds to the flexion-extension movement of the middle finger. A segment of 400 samples represents 2 seconds of the signal, though the gesture took 1 second, the rest is the time interval before and after the gesture.

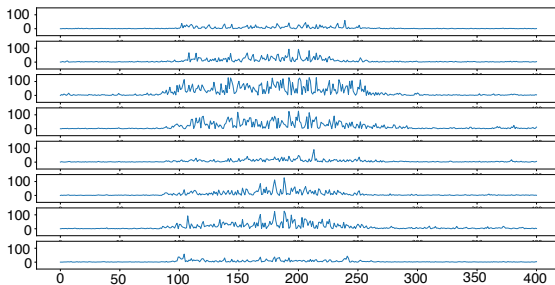


FIGURE 2. sEMG signals of the 8 channels, corresponding to the flexion-extension movement of the middle finger.

Once the sEMG signals were acquired for the preset gestures, feature extraction methods of the 8 channels were performed for the 7 motions. These feature extractions were performed in the time domain. It was proposed to implement 3 types of extractors, which are the most reported in the literature: the mean absolute value method (MAV) [8], the root mean square (RMS) method [9] and the area method under the curve (AUC) [6].

In the MAV method, the mean value of the sEMG signal is calculated. The formula to calculate it is shown in Equation 2.

$$\text{MAV} = \frac{1}{N} \sum_{i=1}^N |X_i| \quad (2)$$

Where N represents the number of data contained in the sample and X_i the data contained in said sample.

The RMS method obtains the root mean square value of the sEMG signal. The mathematical expression is shown in Equation 3.

$$\text{RMS} = \sqrt{\frac{1}{N} \sum_{i=1}^N X_i^2} \quad (3)$$

Where N represents the number of data contained in the sample and X_i the data contained in said sample.

The area method consists of applying the trapezoid rule as an approximation of the definite integral by adding the areas of the trapezoids that make up the sEMG signal. The formula for calculating the area under the curve is shown in Equation 4.

$$T_N(f) = \frac{\Delta x}{2} \sum_{i=1}^N (f(x_i) + f(x_{i-1})) \quad (4)$$

Where $\Delta x = (b-a) / N$ is the length of the subintervals and $X_i = a + i \Delta x$. The values of a and b belong to the interval where the integral will be evaluated.

Classifier

Once the feature extraction has been carried out using each of the proposed extraction methods, a classifier is required to be applied to separate the information and identify each movement. For this study, the support vector machine classifier (SVM) is used, where 100 data of each of the predefined gestures will be used. The data used for SVM can be more or less than one hundred, according to literature, one hundred is a representative number when statistics is applied [10] [11] [12]; the SVM classifier is an algorithm that can determine a plane that separates the acquired data set into several sets (vectors). For a new set, the similarity of the vector is determined, and it is classified within the set associated with that vector.

SVM algorithms use a set of mathematical functions called kernels. There are different types of kernel functions, such as: linear, polynomial, radial basis function (RBF) among others. Depending on the type of kernel, an accurate or inaccurate classification of the data is achieved.

The kernel functions are represented as:

- Linear: $z = y * x + b$
- Polynomial: $z = (y * x + b)^n$
- RBF: $z = \exp(-\gamma \|x - y\|^2)$

Where x and y are the data that is entered into the classifier, b is a parameter to improve performance and n is the degree of the polynomial, γ defines how much influence a single training example has.

In this work, the 3 types of kernels were applied for the SVM in order to determine which kernel maximizes the percentage of accuracy in the identification of movements.

Confusion matrix

In order to calculate the percentage of accuracy that exists during an identification process, the confusion matrix is used.

In the confusion matrix, each column represents the number of predictions for each class, and the rows represent the instances of the real class, so it is possible to observe the successes and errors of the model during the identification of the movement [13]. Figure 2 shows a confusion matrix for 4 classes: A, B, C and D.

To calculate the accuracy value (AC), Equation 5 [14] is used.

$$AC = \frac{T}{T+FAB+FAC+FAD+FBA+\dots+FDC+FCD} \quad (5)$$

Where $T = VA + VB + VC + VD$; VA , VB , VC and VD are the numbers where the classes are identified as true. $FAB\dots FCD$ is the number in which a class is classified in another class. With 100% accuracy, all the values for $FAB\dots FCD$ are 0.

TABLE 2. Confusion matrix for 4 classes.

		Actual Class				
		A	B	C	D	...
Predicted Class	A	VA	FAB	FAC	FAD	...
	B	FBA	VB	FBC	FBD	...
	C	FCA	FCB	VC	FCD	...
	D	FDA	FDB	FDC	VD	...

RESULTS AND DISCUSSION

Since each gesture has 8 associated sEMG channels, it is ideal to find the relationship of the 8 channels with the gesture. One technique used is to graph the data in an eight-dimensional space (number of channels). To simplify and show graphically this relationship, Figure 3 shows the corresponding three-dimensional space data for channels 1, 2 and 6 of each of the 7 movements using the MAV extractor (different colors). It is observed that the classes are separated since they are in different ranges within the three-dimensional space. It is observed that the open hand and closed hand gestures are naturally separated from the gestures of moving a single finger. It is also observed that the little finger, middle finger and ring finger are the gestures that least allow classification because they overlap each other.

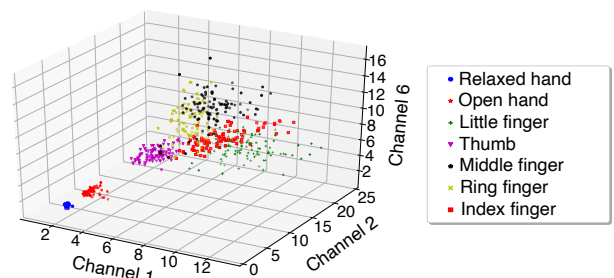


FIGURE 3. MAV characteristics of channels 1, 2 and 6.

The behavior was calculated for the CUA and RMS extractors. There were no significant differences between them.

Once the MAV, AUC and RMS feature extractors were applied to the sEMG signals, the SVM classifier was applied. Figure 4 shows the classification carried out by the SVM with a linear kernel of the data obtained from the MAV for channels 1 and 6. It is observed that there are some data that were misclassified since they are in the region of a different class.

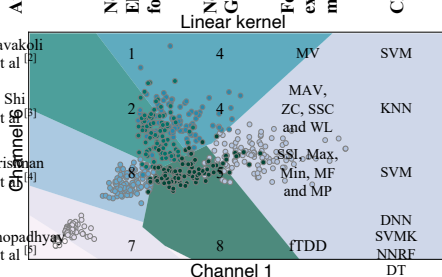


FIGURE 4. Classification of data obtained from the MAV when using a linear kernel in the SVM.

Considering the classification obtained from the classes with 100 samples for each gesture, the corresponding confusion matrix was obtained (Table 3). 70% of the data was used for training and the remaining 30% for testing. Table 2 was obtained for a linear kernel SVM.

TABLE 3. Confusion matrix for the identification of the 7 movements. Shown for SVM with RMS as feature extraction method.

	(1)	(2)	(3)	(4)	(5)	(6)	(7)
(1)	30	0	0	0	0	0	0
(2)	0	30	0	0	0	0	0
(3)	0	0	30	0	0	0	0
(4)	0	0	0	30	0	0	0
(5)	0	0	0	0	30	0	0
(6)	0	0	0	0	0	30	0
(7)	0	0	0	0	3	0	27

In Table 3, number (1) refers to the gesture of the closed hand, number (2) the open hand, number (3) is the flexion-extension (FE) of the little finger, number (4) is for FE of the thumb, number (5) for FE of the middle finger, number (6) for FE of the ring finger and finally number (7) refers to FE of the index finger. In the same way, the black-colored diagonal values show the successes that a class has in respect to itself, and the other values that are outside the diagonal, refer to how many times the classifier predicted a value of a class that does not belong to the assigned one.

Table 4 shows the percentage of accuracy in the identification of the 7 gestures. It is shown that the RMS + SVM with the linear kernel, RMS + SVM with rbf kernel and AUC + SVM with rbf kernel obtained the highest percentage of accuracy in the identification with 99.52%.

TABLE 4. Percentage of accuracy in the identification of gesture under different extractors and kernels.

Article	Extractor	SVM kernel	Accuracy %
This work	MAV	Linear	98.57
	MAV	Polynomial	99.04
	MAV	RBF	98.09
	RMS	Linear	99.52
	RMS	Polynomial	99.04
	RMS	RBF	99.52
	AUC	Linear	98.57
	AUC	Polynomial	99.04
	AUC	RBF	99.52
Tavakoli et al [2]	MV	Gaussian	90.00
Krishnan et al [4]	SSI, Max, Min, MF and MP	Linear	92.4 and 84.27
Mukhopadhyay et al [5]	fTDD	Linear	98.66

The RBF hyperparameters used were $C = 10000.0$ and $\text{Gamma} = 1e-05$ for MAV feature, for RMS were used $C = 10000000$ and $\text{Gamma} = 1e-09$, and for the AUC the value of $C = 100.0$ and $\text{Gamma} = 1e-09$. The Polynomial parameter degrees used for MAV, RMS and AUC were the value of 2.

As shown in Table 4, the best combination of extractor + classifier was that of RMS + SVM with linear kernel also the RMS +SVM and AUC + SVM with the RBF kernel. In a general analysis, it can be observed that there was no significant difference between the feature extraction methods.

According to Table 4, in all the cases we have a high-percentage of identification accuracy, this means that realistically, the sEMG-360 could improve the accuracy. This result was expected because having 8 channels for each gesture to identify is a real advantage comparing with literature (Table 1). In the introduction, Mukhopadhyay et al. [5] using 8 arrays of 3 electrodes to predict 8 gestures and using a deep neural network (DNN) as a classifier, 98.98% accuracy was obtained. This high accuracy may be because the author used 8 electrodes, as we did, as well as a DNN classifier. In our case, identification accuracy is in the range of 98.5-99.5% in all the cases. In a different way, it is observed that a second parameter for increased identification accuracy is the classifier SVM. And a third parameter is the feature extraction method. According with our results, RMS is the better extraction method compared to MAV and AUC. At last, from a computational point of view, RMS + SVM implementation is very easy if compared to the DNN classifier.

Therefore, this research shows that s-EMG-360 improves the accuracy of identification though it is used with the common feature extraction method (RMS, MAV, AUC) and SVM classifier.

CONCLUSIONS

The results show that the RMS extractor in conjunction with the SVM classifier is the combination with the best percentage of accuracy (99.52%) in the identification of the 7 proposed movements of the fingers of the human hand.

It is shown that using a Myo Armband device is a good option for the implementation of the sEMG-360 method.

The sEMG-360 method improves the identification accuracy of human hand gestures. The SVM classifier was the second principal parameter to improve identification accuracy.

It is concluded that the feature extraction methods in the time domain (MAV, AUC and RMS) give the same result for identification accuracy, with RMS having a slight advantage.

At last, we concluded that sEMG-360 around the forearm is a powerful technique because it adds 8 sEMG to the processing data for gesture identification.

AUTHOR CONTRIBUTIONS

E.M.S. conceptualized the project, obtained funding for the research, and developed the methodology implemented in the project. A.I.F. developed the software used in the classification of gestures and movements as well as the one used for the storage of the sEMG signals, he also oversaw the data curation and research for the EMG signals and carried out the validation of the movements and the formal analyses of data. Both authors work equally in the writing and editing of the different versions of the manuscript until complete the final version.

ACKNOWLEDGMENTS

Author Adrian Ibarra thanks the “Consejo Nacional de Ciencia y Tecnología” (CONACYT-Mexico) for his Master post-graduate scholarship. This research was funded by Instituto Politécnico Nacional (IPN) through SIP20196083, SIP20200568 and SIP20211175 projects.

REFERENCES

- [1] Visconti P, Gaetani F, Zappatore GA, Primiceri P. Technical Features and Functionalities of Myo Armband: An Overview on Related Literature and Advanced Applications of Myoelectric Armbands Mainly Focused on Arm Prostheses. *Int J Smart Sens Intell Syst* [Internet]. 2018;11(1):1-25. Available from: <https://doi.org/10.21307/iissis-2018-005>
- [2] Tavakoli M, Benussi C, Lourenco JL. Single channel surface EMG control of advanced prosthetic hands: A simple, low cost and efficient approach. *Expert Syst Appl* [Internet]. 2017;79:322-322. Available from: <http://dx.doi.org/10.1016/j.eswa.2017.03.012>
- [3] Shi W-T, Lyu Z-J, Tang S-T, Chia T-L, et al. A bionic hand controlled by hand gesture recognition based on surface EMG signals: A preliminary study. *Biocybern Biomed Eng* [Internet]. 2018;38(1):126-135. Available from: <http://dx.doi.org/10.1016/j.bbe.2017.11.001>
- [4] Krishnan KS, Saha A, Ramachandran S, Kumar S. Recognition of human arm gestures using Myo armband for the game of hand cricket. 2017 IEEE 5th Int Symp Robot Intell Sensors (IRIS) [Internet]. Ottawa: IEEE; 2017:389-394. Available from: <https://doi.org/10.1109/IRIS.2017.8250154>
- [5] Mukhopadhyay AK, Samui S. An experimental study on upper limb position invariant EMG signal classification based on deep neural network. *Biomed Signal Process Control* [Internet]. 2020;55:101669. Available from: <https://doi.org/10.1016/j.bspc.2019.101669>
- [6] Sánchez Velasco LE, Arias Montiel M, Guzmán Ramírez E, Lugo E. A low-cost EMG-controlled anthropomorphic robotic hand for power and precision grasp. *Biocybern Biomed Eng* [Internet]. 2020;40(1):221-237. Available from: <https://doi.org/10.1016/j.bbe.2019.10.002>
- [7] Rascón-Madrigal LH, Sinecio-Sidrian MA, Mejía-Muñoz JM, Díaz-Román JD, Canales-Valdiviezo I, Botello-Arredondo AI. Estimación en la Intención de Agarres: Cilíndrico, Esférico y Gancho Utilizando Redes Neuronales Profundas. *Rev Mex Ing Biomed* [Internet]. 2020;41(1):117-127. Available from: <https://dx.doi.org/10.17488/RMIB.41.1.9>
- [8] Veer K, Sharma T. Extraction and Analysis of above elbow SEMG for Pattern classification. *J Med Eng Technol* [Internet]. 2016;40(4):149-154. Available from: <https://doi.org/10.3109/03091902.2016.1153739>
- [9] Phinyomark A, Phukpattaranont P, Limsakul C. Feature reduction and selection for EMG signal classification. *Expert Syst Appl* [Internet]. 2012;39(8):7420-7431. Available from: <http://dx.doi.org/10.1016/j.eswa.2012.01.102>
- [10] Resendiz Trejo J. Las máquinas de vectores de soporte para identificación en línea. México [Master's thesis]. [Honolulu]: Centro de Investigaciòn y de Estudios Avanzados del Instituto Politécnico Nacional, 2006. 84p
- [11] Alkan A, Günay M. Identification of EMG signals using discriminant analysis and SVM classifier. *Expert Syst Appl* [Internet]. 2012;39(1):44-47. Available from: <http://dx.doi.org/10.1016/j.eswa.2011.06.043>
- [12] Hassan HF, Abou-Loukh SJ, Ibraheem IK. Teleoperated robotic arm movement using electromyography signal with wearable Myo armband. *J King Saud Univ Eng Sci* [Internet]. 2020;32(6):378-387. Available from: <https://doi.org/10.1016/j.jksues.2019.05.001>
- [13] Ting KM. Confusion Matrix. In: Sammut C, Webb GI, editors. *Ency Mach Learn* [Internet]. Boston, MA: Springer US; 2010. 209p. Available from: https://doi.org/10.1007/978-0-387-30164-8_157
- [14] Shamsudin NF, Basiron H, Saaya Z, Rahman AFNA, et al. Sentiment classification of unstructured data using lexical based techniques. *J Teknol* [Internet]. 2015;77(18):113-120. Available from: <https://doi.org/10.11113/jt.v77.6497>

dx.doi.org/10.17488/RMIB.42.3.4

E-LOCATION ID: 1195

Shielding Volume Reduction in a High Dose Rate Brachytherapy Room

Reducción de Volumen de Blindaje en una Sala de Braquiterapia de Alta Tasa de Dosis

S. González-Guzmán¹, H. M. Montenegro-Monroy¹, J. Pérez-Honorato², M. A. Martínez-Flores³, F. Miranda-Suárez²

¹Universidad Autónoma del Estado de México

²Centro Oncológico Estatal del Instituto de Seguridad Social del Estado de México y Municipios (ISSEMyM)

³Dirección de Gestión y Control del Instituto de Seguridad Social del Estado de México y Municipios (ISSEMyM)

ABSTRACT

This paper describes a method to reduce the shielding thickness in a high dose brachytherapy treatment room, with an Iridium-192 source, using the protocols established by the International Atomic Energy Agency in its Safety Report No. 47; calculating the volume of shielding material, without failing to comply with the radiation safety parameters established by the General Radiation Safety Regulations and regulations in force by the *Comisión Nacional de Seguridad Nuclear y Salvaguardias*, which acts as the regulatory body for the use of radioactive sources in Mexico. The shielding of the walls was determined as a function of room design, source activity, workload, use factor, number of weekly treatments, treatment time, and shielding material properties. The results show that the shielding volume can be reduced by 19.592% and 20.727% for five-point and eleven-point fractionation, respectively, for a Brachytherapy room with a maze.

KEYWORDS: Shielding, Brachytherapy, Radiation Protection

RESUMEN

El presente trabajo describe un método para reducir el grosor de blindaje en una sala de tratamiento de Braquiterapia de alta dosis con fuente de Iridio-192, utilizando los protocolos establecidos por el Organismo Internacional de Energía Atómica en su Informe de Seguridad No. 47; calculando el volumen de material de blindaje, sin incumplir con los parámetros de seguridad radiológica que establece el Reglamento General de Seguridad Radiológica y normatividad vigente por la Comisión Nacional de Seguridad Nuclear y Salvaguardias, quien funge como órgano regulador para el uso de fuentes radiactivas en México. Por lo que se determinó el grosor de las paredes en función al diseño de la sala, ubicación y actividad total de la fuente, así como, factor de ocupación en áreas adyacentes carga de trabajo, factor de uso, número de tratamientos semanales, tiempo promedio de tratamiento y propiedades del material de blindaje. Mediante estos cálculos, se determinó que el volumen de blindaje se puede reducir un 19.592% y 20.727% para el fraccionamiento en cinco y once puntos, respectivamente, para una sala de Braquiterapia con laberinto.

PALABRAS CLAVE: Blindaje, Braquiterapi, Protección Radiológica

Corresponding author

TO: Jonathan Pérez Honorato

INSTITUTION: Centro Oncológico Estatal del Instituto de Seguridad Social del Estado de México y Municipios (ISSEMyM)

ADDRESS: Av. Solidaridad Las Torres #101, Col. Del Parque, C. P. 50180, Toluca, Estado de México, México

E-MAIL: jonathanperezhonorato@yahoo.com.mx

Received:

24 June 2021

Accepted:

3 December 2021

INTRODUCTION

Radiation protection (RP) focuses on the prevention of stochastic and deterministic damage caused by ionizing radiation to workers, the public, and the environment, without interfering with the exposure processes associated with a benefit, ranging from electric power generation to applications in medicine, industry, and agriculture [1] [2] [3].

RP is the responsibility of each country; however, there are international organizations such as the International Atomic Energy Agency (IAEA) and the International Commission on Radiological Protection (ICRP), which issue recommendations on radioprotection to reduce risks and prevent accidents, respond to emergencies associated with radioactive sources and seek to mitigate harmful effects associated with radiological exposure practices; environmental, occupational, or public [3] [4].

It is important to mention that the RP is based on the principles of:

- Justification: Any practice involving exposure to ionizing radiation should produce more benefit than harm [1].
- Optimization: All radiation exposure should be kept As Low As Reasonably Achievable (ALARA Principle) [1].
- Dose limits: applicable for planned and justified radiation exposure [1].

The first two are aimed at the use of the radioactive source, and the third one, for exposed personnel and the public [5], regulating the dose limits in force. In Mexico, the *Comisión Nacional de Seguridad Nuclear y Salvaguardias* (CNSNS -National Commission for Nuclear Safety and Safeguards-) is the regulatory body for the use of radioactive sources, and the effective

dose equivalent were published in the *Reglamento General de Seguridad Radiológica* (General Regulation of Radiological Safety). These values and the recommended values by the ICRP are measured in millisievert (mSv) and shown in Table 1.

TABLE 1. Summary of effective exposure limits in planned situations [8][9]

Dose limit	Occupationally exposed personnel	Public
Reglamento General de Seguridad Radiológica	50 mSv/year for stochastic effects	5 mSv/year for stochastic effects
	500 mSv/year for deterministic effects	50 mSv/year for deterministic effects
ICRP	100 mSv/5 years conditional on not exceeding 50 mSv per year	1 mSv/year
Crystalline	150 mSv	5 mSv
Skin	500 mSv	50 mSv
Hands and feet	500 mSv	-

Also, there are RP factors or practical RP methods [6], which are:

- Time: The less time an individual is exposed to a radiation source, the lowest dose absorbed [7].
- Distance: Every individual should be as far away as possible from the radiation source, according to the inverse square law of distance, which indicates that it is inversely proportional to the square of the distance from the source [4] [7].
- Shielding: Barrier between the source and the individual that reduces the intensity of ionizing radiation [7].

These factors should be considered to optimize the RP design [6]. Regarding shielding, it depends on activity, type of radiation and energy emitted by the source,

which is directly related to the type of particles released by the radionuclide (emissions α , β^+ , β^- , γ , etc.) [7], as well as the density and thickness of the material. Nowadays, the most used materials are concrete, lead, and steel [7] [10], whose description and density are shown in Table 2.

TABLE 2. Examples of radiological shielding materials [11].

Material	Comments
Concrete	Its density varies with mineral content.
Steel /Lead	It is normally used as supplementary shielding.

Regarding medical use, radioactive sources are used in diagnosis, treatment [1], and *theragnostic* [12]. Particularly in treatments, there are *teletherapy* and *brachytherapy*.

Brachytherapy is a treatment in which radioactive sources are placed at a short distance from the tumor. It is classified according to dose rate or how quickly the dose is delivered to the patient: low, medium, and high [13]. In the case of *High Dose Rate Brachytherapy* (HDR-B), the most radioactive isotopes used are Cobalt-60 (^{60}Co) and Iridium-192 (^{192}Ir) [11]. Particularly, ^{192}Ir has a half-life of 73,829 days and decays 95.35% by particle emission β and 4.65% by *Electronic Capture* (EC) to excited states of *Platinum-192* (^{192}Pt) and *Osmium-192* (^{192}Os) respectively. Afterwards, they decay by emission γ until they reach stability (Figure 1) [14] [15]. Exposure to high levels of γ -rays cause harmful effects (for example cancer), which is why a barrier is used to attenuate them (mainly by photoelectric effect and Compton effect) [16].

Shielding depends on the design of the HDR-B treatment room. Therefore, the IAEA suggests a room design with a doorless maze for ^{60}Co radioactive source, includes a control area, preparation/procedure room,

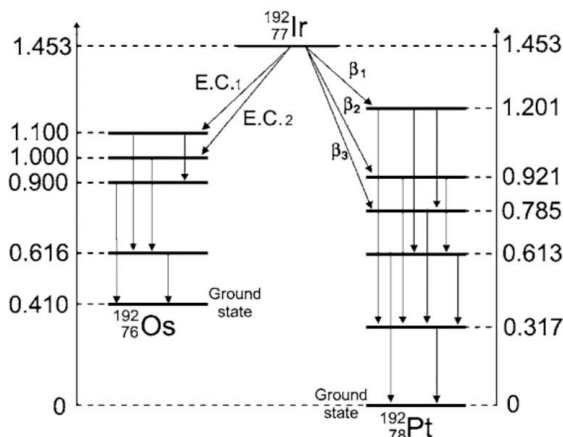


FIGURE 1. ^{192}Ir decay diagram by particle emission and EC [15].

recovery area, sluice room, and image processing area (Figure 2) [17]. The dimensions for the width of the maze should be 1.8 meters (m), the internal ones 4 m long by 4 m wide (Figure 2), and a height of 3 to 3.6 m. The above, assuming the use of fluoroscopy equipment for applicator placement [11], although Computed Tomography (CT) and Magnetic Resonance Imaging (MRI) simulation is also used [17].

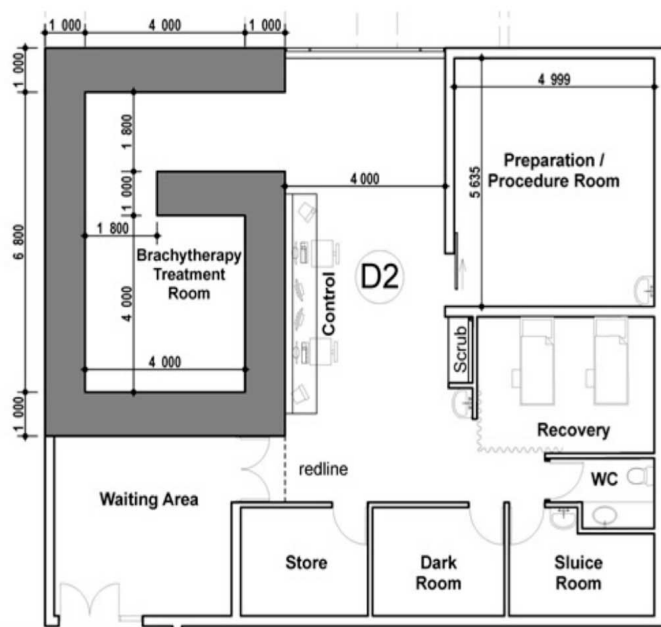


FIGURE 2. Brachytherapy treatment room for ^{60}Co source suggested by IAEA: dimensions and adjoining areas [17].

Calculation of primary barriers

IAEA Safety Report Series No. 47 (SRS-47) describes a method for calculating shielding thicknesses in walls, floor, and roof and considerations as primary barriers (shielding where useful radiation beam hits directly). This method starts from the calculation of the attenuation required by the barrier (B) given a dosimetry shielding point that is at a certain distance from the source (d) [4] [11] [18]. Thus, B is determined from Equation (1):

$$B = \frac{P d^2}{W U T} \quad (1)$$

Where P is the design limit measured in $\mu\text{Sv week}^{-1}$, W is the workload in micro grays per square meter week $^{-1}$ ($\mu\text{Gy m}^2 \text{ week}^{-1}$), U is the use factor, and T is the occupancy factor of adjacent areas [11].

Concerning P , it must ensure compliance with the permissible exposure dose limits for adjacent areas. The classification of the adjacent areas is:

- Controlled: areas with specific protective measures to control potential exposures under normal working conditions. The limit is P equal to 120 microsievert per week ($\mu\text{Sv week}^{-1}$) [11] [16].
- Uncontrolled (public): areas that are not designated as controlled but are under review. The design limit is 6 $\mu\text{Sv week}^{-1}$ [11] [16].

About W , it refers to the dose administered per treatment each time (usually in one week) [4] [11]. It is calculated by the Equation (2) [11]:

$$W = RAKR \cdot A \cdot t \cdot n \quad (2)$$

Where RAKR is the Reference Air Kerma Rate for a source of unit activity at one-meter distance modified by attenuation and scattering in the air [16]; A is the

total source activity measured in *becquerels* (Bq); t is the average treatment duration in hours, and n is the number of treatments per week [11].

According to the American Association of Medical Physicists Publication No. 21 (AAPM-21), W is determined by the Equation (3) [19]:

$$W = S_k \cdot t \cdot n \quad (3)$$

Where S_k is the air kerma strength of the source in units of U_0 ($\mu\text{Gy m}^2/\text{h}$) and it is equivalent to the product of RAKR times A [19].

For the T factor, it indicates the average fraction of time that a person is mostly exposed to adjacent area where the source is in use. Table 3 shows the value for each area according to NCRP Report No. 49 (NCRP-49) [4] [10] [11].

TABLE 3. Occupancy factor T recommended by the NCRP-49 [10] [11].

Type of area	T
Offices, laboratories, shops, children's play areas, nurse's stations, staff rooms. Control room, patient rooms.	1
Corridors.	1/4
Waiting rooms, toilets, stairways, unattended elevators, vehicular traffic.	1/16

It is important to mention that for HDR-B, the sources are isotropic, i.e., they are not collimated, and their emissions are in all directions. In this sense, the U factor will always be equal to 1 [4] [11].

It is also recommended the use of the *Tenth Value Layer* (TVL) and *Half Value Layer* (HVL), which reduce the radiation intensity by a factor of one tenth and one half of the initial intensity, respectively, whose thickness is specific for each material and radionuclide [11]. The number of TVL that produces a transmission factor B is calculated from the Equation (4) [11]:

$$TVL = \log_{10} \left(\frac{1}{B} \right) \quad (4)$$

So, the barrier thickness (E_t) is obtained by multiplying the TVL times the TVL value of the material (TVL_m)^[11], as shown in the Equation (5):

$$E_t = TVL \cdot TVL_m \quad (5)$$

Calculation of secondary barriers

In addition, secondary radiation must be considered, especially that transmitted into the maze. For which, the factor B for the secondary barriers (barriers not in direct contact with the radiation beam from the source), is calculated from Equation (6) [11]:

$$B = \frac{P d_{sca}^2 d_{sec}^2}{\alpha \text{WT} \left(\frac{F}{400} \right)} \quad (6)$$

Where d_{sca} is the distance from the radiation source to the patient in meters (m); d_{sec} is the distance from the patient to the point of interest in m ; α is the beam energy scattering fraction and scattering angle in d_{sca} ; F is the incident field area over the patient in square centimeters (cm^2).

MATERIALS AND METHODS

The method consists of three stages: the first is to identify the room design data, source characteristics, design limits and shielding material. The second stage is to determine the number of dosimetric point per wall and roof, calculating the shielding using the IAEA SRS-47 method (described previously) for each point, and obtain the area and volume of each barrier. The last stage involves calculating and analyzing the shielding reduction percentages (Figure 3).

First, the data of the HDR-B room are identified, considering the design, dimensions, and adjacent areas shown in Figure 4, having as primary barriers wall A, B, D, and E, and a distinction of primary and secondary barriers, on wall C and the roof.

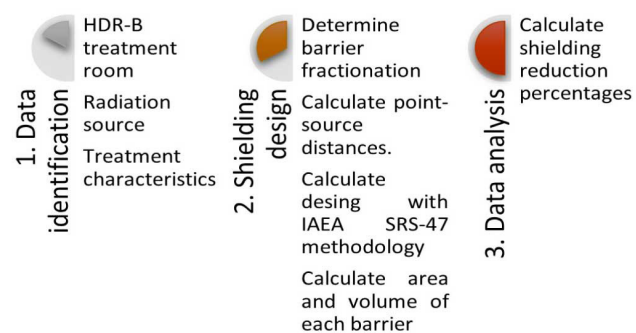


FIGURE 3. Method for fractional calculation of the shielding of an HDR-B room.

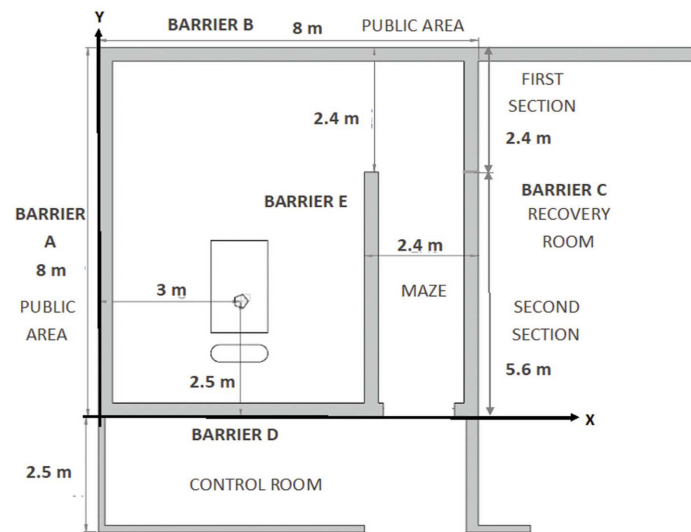


FIGURE 4. Representation of the dimensions and adjoining areas of the HDR-B room, in x-y view.

For this case, we consider the use of an ^{192}Ir source with a nominal activity of 370 Gigabecquerel (GBq), RAKR of $0.111 \mu\text{Gy} \cdot \text{MBq}^{-1} \cdot \text{m}^2 \cdot \text{h}^{-1}$ ^[11], total activity (A) of 555 GBq^[20], a workload (*n*) of 30 treatments per week, with an average treatment duration (*t*) of 10 minutes (0.167 hours) to deliver an absorbed dose of 7.5 Gy, to the prescription point per treatment and concrete as shielding material, whose TVL value for this source is $0.152 \text{ m}^{[11]}$.

Also, the value for the factor T and the design limit P is established according to the adjacent area and NCRP 49 (values shown in Table 3) [10]. The assignment of these values is shown in Table 4.

TABLE 4. Summary of values used according to the NCRP.

Barrier	Adjacent area	T	Type of area	P [$\mu\text{Sv week}^{-1}$]
A	Garden	1/16	Uncontrolled	6
B	Garden	1/16	Uncontrolled	6
C	Recovery room	1/16	Uncontrolled	6
D	Control room	1	Controlled	120
E	Maze	1/16	Uncontrolled	6
Roof	None	1/16	Uncontrolled	6

For the second stage, the barriers A, B, D and E are divided into 4 (5 points) and 10 (11 points) equal parts (see example in Figure 5, for 5 points), where for each division point (dosimetric points) and distances closer to the source (d_A , d_B , d_D and d_E) the following calculations are performed:

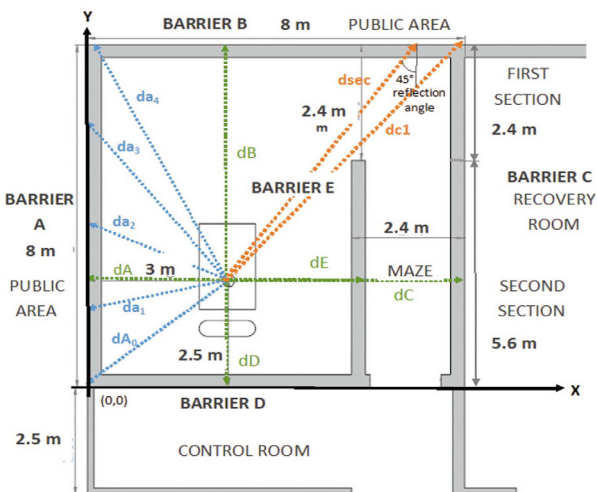


FIGURE 5. Location of 5 dosimetric points on barrier A, as well as the closest distances from the source to the walls of the HDR-B treatment room.

First, the distances of the points to the source (distance between two points) are calculated, using the Equation (7) [21].

$$d_n = \sqrt{(x - x_0)^2 + (y - y_0)^2 + (z - z_0)^2} \quad (7)$$

For this purpose, the positions (x, y, z) of the dosimetric points on the cartesian plane, represented by the HDR-B room, are considered. Which has origin (0, 0) at the lower left and the source position at ($x_0 = 3$, $y_0 = 2.5$, $z_0 = 1.1$) (Figure 4).

Then, the W factor is calculated by substituting the values of RAKR, A , t , and n , in the Equation (2), which results:

$$W = (0.111 \mu\text{Gy m}^2 \cdot \text{MBq}^{-1} \text{h}^{-1}) \\ (555 \times 10^3 \text{ MBq})(0.167 \text{ h})(30 \text{ treatments week}^{-1}) \\ W = 308,641.050 \mu\text{Gy m}^2 \text{ week}^{-1}$$

The shielding thickness is then calculated for each of the points of each barrier, substituting the values of P , W , U , T , and d the in Equation (1), obtaining:

$$B = \frac{(6 \mu\text{Sv week}^{-1})(d^2)}{(308,641.050 \mu\text{Gy m}^2 \cdot \text{week}^{-1})(1)(T)}$$

The obtained value of B is then substituted into the Equation (4) to calculate the number of TVL:

$$TVL = \log_{10} \left(\frac{1}{B} \right)$$

The result and the TVL value of the concrete for ^{192}Ir are substituted in the Equation (5), resulting:

$$Et = (TVL)(0.152 \text{ m})$$

Once all the points of barriers A, B, D, and E have been obtained, the area of each barrier is calculated by obtaining the areas of the rectangular trapezoids (a_{tr}) formed by the thicknesses of each dosimetric, as shown in Figure 6. This calculation is performed with the Equation (8) [22]:

$$a_{tr} = \frac{(B_t + b) * h}{2}$$

Where B_t is the major base (lower thickness), and b is the minor base (upper thickness), and h is the height (dosimetric point spacing).

The sum of the areas of the rectangular trapezoids provides the area of each barrier. Subsequently, it is multiplied by the height of the room, which is 3.5 meters, to obtain the volume.

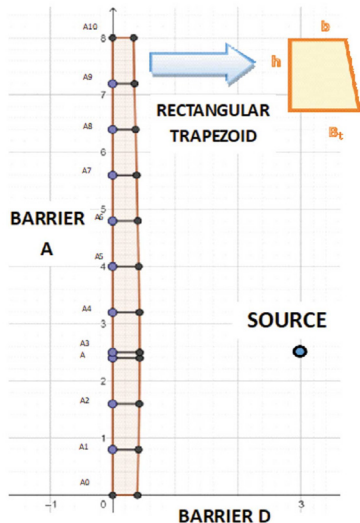


FIGURE 6. Rectangular trapezoid formed by the point A9 and A10 of the 11-point fractionation of the barrier A.

In the case of the wall C, it is divided into two sections (Figure 4). For the first section, the distance d_{c1} is considered and the shielding thickness is calculated using the calculations described for barriers A, B, D, and E. For the second section, the distance from the source to the middle of the maze on wall B having coordinates (6.8, 8) (Figure 4) is calculated using the Equation (7), resulting:

$$d_{sec} = \sqrt{(6.8 - 3)^2 + (8 - 2.5)^2} = 6.685 \text{ m}$$

For this case, we considered the d_{sca} value of 1.5 m and a maximum F of 400 cm² and a reflection angle of 45° for 60Co (α) of 0.0037 [11]; these values and the values of T, P, and W (calculated previously) are substituted in Equation (6) to obtain the factor B, resulting:

$$B = \frac{\left(\frac{6 \text{ } \mu\text{SV}}{\text{sem}}\right)(1.5 \text{ m})^2 (6.685 \text{ m})^2}{(0.0037) (308,641.050 \mu\text{Gy m}^2 \text{ week}^{-1})(1)\left(\frac{400}{400}\right)}$$

Then, the value of B is substituted in the Equation (4) and subsequently, Equation (5) are used to obtain the final thickness. The area is calculated by multiplying the width of the barrier (2.4 m for the first section and 5.6 m times the second section) and the sum of these are multiplied times the height (3.5 m) to obtain the volume.

For the roof shield calculation, it is divided into two sections (Figure 7).

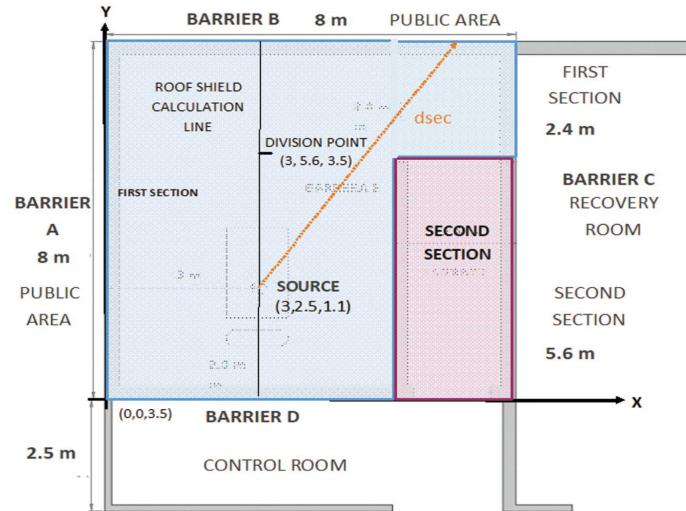


FIGURE 7. Dosimetric points calculated on the roof of the HDR-B room.

In the case of the first section, the fractionation into 5 and 11 divisions is performed on the position of the source on the x-axis (indicated with a black line in Figure 7). The calculations of the distances are carried out in the dimensions (x, y, z) with the Equation (7), the shortest distance to the source (3, 2.5, 3.5), and the position (3, 5.6, 3.5) are also considered.

Then, for each of the distances obtained, the thickness is calculated using the Equations (1), (4), and (5).

To obtain the area, Equation (8) is used in the same way with barriers A, B, D, and E. These areas are multiplied by the width of each section and the result is multiplied by the length of the room (5.6 m or 8 m) to obtain the volume.

The second section is analyzed as a secondary barrier, so the distance from the point d (6.8, 8, 3.5) (Figure 7) is calculated using the Equation (7). Subsequently, B is calculated with the Equation (6), considering the same values of d , F , and α . The shielding thickness is calculated using the Equations (4) and (5).

The area is obtained by multiplying the thickness times the length of the section (5.6 m). The result is multiplied by the width of the section (2.4 m) to obtain the volume.

As for the reference volume values, they are calculated by multiplying the thickness of the points dA, dB, dD, dC, dE and dT, times the length of each barrier (area), the result is multiplied by the height.

For the third stage, the percentage of reduction is calculated by comparing the volume calculated at one point in each of the barriers against this obtained for 5 and 11 points.

Also, the geometric mean (G) is calculated at the reduction percentages per barrier, which is defined as the root- n th (N) of the product of all the elements (n), represented by the Equation (9) [23] [24]:

$$G = \sqrt[n]{x_1 * x_2 * \dots * x_n} \quad (9)$$

As for the total percentage of the reduced shielding of the HDR-B room, it is calculated by adding the volumes of all barriers at one, 5, and 11 points. Subsequently, a comparison is made of the required shielding volume at one point vs. 5 points and one point vs. 11 points.

RESULTS AND DISCUSSION

From the previous study, Tables 5 and 6 were obtained as a result of the fractionation of barriers A, B, D, and E for 5 and 11 points, where x and y indicate the positions of each dosimetric point, d is the calculated distance from the point to the source measured in meters, Et is the required shielding thickness in meters, a is the area obtained from each rectangular trapezoid, ac is the sum of the areas of the rectangular trapezoids comprising the barrier.

TABLE 5. Shielding for barriers A, B, D and E, for 5 points.

Barrier	Nº	x	y	d [m]	Et [m]	a_{tr} [m ²]	a_c [m ²]	Volume [m ³]
A	0	0.000	0.000	3.905	0.350			
	1	0.000	2.000	3.041	0.383	0.733		
	dA	0.000	2.500	3.000	0.383	0.192		
	2	0.000	4.000	3.354	0.383	0.575		
	3	0.000	6.000	4.610	0.328	0.711		
	4	0.000	8.000	6.265	0.292	0.620		
B	0	0.000	8.000	6.265	0.292			
	1	2.000	8.000	5.590	0.304	0.596		
	dB	3.000	8.000	5.500	0.311	0.308		
	2	4.000	8.000	5.590	0.304	0.308		
	3	6.000	8.000	6.265	0.292	0.596		
	4	8.000	8.000	7.433	0.269	0.561		
D	0	0.000	0.000	3.905	0.338			
	1	1.400	0.000	2.968	0.383	0.505		
	2	2.800	0.000	2.508	0.410	0.555		
	dD	3.000	0.000	2.500	0.410	0.082		
	3	4.200	0.000	2.773	0.383	0.476		
	4	5.600	0.000	3.607	0.350	0.513		
E	0	5.600	0.000	3.607	0.364			
	1	5.600	1.400	2.823	0.410	0.542		
	dE	5.600	2.500	2.600	0.410	0.451		
	2	5.600	2.800	2.617	0.410	0.123		
	3	5.600	4.200	3.106	0.383	0.555		
	4	5.600	5.600	4.046	0.350	0.513		

According to Figure 8, we can observe that in barrier A, there is a decreasing trend in the thickness of the shielding thickness from 10.724 m³ of concrete calculated for one point to 9.909 m³ for 5 points and 9.916 m³ for 11 points. This behavior represents a percentage decrease of **7.600%** and **7.535%** (Table 7), respectively.

Also, in barrier B there is a decrease from 8.708 m³ at one point to 8.292 m³ at 5 points and 8.295 m³ at 11 points (Figure 8). The percentage decrease is **4.777%** and **4.743%**, respectively (Table 7).

TABLE 6. Shielding for barriers A, B, D and E, for 11 points.

Barrier	Nº	x	y	d [m]	Et [m]	a _{tr} [m ²]	a _c [m ²]	Volume [m ³]
A	0	0.000	0.000	3.905	0.350		2.833	9.916
	1	0.000	0.800	3.448	0.364	0.286		
	2	0.000	1.600	3.132	0.383	0.299		
	3	0.000	2.400	3.002	0.383	0.306		
	dA	0.000	2.500	3.000	0.383	0.038		
	4	0.000	3.200	3.081	0.383	0.268		
	5	0.000	4.000	3.354	0.383	0.306		
	6	0.000	4.800	3.780	0.364	0.299		
	7	0.000	5.600	4.314	0.338	0.281		
	8	0.000	6.400	4.920	0.319	0.263		
	9	0.000	7.200	5.576	0.304	0.249		
	10	0.000	8.000	6.265	0.292	0.238		
B	0	0.000	8.000	6.265	0.292		2.370	8.295
	1	0.800	8.000	5.924	0.298	0.236		
	2	1.600	8.000	5.675	0.304	0.241		
	3	2.400	8.000	5.533	0.304	0.243		
	dB	3.000	8.000	5.500	0.311	0.185		
	4	3.200	8.000	5.504	0.311	0.062		
	5	4.000	8.000	5.590	0.304	0.246		
	6	4.800	8.000	5.787	0.304	0.243		
	7	5.600	8.000	6.084	0.292	0.238		
	8	6.400	8.000	6.466	0.287	0.232		
	9	7.200	8.000	6.920	0.277	0.226		
	10	8.000	8.000	7.433	0.269	0.218		
D	0	0.000	0.000	3.905	0.338		2.113	7.396
	1	0.600	0.000	3.493	0.350	0.193		
	2	1.100	0.000	3.128	0.364	0.200		
	3	1.700	0.000	2.827	0.383	0.209		
	4	2.200	0.000	2.613	0.383	0.214		
	5	2.800	0.000	2.508	0.410	0.222		
	dD	3.000	0.000	2.500	0.410	0.082		
	6	3.400	0.000	2.526	0.410	0.148		
	7	3.900	0.000	2.664	0.383	0.222		
	8	4.500	0.000	2.905	0.383	0.214		
	9	5.000	0.000	3.227	0.364	0.209		
	10	5.600	0.000	3.607	0.350	0.200		
E	0	5.600	0.000	3.607	0.364		2.180	7.630
	1	5.600	0.600	3.244	0.383	0.209		
	2	5.600	1.100	2.944	0.383	0.214		
	3	5.600	1.700	2.726	0.410	0.222		
	4	5.600	2.200	2.613	0.410	0.230		
	dE	5.600	2.500	2.600	0.410	0.107		
	5	5.600	2.800	2.617	0.410	0.123		
	6	5.600	3.400	2.739	0.410	0.230		
	7	5.600	3.900	2.962	0.383	0.222		
	8	5.600	4.500	3.268	0.383	0.214		
	9	5.600	5.000	3.635	0.364	0.209		
	10	5.600	5.600	4.046	0.350	0.200		

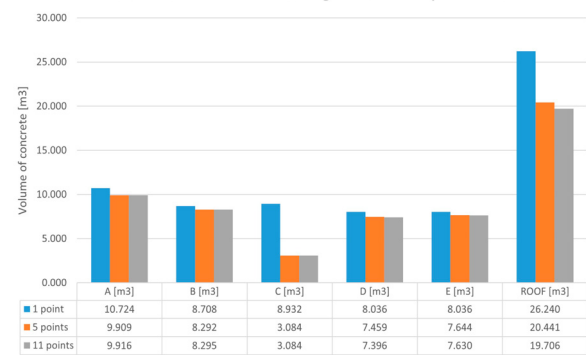
A similar case is barrier D, the volume decreased from 8.036 m³ for one point to 7.459 m³ for 5 points and 7.396 m³ for 11 points (Figure 8), representing a decrease of **7.180%** and **7.964%** (Table 7), respectively.

TABLE 7. Percentage of volume reduced by barrier.

Number of points	A [%]	B [%]	C [%]	D [%]	E [%]	Roof [%]
5	7.600	4.777	65.472	7.180	4.878	22.100
11	7.535	4.743	65.472	7.964	5.052	24.901

For barrier E, the volume calculated for one point is 8.036 m³, while for 5 points it is 7.644 m³ and for 11 points it is 7.630 m³ (Figure 8), representing a percentage decrease of **4.878%** and **5.052%** (Table 7) respectively.

Volume of concrete shielding calculated per barrier

**FIGURE 8 Comparison of the volume required per barrier.**

In the case of barrier C, it represents the best reduction in shielding, since a single point requires 8.932 m³ of concrete, while with the proposed method the volume required is 3.084 m³ (Table 8). This difference represents a **65.472%** of reduction in the shielding volume (Table 7).

TABLE 8. Shielding for barrier C.

Number of points	Section	x	y	d [m]	Et [m]	a [m ²]	ac [m ²]	Volume [m ³]
1	dc	8.00	2.50	5.000	0.319	-	-	8.932
First section	1	8.00	8.00	7.433	0.269	0.646	0.881	3.084
Second section	2	6.80	8.00	6.685	0.042	0.235		

For roof shielding, the volume required for one point is 26.240 m³ (Figure 8), meanwhile for 5 and 11 points, they were 20.441 m³ and 19.706 m³ respectively (Table 9), representing a reduction percentage of **22.100%** and **24.901%** respectively.

TABLE 9. Armoring for the roof.

Number of points	Nº	x	y	z	d [m]	Et [m]	atr [m ²]	V[tr] [m ³]	Volume [m ³]
5	0	3.000	0.000	3.500	3.466	0.364			20.441
	1	3.000	2.000	3.500	2.452	0.410	0.774	4.334	
	2	3.000	2.400	3.500	2.402	0.410	0.164	0.918	
	dt	3.000	2.500	3.500	2.400	0.410	0.041	0.230	
	2	3.000	4.000	3.500	2.830	0.410	0.615	3.444	
	3	3.000	5.600	3.500	3.920	0.350	0.608	4.864	
	4	3.000	6.000	3.500	4.244	0.338	0.138	1.104	
	5	3.000	8.000	3.500	6.001	0.298	0.636	5.088	
	dl	6.800	8.000	3.500	7.103	0.034	0.082	0.459	
	0	3.000	0.000	3.500	3.466	0.364			
	1	3.000	0.800	3.500	2.941	0.383	0.299	1.674	
11	2	3.000	1.600	3.500	2.563	0.410	0.317	1.775	
	3	3.000	2.400	3.500	2.402	0.410	0.328	1.837	
	Dt	3.000	2.500	3.500	2.400	0.410	0.041	0.230	
	4	3.000	3.200	3.500	2.500	0.410	0.287	1.607	
	5	3.000	4.000	3.500	2.830	0.410	0.328	1.837	
	6	3.000	4.800	3.500	3.324	0.383	0.317	1.775	
	7	3.000	5.600	3.500	3.920	0.350	0.293	2.344	
	8	3.000	6.400	3.500	4.579	0.328	0.271	2.168	
	9	3.000	7.200	3.500	5.277	0.311	0.256	2.048	
	10	3.000	8.000	3.500	6.001	0.298	0.244	1.952	
	dl	6.800	8.000	3.500	7.103	0.034	0.082	0.459	

The calculation of the geometric mean of the reduction percentages per wall at 5 points yielded a reduction percentage of **11.070%**, while for 11 points it was **11.526%**.

In addition, the shielding volume required for the HDR-B room at one point is 70.676 m³, while for fractionation at 5 points requires 56.829 m³ and at 11 points 56.027 m³, representing a percentage decrease of **19.592%** and **20.727%**, respectively (Table 10).

TABLE 10. Percentage of total volume reduced by 5 and 11 points.

Number of points	Total volume [m ³]	Reduced volume [%]
1	70.676	-
5	56.829	19.592
11	56.027	20.727

It is important to mention that, currently the design methods for shielding a HDR-B room are determined in accordance with the reports of the NCRP (No. 49,

151, and 155) and IAEA SRS-47, which establish the calculation of shielding thickness starting from the closest points to the source [4] [10] [11] [25]. However, knowing that gamma-ray attenuation is related to the interaction with matter, represented by the Equation (10):

$$I(x) = I(0) \cdot e^{-\mu x} \quad (10)$$

Where $I(x)$ is the intensity of gamma-rays as a function of distance x in the material and μ is the linear attenuation coefficient which depends on the energy of the gamma rays and the material which they interact with [26] [27], it is possible to compare an analysis based on fractionation of the barriers (proposed in Figure 3), derived from the fact that it is known that increasing the distance between the focal point (source) and the interaction point (dosimetric point) the amount of radiation is decreased by the inverse square law of the distance [7] [18] [26] [28] [29].

In this sense, a reduction in the volume of shielding was obtained in all barriers calculated with the proposed method (Figure 8), the most significant reduction percentage is 65.472% in the C barrier (Table 7). In the other barriers, the reduction was lower because the distances from the points to the source do not present much difference between them. One example is barrier B, divided into 11 points (Table 6), most of the calculated distances (column d[m]) are within the range from 5.500 to 7.433 m.

It is important to point out, according to Table 10, the volume calculated at 5 points (56.829 m³) is higher than at 11 points (56.027 m³); it can be inferred that the smaller the separation distance between the points, the higher the accuracy of the shielding calculation, since more intermediate points are considered. The most significant example is the roof, whose difference between the shielding volume calculated at 5 (is 20.441 m³) and 11 points (19.706 m³) is 0.735 m³ (Table 9).

Also, IAEA document SRS-47 recommends that for HDR-B room the shielding barriers should be primary because when the source is in use, it is isotropic and without collimation [11] [17] [31] [33]. However, it was analyzed that both in the second section of the C barrier (Figure 5) and in the second section of the roof (Figure 7) there is no primary radiation, but the radiation transmitted through by the E barrier and the scattered radiation, product of the reflection on barrier B. Therefore, and considering the cost-benefit, it is possible to consider these sections as secondary barriers, otherwise; it implies calculating an excessively and unnecessary thickness, which implies the requirement of more material, space, and economic resources [30] [34] [35].

It should be noted that there is no specific recommendation or method for the analysis of secondary radiation. Even estimating the absorbed dose at the entrance of the maze is difficult, so in practice, various methods have been adopted, ranging from considering only direct radiation or scattered radiation [4] [11].

In the case of the secondary radiation analysis, the value used for α corresponds to ^{60}Co , because in the IAEA SRS-47 report, it is not available for ^{192}Ir . In addition, ^{60}Co has a gamma-ray energy value (of 1.25 MeV) higher than that of ^{192}Ir (0.375 MeV), thus ensuring that the calculation is effective [11] [26] [36].

It is important to mention that this study does not contemplate the affectation of rear shielding derived from the elimination of part of it to install ducts and boxes embedded in walls, roofs and floors, hardware in lead-lined doors or concrete block joints, since these adaptations are specific to each HDR-B room [30] [37].

Similarly, it does not include the shielding analysis for the floor, because it is assumed that the HDR-B room is on the ground level does not affect any piping or drainage [32]. However, if necessary, it can be performed in the same way as for the roof.

Although the design of the HDR-B room is related to space and available resources, this method is intended as a strategy to reduce construction costs without failing to comply with national and international regulations regarding exposure dose limits for exposed personnel and the public, and also, to optimize resources to be allocated to other expenses such as the cost of equipment, radioactive sources, auxiliary equipment, service and maintenance costs, training and salaries of personnel [26] [31] [34] [37] [38].

In this sense, a cost-benefit analysis of the fractional shielding calculation could be expected to be effective in RP and cheaper in shielding material cost with respect to the IAEA SRS-47 methodology. However, the option of having an RP surveillance program is not ruled out [32] [34] [39].

As for the geometric mean calculated for the percentages reduced in each barrier (Table 7), it was obtained that, for the fractionation in 5 points, it was 11.070%, meanwhile for 11 points it was 11.526%. This indicates that the shielding reduction in the DHR-B room barriers is reduced by at least 11%.

Thus, the proposed method for the calculation of shielding for HDR-B rooms, which starts from the RP and optimizes space and economic resources allocated, a concrete reduction of 19.592% and 20.727% was obtained for the fractionation in 5 and 11 points respectively (Table 10), which makes it more beneficial compared to conventionally method using the IAEA 47.

CONCLUSIONS

According to the results obtained and basing this model on the IAEA SRS-47 methodology, it is concluded that through the fractional calculation of shielding and the distinction of primary and secondary barriers, it is possible to reduce 19.592% and 20.727% of construction material for the fractionation

in 5 and 11 points respectively, in a brachytherapy room with maze; optimizing costs without affecting the PR guidelines for exposed workers and public in adjacent areas.

This difference of percentage is related to the fractionation of the barriers, where the higher the fractionation, the higher the accuracy of the shielding calculation. This possible error is mitigated by including an HVL layer; however, an RP monitoring program is not rejected.

Finally, this study opens the way to be used in the design of shielding with other methodologies and in other areas with the use of ionizing radiation sources.

AUTHOR CONTRIBUTIONS

S.G.G. conceptualized the project, developed the methodology and writing of the manuscript. H.M.M.M. carried out formal analysis and writing of the final version of the manuscript. J.P.H. conceptualization of the project and designed and supervised development of the methodology writing of the manuscript. M.A.M.F. provided materials for the development of the research, supervised the development of the methodology, reviewed, and validated the final version of the manuscript. F.M.S. validated the methodology design and supervised the development of the methodology and provided materials and resources for the project. All authors reviewed and approved the final version of the manuscript.

REFERENCES

- [1] International Commission on Radiological Protection. Las Recomendaciones 2007 de la Comisión Internacional de Protección Radiológica [Internet]. Madrid: Sociedad Española de Protección Radiológica; 2007. 116p. Reporte No. 103. Available from: https://www.icrp.org/docs/P103_Spanish.pdf
- [2] International Atomic Energy Agency. Annual Report for 2004 [Internet]. Vienna: International Atomic Energy Agency; 2004. 89p. Report No. 2004. Available from: https://www.iaea.org/sites/default/files/anrep2004_full.pdf
- [3] International Atomic Energy Agency. Radiation Safety in Industrial Radiography. Specific Safety Guide No. SSG-11 [Internet]. Vienna: International Atomic Energy Agency; 2011. 104p. Report No. SSG-11 Available from: https://www-pub.iaea.org/MTCD/Publications/PDF/Pub1466_web.pdf
- [4] Perez-Calatayud J, Corredoira Silva E, Crispín Contreras V, Eudaldo Puell T, et al. Protección radiológica en Braquiterapia: Informe del grupo de trabajo de Braquiterapia de la SEFM. Rev Física Médica [Internet]. 2015;16(2):11-47. Available from: <https://revistadefisicamedica.es/index.php/rfm/article/view/175>
- [5] International Commission on Radiological Protection. Protección Radiológica en Medicina [Internet]. Ciudad Autónoma de Buenos Aires: Sociedad Argentina de Radioprotección; 2011. 64p. Publicación No. 105. Available from: <https://www.icrp.org/docs/P%20105%20Spanish.pdf>
- [6] International Atomic Energy Agency. Radiation Protection and Safety in Medical Uses of Ionizing Radiation [Internet]. Vienna: International Atomic Energy Agency; 2018. 318p. Specific Safety Guide No. SGG-46. Available from: https://www-pub.iaea.org/MTCD/Publications/PDF/PUB1775_web.pdf
- [7] Núñez M. Protección radiológica en Medicina Nuclear [Internet]. 2008; Available from: https://www.alasbimn.net/comites/tecnologos/material/Proteccion_radiologica.pdf
- [8] Reglamento General de Seguridad Radiológica [Internet]. 1988. Available from: https://www.gob.mx/cms/uploads/attachment/file/122476/reglamento_general_seguridad_radiologica.pdf
- [9] Eckerman K, Harrison J, Menzel HG, Clement CH. Compendium of Dose Coefficients based on ICRP Publication 60 [Internet]. International Commission on Radiological Protection; 2013. 130p. ICRP publication 119. Available from: [https://www.icrp.org/docs/P%20119%20JAICRP%2041\(s\)%20Compendium%20of%20Dose%20Coefficients%20based%20on%20ICRP%20Publication%2060.pdf](https://www.icrp.org/docs/P%20119%20JAICRP%2041(s)%20Compendium%20of%20Dose%20Coefficients%20based%20on%20ICRP%20Publication%2060.pdf)
- [10] National Council on Radiation Protection and Measurements. Structural Shielding design and evaluation for medical use of x rays and gamma rays of energies up to 10 MeV. Washington: National Council on Radiation Protection and Measurements; 1998. 113p. Report No. 049.
- [11] International Atomic Energy Agency. Radiation Protection in the design of Radiotherapy Facilities [Internet]. Vienna: International Atomic Energy Agency; 2006. 130p. Safety Reports Series No. 47. Available from: https://www-pub.iaea.org/MTCD/Publications/PDF/Pub1223_web.pdf
- [12] Turner JH. An introduction to the clinical practice of theranostics in oncology. Br J Radiol [Internet]. 2018;91(1091):20180440. Available from: <https://dx.doi.org/10.1259%2Fbjr.20180440>
- [13] Montemaggi P, Trombetta M, Brady LW. Brachytherapy, an International Perspective [Internet]. Springer; 2016. 408p. Available from: <https://doi.org/10.1007/978-3-319-26791-3>
- [14] Pallaroso Yela MA. Efecto del material de contraste en las distribuciones de dosis asociadas a la braquiterapia de Alta Tasa con Iridio-192 para tratamientos de cáncer cérvico-uterino [Internet]. [Master's thesis]. [Quito]: Escuela Politécnica Nacional, 2018. 73p. Available from: <https://bibdigital.epn.edu.ec/bitstream/15000/19490/1/CD-8888.pdf>
- [15] Medina Mendieta SM. Puesta en servicio clínico de la unidad de Braquiterapia de alta tasa de dosis con fuente de 60 Co SagiNova; en el Centro Nacional de Radioterapia "Nora Astorga" en el periodo de marzo -abril 2018 [Internet]. [dissertation]. [Managua]: Universidad Nacional Autónoma de Nicaragua, Managua, 2019. 93p. Available from: <https://repositorio.unan.edu.ni/12539/1/MONOGRAFIA%20SARAY%20MEDINA%20MENDIETA.pdf>
- [16] Yanchapanta Bastidas VN. Metodología para adaptar recintos de irradiación de braquiterapia HDR con Ir-192 a Co-60 [Internet]. [Master's thesis]. [Mendoza]: Universidad Nacional de Cuyo, 2016. 80p. Available from: <http://ricabib.cab.cnea.gov.ar/571/1/Yanchapanta.pdf>
- [17] International Atomic Energy Agency. Radiotherapy facilities: Master planning and concept design considerations. Vienna: International Atomic Energy Agency; 2014. 31p. Human Health Reports No. 10.
- [18] Saravia-Rivera GE. Protección y seguridad radiológicas. Anal Radiol Mex [Internet]. 2013;2:105-110. Available from: <https://www.medicgraphic.com/pdfs/anaradmx/arm-2013/arm132g.pdf>
- [19] American Association of Physicists in Medicine. Specification of brachytherapy source strength [Internet]. New York: American Association of Physicists in Medicine; 1987. 21p. Report No. 21. Available from: https://www.aapm.org/pubs/reports/rpt_21.pdf
- [20] Brachytherapy V. Equipo de carga diferida HDR GammaMedplus iX, 3/24 iX. [Internet]. Varian. Available from: <https://www.varian.com/es/products/brachytherapy/afterloaders-applicators/gammamedplus-ix>
- [21] Tinoco G. Antecedentes: Distancia entre dos puntos [Internet]. UAEM; 2013. Available from: http://metabase.uaem.mx:8080/bitstream/handle/123456789/2883/_1_Antecedentes-Distancia%20entre%20dos%20puntos.pdf?sequence=1
- [22] Flores Martínez P. El trapecio isóceles de diagonales perpendiculares [Internet]. Universidad de Granada. Available from: [http://www.ugr.es/~pflores/textos/aRTICULOS/Propuestas/trapecio.pdf#:~:text=Caracter%C3%ADsticas%20del%20trapecio%20de%20diagonales%20perpendiculares%20Seg%C3%A1n%20las,dos%20tri%C3%A1ngulos%20rect%C3%A1ngulos%20dos%20tri%C3%A1ngulos%20isos%C3%A1celes](http://www.ugr.es/~pflores/textos/aRTICULOS/Propuestas/trapecio.pdf#:~:text=Caracter%C3%ADsticas%20del%20trapecio%20de%20diagonales%20perpendiculares%20Seg%C3%A1n%20las,dos%20tri%C3%A1ngulos%20rect%C3%A1ngulos%20dos%20tri%C3%A1ngulos%20is%C3%B3celes%2C%20y%20dos%20tri%C3%A1ngulos%20isos%C3%A1celes)
- [23] Salazar, C, y Del Castillo S. Fundamentos Básicos De Estadística. 2018. 224p.
- [24] Vargas Sabadías A. Estadística descriptiva e inferencial. Murcia:Universidad de Castilla-La Mancha; 1995. 576p.
- [25] National Council on Radiation Protection and Measurements. Structural Shielding Design and Evaluation for Megavoltage X- and Gamma-Ray Radiotherapy Facilities. Bethesda: NCRP; 2005. Report No. 151.

- [26] Cherry R. Radiaciones ionizantes. In: Enciclopedia de salud y seguridad en el trabajo [Internet]. 2010. Available from: <https://www.insst.es/documents/94886/162520/Cap%C3%ADtulo+48.+Radiaciones+ionizantes>
- [27] Ghiasi H, Mesbahi A. A new analytical formula for neutron capture gamma dose calculations in double-bend mazes in radiation therapy. Reports Pract Oncol Radiother [Internet]. 2012;17:220-225. Available from: <https://doi.org/10.1016/j.rpor.2012.03.011>
- [28] Delgado Ramos O, Fernández Frededs O, Leyton Legués F, Rodríguez Casas AM, et al. Manual de protección radiológica y de buenas prácticas en radiología dento-maxilo-facial [Internet]. Chile: Instituto de Salud Pública de Chile; 82p. Available from: <https://www.minsal.cl/portal/url/item/7f2d789a9750153be04001011f012d29.pdf>
- [29] Preciado Ramírez M, Luna Cano V. Medidas Básicas de Protección Radiológica. Cancerología. Cancerología [Internet]. 2010;5(2010):25-30. Available from: <http://inca-mexico.org/revistainvestiga/elementos/documentosPortada/1294860259.pdf>
- [30] Horton P, Eaton D. Design and Shielding of Radiotherapy Treatment Facilities [Internet]. Philadelphia: IOP Publishing; 2013. 304p. Available from: <https://doi.org/10.1088/978-0-7503-1440-4>
- [31] International Atomic Energy Agency. Setting Up a Radiotherapy Programme: Clinical, Medical Physics, Radiation Protection and Safety Aspects [Internet]. Vienna: International Atomic Energy Agency; 2008. 255p. Available from: https://www-pub.iaea.org/MTCD/Publications/PDF/pub1296_web.pdf
- [32] Australian Radiation Protection and Nuclear Safety Agency. Radiation Protection in Radiotherapy [Internet]. Barton: Acting Chief Executive Officer of ARPANSA; 2008. 106p. Radiation Protection Series Publication No. 14.3. Available from: https://www.arpansa.gov.au/sites/default/files/legacy/pubs/rps/rps14_3.pdf
- [33] International Atomic Energy Agency. Radiation Oncology Physics: A Handbook for Teachers and Students [Internet]. Vienna: International Atomic Energy Agency; 2005. 657p. Available from: https://www-pub.iaea.org/mtcd/publications/pdf/pub1196_web.pdf
- [34] International Atomic Energy Agency. Implementation of High Dose Rate Brachytherapy in Limited Resource Settings [Internet]. Vienna: International Atomic Energy Agency; 2015. 97p. Human Health Series No. 30. Available from: <https://www-pub.iaea.org/MTCD/Publications/PDF/Pub1670web-5444797.pdf>
- [35] Jalbert M. Intensity Modulation of Medium-Energy, High Dose Rate Brachytherapy Sources Brachytherapy Sources [Internet]. [dissertation]. [Worcester]: Worcester Polytechnic Institute, 2020. 27p. Available from: <https://digital.wpi.edu/pdfviewer/8049g7500>
- [36] International Atomic Energy Agency. Protección radiológica y seguridad de las fuentes de radiación: Normas básicas internacionales de seguridad [Internet]. Vienna: International Atomic Energy Agency; 2011. 280p. N° GSR Part 3. Available from: https://www-pub.iaea.org/MTCD/Publications/PDF/SupplementaryMaterials/SupM_Pub1531_Spanish.pdf
- [37] Arwui CC, Schandorf C, Nani K, Darko EO, et al. Shielding design of a brachytherapy unit at the Korle Bu teaching hospital in Ghana: Comparison of theoretical calculations and experimental study. Radiat Prot Dosimetry [Internet]. 2010;140:59-66. Available from: <https://doi.org/10.1093/rpd/ncq001>
- [38] American Association of Physicists in Medicine. Remote Afterloading Technology [Internet]. New York: American Institute of Physics; 1993. 107p. Report No. 41. Available from: https://www.aapm.org/pubs/reports/rpt_41.pdf
- [39] Van Den Broek JG, Weatherburn H. Re-evaluation of a radiation protection cost benefit analysis study in brachytherapy. Br J Radiol [Internet]. 1994;67:59-62. Available from: <https://doi.org/10.1259/0007-1285-67-793-59>